The Effects of Realistic Nuclear Kinetics, Dimensionality, and Resolution on Detonations in Low-Density Type Ia Supernovae Environments

A Dissertation Presented for the

Doctor of Philosophy

Degree

The University of Tennessee, Knoxville

Thomas L. Papatheodore

August 2015

© by Thomas L. Papatheodore, 2015
All Rights Reserved.

To my wife, Leesa.

Acknowledgements

I would like to give special thanks to my advisor Dr. Bronson Messer for his guidance and encouragement during my time as a graduate researcher. I also thank Dr. Raph Hix, Dr. Mike Guidry, and Dr. Steven Wise for serving as members of my doctoral committee and also for their instructional support in various aspects of my research. I would also like to acknowledge Eric Lenz, Austin Harris, and Dean Townsley for providing advice and useful conversations that helped advance my understanding of this work. In addition, I express my appreciation to Suzanne Parete-Koon and Chris Smith for introducing me to the FLASH code and the general aspects of simulating detonations in Type Ia supernovae. I also thank Dr. Marianne Breinig for her guidance and instructional support during my time as a graduate student and teaching assistant. Finally, I would like to thank my family, and especially my wife Leesa Papatheodore, for their patience and encouragement over my many years as a student.

Abstract

Type Ia supernovae are most likely thermonuclear explosions of carbon/oxygen white dwarves in binary stellar systems. These events contribute to the chemical and dynamical evolution of their host galaxies and are essential to our understanding of the evolution of our universe through their use as cosmological distance indicators. Nearly all of the currently favored explosion scenarios for these supernovae involve detonations. However, modeling astrophysical detonations can be complicated by numerical effects related to grid resolution. In addition, the fidelity of the reaction network chosen to evolve the nuclear burning can alter the time and length scales over which the burning occurs. Multidimensional effects further complicate matters by introducing a complex cellular structure within the reaction zone. Here, we report on how these complications can affect the outcome of simulating such astrophysical detonations in the context of Type Ia supernovae.

Table of Contents

1 Introduction **1**

1.1 Observations . . . 4

1.2 Cosmological Distance Indicators . . . 7

1.3 Type Ia Explosion Mechanisms . . . 8

1.3.1 Single-Degenerate Scenario . . . 8

1.3.2 Double-Degenerate Scenario . . . 10

1.3.3 Double-Detonation Scenario . . . 12

1.4 SNe Ia Simulations . . . 13

1.5 Outline . . . 13

2 Detonation Theory & Previous Work **14**

3 Burning Within Numerical Shocks **21**

3.1 Introduction . . . 21

3.2 Simulations . . . 23

3.2.1 1D . . . 24

3.2.2 2D . . . 27

3.3 Summary and Discussion . . . 36

4 1D Simulations **41**

4.1 Case 1: $\rho_{fuel} = 1{\times}10^7$ g cm^{-3} . . . 44

4.2 Case 2: $\rho_{fuel} = 5{\times}10^7$ g cm^{-3} . . . 55

4.3 Conclusions . . . 80

5 Multi-D Simulations **83**

5.1 2D . . . 83

5.2 3D . . . 101

5.3 Conclusions . . . 104

6 Double-Detonations in Confined He-Belts **108**

6.1 Simulations . . . 109

6.2 Results . . . 118

6.2.1 He-Belts . . . 118

6.2.2 Ni-Belts . . . 130

6.3 Summary . . . 135

7 Conclusions **143**

Bibliography **146**

Appendix **155**

Appendix A . . . 156

Appendix B . . . 161

Vita **162**

List of Tables

Table 4.1 Isotopes tracked in the four nuclear reaction networks. 43

Table 4.2 Detonation velocities and overdrive parameters calculated for the four reaction networks at a fuel density of 1×10^7 g cm^{-3} (refinement level 14: 0.001953125 cm). 56

Table 4.3 Detonation velocities and overdrive parameters calculated for the four reaction networks at a fuel density of 5×10^7 g cm^{-3}. 76

Table 5.1 Detonation cell sizes measured for simulations evolved with each of the four reaction networks at different levels of grid refinement. 94

Table 5.2 Burning Lengths calculated for detonations evolved with the Aprox13 network. The C-burning lengths were calculated analogously to 1D. The O-burning lengths were calculated by two methods: Method 1 is measured from the back of the numerical shock to the left-most coordinate where the ^{16}O mass fraction still has a value greater than or equal to 0.25 or 0.05 (50% or 90% of initial value), and Method 2 is measured from the average position of the shock to the coordinate where the ^{16}O mass fraction (averaged over y for a given x-coordinate) has been depleted by 50% or 90%. 95

Table 5.3 Burning Lengths calculated for detonations evolved with the X14 network. The C-burning lengths were calculated analogously to 1D. The O-burning lengths were calculated by two methods: Method 1 is measured from the back of the numerical shock to the left-most coordinate where the ^{16}O mass fraction still has a value greater than or equal to 0.25 or 0.05 (50% or 90% of initial value), and Method 2 is measured from the average position of the shock to the coordinate where the ^{16}O mass fraction (averaged over y for a given x-coordinate) has been depleted by 50% or 90%. 96

Table 5.4 Burning Lengths calculated for detonations evolved with the X14+ap+an network. The C-burning lengths were calculated analogously to 1D. The O-burning lengths were calculated by two methods: Method 1 is measured from the back of the numerical shock to the left-most coordinate where the ^{16}O mass fraction still has a value greater than or equal to 0.25 or 0.05 (50% or 90% of initial value), and Method 2 is measured from the average position of the shock to the coordinate where the ^{16}O mass fraction (averaged over y for a given x-coordinate) has been depleted by 50% or 90%. 97

Table 5.5 Burning Lengths calculated for detonations evolved with the X150 network. The C-burning lengths were calculated analogously to 1D. The O-burning lengths were calculated by two methods: Method 1 is measured from the back of the numerical shock to the left-most coordinate where the ^{16}O mass fraction still has a value greater than or equal to 0.25 or 0.05 (50% or 90% of initial value), and Method 2 is measured from the average position of the shock to the coordinate where the ^{16}O mass fraction (averaged over y for a given x-coordinate) has been depleted by 50% or 90%. 98

Table 6.1 Results from He-belt simulations. Masses, densities, and kinetic energies are in units of $M_\odot$, 10^6 g cm^{-3}, and 10^{51} ergs, respectively. The FWHM defines a velocity range with units of km s^{-1}. The subscripts b and c stand for core and belt, respectively. 117

Table 6.2 Results from Ni-belt simulations. Masses, densities, and kinetic energies are in units of $M_\odot$, 10^6 g cm^{-3}, and 10^{51} ergs, respectively. The FWHM defines a velocity range with units of km s^{-1}. The subscripts b and c stand for core and belt, respectively. 120

List of Figures

Figure 1.1 Classification system for supernovae. Type Ia supernovae are defined by the presence of strong Si absorption features in their early and peak spectra, differentiating them from all other Type I supernovae. 3

Figure 1.2 (a) Collection of nearby SNe Ia light curves as observed and (b) after parameter fitting. Hamuy et al. (1993) 5

Figure 1.3 Cartoon depicting a dense, expanding SNe Ia remnant just after an explosion. The receding photosphere first shows the unburned C (blue) in the outer edge, followed by the IMEs (red), and subsequently IGEs (black) 6

Figure 2.1 P-V diagram showing three different regimes for a given detonation velocity. 17

Figure 2.2 P-V diagram showing the path taken by a fluid element as a reactive shock front passes. 19

Figure 3.1 Temperature as a function of position for a small section of the problem setup along with the adaptive mesh (shown only on the bottom of the figure). Red (1×10^{10} K) denotes the "match head" region used to ignite the fuel shown in blue (1×10^{7} K). 24

Figure 3.2 Results from the 1D simulations showing the secondary shock structure in the density profile due to unresolved C-burning (0.5-cm resolution) at t $\sim 10^{-6}$s. The solid curves show the outcome when shock burning is allowed and the dashed curves show the results when burning is prohibited in the shock. The different pairs of curves correspond to the different initial fuel densities of 1×10^9, 5×10^8, 1×10^8, and 5×10^7 g cm^{-3}. We can see that preventing burning in the shock eliminates the nonphysical shock structure in the two higher-density simulations, leading to the correct detonation velocity and physically acceptable results. 25

Figure 3.3 A zoomed in view of the density profiles from the 1×10^8 and 5×10^7 g cm^{-3} simulations. Although they do not show a secondary shock, there are differences in their peak values corresponding to premature burning conditions inside the shock as opposed to the proper post-shock conditions. 26

Figure 3.4 Maximum of nuclear energy release rate versus time for the $\rho_i = 5 \times 10^7$ g cm^{-3} simulation with 0.5-, 0.125-, and 0.03125-cm maximum resolution. At 0.5-cm resolution the energy release is under-resolved and at 0.03125-cm and above the rate has converged to its steady value. 28

Figure 3.5 Snapshots of pressure from unperturbed, 2D series. The top, middle, and bottom rows show the results from the 0.5-, 0.125-, and 0.03125-cm maximum resolution simulations, respectively. The 0.5- and 0.125-cm panels show the results at t $= 8 \times 10^{-7}$s and the 0.03125-cm panels show the results at t $= 4.15 \times 10^{-7}$s. The differences in the fine features of the detonation fronts are due to various onset times for cellular burning. 31

Figure 3.6 Snapshots of pressure from the perturbed, 2D series. The top, middle, and bottom rows show the results from the 0.5-, 0.125-, and 0.03125-cm maximum resolution simulations, respectively. The 0.5-, 0.125-, 0.03125-cm panels show the pressure at t = 1.5×10^{-6}s, t = 8×10^{-7}s, and t = 4.15×10^{-7}s, respectively. The differences in the fine features of the detonation fronts are due to various onset times for cellular burning. 32

Figure 3.7 Diagram illustrating the formation of cellular structure. The shock front is shown at three times, superimposed on the triple-point paths (Fickett and Davis, 1979; Timmes et al., 2000a). The main features of the detonation front are the Mach stems, incident shocks, and transverse waves. The points where these three features coexist are high-pressure regions called triple-shock structures, or triple-points, which trace out the cellular pattern shown in black. 33

Figure 3.8 Transverse velocity versus position for the perturbed, 0.5-cm resolution model. The left and right panels show the cases where burning is allowed and prohibited within the shock, respectively. The color map can be seen in the top left panel only, while each panel has its own scale. The top, middle, and bottom rows show the results for the two cases at 1.25×10^{-6} s, 2.25×10^{-6} s, and 3.25×10^{-6} s, respectively. . 37

Figure 3.9 Maximum density profiles from the unperturbed, 2D series showing the onset of cellular burning (steep increases in density). The strength of the triple-points corresponding to these maximum values are dependent on resolution as well as the treatment of burning within the numerical shock. 38

Figure 4.1 Schematic representation of the Aprox13 network showing the approximated (α,p)(p,γ)-links (see Frank Timmes' website – http://cococubed.asu.edu) 42

Figure 4.2 The 50% and 90% burning lengths were measured from the back of the numerical shock to a distance where the initial mass fraction of the fuel was reduced by 50% or 90%, respectively. 45
Figure 4.3 50% C-burning length versus level of grid refinement for four reaction networks in Table 4.1. Level 6, 8, 10, 12, and 14 correspond to 0.5, 0.125, 0.03125, 0.0078125, and 0.001953125 cm resolution. 50
Figure 4.4 90% C-burning length versus level of grid refinement for four reaction networks in Table 4.1. Level 6, 8, 10, 12, and 14 correspond to 0.5, 0.125, 0.03125, 0.0078125, and 0.001953125 cm resolution. 51
Figure 4.5 50% O-burning length versus level of grid refinement for four reaction networks in Table 4.1. Level 6, 8, 10, 12, and 14 correspond to 0.5, 0.125, 0.03125, 0.0078125, and 0.001953125 cm resolution. 52
Figure 4.6 90% O-burning length versus level of grid refinement for four reaction networks in Table 4.1. Level 6, 8, 10, 12, and 14 correspond to 0.5, 0.125, 0.03125, 0.0078125, and 0.001953125 cm resolution. 53
Figure 4.7 ^{12}C, ^{16}O, ^{28}Si mass fractions resulting from detonations with fuel density of 1×10^{7} g cm^{-3} (t=6×10^{-6} s). 54
Figure 4.8 Detonation velocity vs time for the four nuclear reaction networks at the highest grid resolution. 56
Figure 4.9 Total energy generation rate vs time for the four nuclear reaction networks at the highest grid resolution. 57
Figure 4.10 detonation velocity vs time for the Aprox13 network at different resolution. 58
Figure 4.11 Total energy generation rate vs time for the Aprox13 network at different resolution. 59
Figure 4.12 A pressure profile showing the oscillations behind the main shock front for a detonation evolved with the X150 network at 0.03125 cm resolution. 62
Figure 4.13 Thermodynamic and isotopic profiles along with the numerical shock. Here we see the C-pocket behind the shock before it explodes (t = 0.0 s). 63

Figure 4.14 Thermodynamic and isotopic profiles along with the numerical shock. Here we see the profiles just after ignition of the C-pocket (t = 1.0×10^{-9} s). 64
Figure 4.15 Thermodynamic and isotopic profiles along with the numerical shock. Here the C-pocket has finished burning and now the O-pocket has ignited (t = 2.0×10^{-9} s). 65
Figure 4.16 Thermodynamic and isotopic profiles along with the numerical shock. Here the C- and O-pockets are building back up (t = 3.0×10^{-9} s). . . 66
Figure 4.17 Thermodynamic and isotopic profiles along with the numerical shock. Here the C- and O-pockets continue to grow (t = 4.0×10^{-9} s). 67
Figure 4.18 Thermodynamic and isotopic profiles along with the numerical shock. Here the profiles have returned to their initial states as in Figure 4.13 (t = 5.0×10^{-9} s). 68
Figure 4.19 A larger view of the domain showing the oscillations embedded in the profiles. 69
Figure 4.20 50% C-burning length versus level of grid refinement for four reaction networks in Table 6.1. Level 6, 8, 10, 12, and 14 correspond to 0.5, 0.125, 0.03125, 0.0078125, and 0.001953125 cm resolution. 70
Figure 4.21 90% C-burning length versus level of grid refinement for four reaction networks in Table 6.1. Level 6, 8, 10, 12, and 14 correspond to 0.5, 0.125, 0.03125, 0.0078125, and 0.001953125 cm resolution. 71
Figure 4.22 50% O-burning length versus level of grid refinement for four reaction networks in Table 6.1. Level 6, 8, 10, 12, and 14 correspond to 0.5, 0.125, 0.03125, 0.0078125, and 0.001953125 cm resolution. 73
Figure 4.23 90% O-burning length versus level of grid refinement for four reaction networks in Table 6.1. Level 6, 8, 10, 12, and 14 correspond to 0.5, 0.125, 0.03125, 0.0078125, and 0.001953125 cm resolution. 74
Figure 4.24 ^{12}C, ^{16}O, ^{28}Si mass fractions resulting from detonations with fuel density of 5×10^{7} g cm^{-3} (t=6×10^{-6} s). 75

Figure 4.25 Detonation Velocity vs Time for the four nuclear reaction networks. . 77
Figure 4.26 Total energy generation rate vs time for the four nuclear reaction networks at the highest grid resolution. 78
Figure 4.27 Detonation Velocity vs Time for the Aprox13 network at different resolution. 79
Figure 4.28 Total energy generation rate vs time for the Aprox13 network at different resolution. 80

Figure 5.1 Cellular structure shown by a plot of the maximum pressure achieved at each grid zone during the simulation evolved with the Aprox13 network. Note the scales of the plots in Figures 5.1, 5.2, 5.3, 5.4 are different in order to show the cellular features from each network. 85
Figure 5.2 Cellular structure shown by a plot of the maximum pressure achieved at each grid zone during the simulation evolved with the X14 network. Note the scales of the plots in Figures 5.1, 5.2, 5.3, 5.4 are different in order to show the cellular features from each network. 86
Figure 5.3 Cellular structure shown by a plot of the maximum pressure achieved at each grid zone during the simulation evolved with the X14+ap+an network. Note the scales of the plots in Figures 5.1, 5.2, 5.3, 5.4 are different in order to show the cellular features from each network. . . . 87
Figure 5.4 Cellular structure shown by a plot of the maximum pressure achieved at each grid zone during the simulation evolved with the X150 network. Note the scales of the plots in Figures 5.1, 5.2, 5.3, 5.4 are different in order to show the cellular features from each network. 88
Figure 5.5 Log-plot of the ^{12}C mass fraction along with several 1D samples (see Figure 5.6) along the front. The numerical shock is shown in white. . . 91
Figure 5.6 ^{12}C profiles resulting from the 1D samples taken in Figure 5.5. These profiles show the differences in the ^{12}C mass fraction at different locations along the detonation front. 92

Figure 5.7 Detonation cells superimposed on ^{12}C mass fraction resulting from the detonation evolved with the X14 network at 8 levels of grid refinement. Behind the triple-points the ^{12}C is depleted on a shorter distance behind the shock (white curve) relative to its depletion behind the weak incident shocks between the triple-points. 93

Figure 5.8 ^{16}O mass fraction (only plotted for values of 0.25 and higher) resulting from the simulation evolved with the Aprox13 network at 10 levels of grid refinement. The black arrow represents a possible 1D sample taken in order to calculate the 50% O-burning length. If burning lengths are measured analogously to 1D, then such a sample that terminates at an unrepresentative pocket of over-reacted fluid could influence results . . 99

Figure 5.9 Same as Figure 5.8 but showing the two methods used to calculate O-burning lengths. In method 1 (black lines showing the minimum, maximum, and average values), we measured from the back of the numerical shock to the left-most coordinate where the ^{16}O mass fraction was still 0.25 or higher. In method 2, we measured from the average shock location to the coordinate where the y-average of ^{16}O is 0.25. . . 100

Figure 5.10 Plot of the detonation velocities versus time for the 2D results evolved with the X14 network at three levels of grid refinement. The 1D result at 10 levels of grid refinement is also shown for comparison. 102

Figure 5.11 Plot of the total nuclear energy generation integrated over the grid versus time for the 2D results evolved with the X14 network at three levels of grid refinement. The 1D result at 10 levels of grid refinement is also shown for comparison. The 2D values have been divided by 128 to account for the extra 128-cm extent of fluid that was burned relative to 1D. This data shows that although the distribution of energy release is different in 1D versus 2D, and at different levels of grid refinement, the total energy that is released is roughly the same. 103

Figure 5.12 Plot of the ^{16}O mass fraction resulting from an unsupported 3D detonation evolved with the Aprox13 network at 8 levels of grid resolution (5×10^7 g cm^{-3}). 105
Figure 5.13 Plot of the ^{28}Si mass fraction resulting from an unsupported 3D detonation evolved with the Aprox13 network at 8 levels of grid resolution (5×10^7 g cm^{-3}). 106

Figure 6.1 Explosion scenario proposed by Diehl et al. (2014). The ^{56}Ni produced during the He-belt detonation has large velocities like the rest of the matter in the outer ejecta, but its component in the line-of-sight of the observer is small because it is confined to an equatorial belt. 110
Figure 6.2 Log-Log plot of density vs radius for a WD with central density of 5×10^7 g cm^{-3} 112
Figure 6.3 Log-Log plot of pressure vs radius for a WD with central density of 5×10^7 g cm^{-3} 113
Figure 6.4 In order to represent a belt of He or Ni around the WD, it is only necessary to insert a "plug" of matter due to the 2D axisymmetry. . . 114
Figure 6.5 The red region represents a "belt" of He or Ni with a density of 2×10^6 g cm^{-3}. It is embedded into the WD until it reaches the density contour with the same value. 115
Figure 6.6 The crescent-shaped belts were created by using a hypothetical circle 3x the radius of the WD and offsetting it in the negative x-direction until its edge meets the desired density contour of the WD. The region of the WD that does not overlap with the larger circle is then filled with He. 116
Figure 6.7 Results from a typical simulation. Density is plotted in gray-scale and ^{56}Ni is pictured in the rainbow color scheme. The total mass of ^{56}Ni synthesized in the belt is calculated and this mass is separated into line-of-sight velocity bins to create histograms of its distribution. . . . 119

Figure 6.8 Results from model He-K. A detonation in the crescent-shaped He-belt produces a belt of ^{56}Ni with a similar shape, which reaches far from the equatorial region. 122
Figure 6.9 Results from model He-K. The FWHM shows that most of the belt-^{56}Ni has line-of-sight velocities below ∼9000 km s^{-1}. 123
Figure 6.10 Results from model He-I. Even with a geometrically confined belt, the He-detonation spreads the resulting ^{56}Ni far from the equator. 124
Figure 6.11 Results from model He-I. The FWHM shows that most of the belt ^{56}Ni has line-of-sight velocities below ∼7000 km s^{-1}. 125
Figure 6.12 Results from model He-C. Detonations in this geometrically confined, constant-density He-belt produces more ^{56}Ni than its stratified-density counterpart, but the ^{56}Ni is spread even further from the equator. . . 127
Figure 6.13 Results from model He-C. The FWHM shows that most of the belt ^{56}Ni has line-of-sight velocities below ∼12000 km s^{-1}. 128
Figure 6.14 Plot of proton number versus neutron number showing the isotopes involved in the 13-species network (red) and the 150-species network (sum of red and blue). 129
Figure 6.15 Comparison of the final results from models He-K and He-K-X150. . . 131
Figure 6.16 Results from model He-K. The FWHM shows that most of the belt ^{56}Ni has line-of-sight velocities below ∼7300 km s^{-1}. 132
Figure 6.17 Results from model He-K-X150. The FWHM shows that most of the belt ^{56}Ni has line-of-sight velocities below ∼7800 km s^{-1}. 133
Figure 6.18 A comparison of models He-K and He-K-X150, showing the first 0.5s of the evolution. 134
Figure 6.19 Results of model Ni-A. The belt of ^{56}Ni has been spread out by the explosion but the majority of its mass is still close to the equator. . . 136
Figure 6.20 Results from model Ni-A. The FWHM shows that most of the belt-^{56}Ni has line-of-sight velocities below ∼1800 km s^{-1} 137

Figure 6.21 Results from model Ni-C. The belt-^{56}Ni has not been spread out much by the explosion and so remains near the equator. 138
Figure 6.22 Results from model Ni-C. The FWHM shows that most of the belt-^{56}Ni has line-of-sight velocities below $\sim$2100 km s^{-1} 139
Figure 6.23 Results from model Ni-D. The belt-^{56}Ni has not been spread out much by the explosion and so remains near the equator. By increasing the density by 3$\times$ relative to model Ni-C, the belt-^{56}Ni resides deeper inside the remnant. 140
Figure 6.24 Results from model Ni-D. The FWHM shows that most of the belt-^{56}Ni has line-of-sight velocities below $\sim$700 km s^{-1} 141

Chapter 1

Introduction

Since the time of the Big Bang, the primordial elements hydrogen (H), helium (He), and lithium (Li) have been synthesized into heavier elements by thermonuclear reactions inside of the stars. The change of composition resulting from these reactions causes stars to evolve over the course of their lives. Although most stars burn through their nuclear fuel and end their lives quietly as inert, compact objects, others end their existence in explosive deaths. These stellar explosions are called supernovae and are among the most energetic events known to occur in our universe. They further synthesize the matter of their progenitor stars and distribute this material out into the interstellar medium of their host galaxies. In the process they generate $\sim 10^{51}$ ergs of kinetic energy, sending shock waves into their surroundings, thereby contributing to galactic evolution.

The fate of individual stars depends on their initial masses. Stars that are born with less than 8 solar masses (solar mass = $M_\odot$ = mass of sun = 2×10^{33} g) of material will first burn their H fuel into He and subsequently burn this He into carbon (C) and oxygen (O). If sufficiently massive, these stars can continue to burn some of the newly formed C into O, neon (Ne), and magnesium (Mg), but (due to their low masses) this is their final burning stage before the nuclear reactions cease. Without energy generation from the nuclear reactions, there is nothing to support the stars against their own self gravity and they begin to collapse. This continues until densities become large enough to force electrons into higher energy

states as demanded by the Pauli exclusion principle. These "degenerate" electrons become the dominant contribution to the pressure of the the collapsing stars, and it is this electron degeneracy pressure that finally halts the collapse. What remains after such an occurrence is a white dwarf; a hot, dense, inert ball of (mostly) C and O[1] (supported by degenerate electrons) that slowly radiates its existing thermal energy (generated from previous burning epochs) out into its surroundings. These objects compress roughly a solar mass of material into a volume the size of the Earth, with an average density and temperature of about 10^6 g cm^{-3} and 10^7 K. Although they are inert, we will see in the upcoming sections that these white dwarves can end their lives in thermonuclear explosions (Type Ia supernovae) under the right conditions. Stars that are born with more than 8 $M_\odot$ of material can have central densities and temperatures high enough to fuse elements as heavy as iron (Fe). After exhausting their fuel, these stars also begin to collapse, however, the electron degeneracy pressure is not sufficient to halt the inward fall of their massive cores. In this case, the collapse continues until the inner core is compressed slightly beyond nuclear densities (here, it is the neutron degeneracy pressure that halts the collapse), where it then rebounds, accelerating the inward falling material near the core outward into the remainder of the star. This "bounce", along with subsequent neutrino heating, powers these "core-collapse" supernovae. Explosions of these massive stars are a separate subject and will not be discussed further here.

Human knowledge of supernovae has accumulated over centuries of earth-based observations and more recently from space-based telescopes. The modern classification system of supernovae is based on their spectroscopic properties. The absence of H absorption lines in a supernova spectrum classifies it as a Type I event, while the presence of this feature classifies a Type II event (Figure 1.1). These two classifications are divided into subcategories based on further spectroscopic considerations. For instance, Type Ia supernovae are defined by the presence of strong silicon (Si) absorption lines in their early and peak spectra in addition to

[1] In general, a white dwarf is composed of the burning products that remain after its final stage of reactions (e.g. He, C/O, O/Ne, and O/Ne/Mg white dwarves are believed to exist) but in this work we will mostly be concerned with C/O white dwarves.

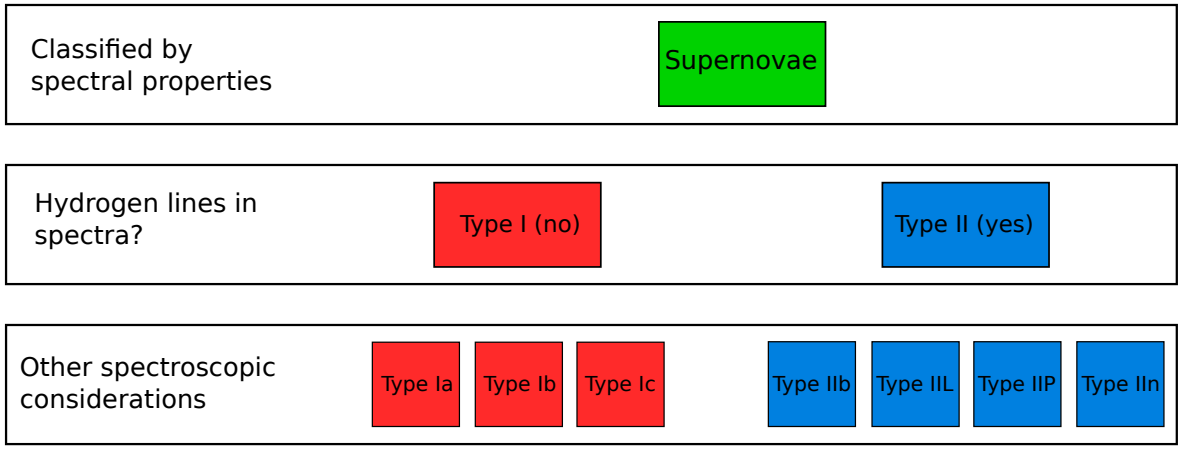


Figure 1.1: Classification system for supernovae. Type Ia supernovae are defined by the presence of strong Si absorption features in their early and peak spectra, differentiating them from all other Type I supernovae.

the absence of H (Filippenko, 1997). These Si lines are unique to Type Ia supernovae and so differentiate them from Type Ib/c events.

Type Ia supernovae (SNe Ia) are commonly attributed to thermonuclear explosions of C/O white dwarves (C/O WDs) in binary stellar systems and are among the brightest phenomena ever observed. Explosions of such objects can explain the lack of H in Type Ia spectra, and converting about 1 $M_\odot$ of C/O into Ni releases $\sim 10^{51}$ ergs of energy. These thermonuclear supernovae are unique among all other supernovae because they derive their explosion energies from nuclear energy release instead of the gravitational collapse of massive stellar cores. They are responsible for approximately 50% of the Fe production in the cosmos, and therefore play a significant role in galactic chemical evolution. Observationally, they can be used as cosmological distance indicators, providing unparalleled insight into the geometry and evolution of our universe.

1.1 Observations

Observations of Type Ia supernovae show a roughly homogeneous group of events, both spectroscopically and photometrically. Their light curves rise to peak brightness in ∼15-20 days, reaching an average magnitude of -19.3 with a variation of about 0.3 between events (Hillebrandt et al., 2013). This rise is followed by a similarly steep decline that transitions into an exponential decrease. Figure 1.2 shows this behavior for a group of nearby SNe Ia sampled at the Cerro Tololo Inter-American Observatory (Hamuy et al., 1993), and also illustrates a prominent correlation between light curve shapes and peak brightness (Phillips, 1993). The spectra of SNe Ia show large amounts of high-velocity (10-20,000 km s^{-1}) intermediate-mass elements (IMEs; elements between the C/O fuel and the Fe peak) at early times (Filippenko, 1997), and if detected early enough, even higher-velocity ($\gtrsim$ 25,000 km s^{-1}) C-features can be seen (Parrent et al., 2011; Silverman and Filippenko, 2012; Zheng et al., 2013). As the observations continue, the composition evolves toward heavier elements, until about two weeks after peak when the spectra are dominated by lower-velocity (5-10,000 km s^{-1}) iron-group elements (IGEs). It is believed that this behavior is due to light escaping from a dense but expanding remnant. Just after an explosion the remnant is so dense that it is opaque to electromagnetic radiation. However, as it expands, light can begin to escape first from the outer regions where densities are the lowest. Then, as the expansion continues, a photosphere recedes inward, emitting photons from deeper and deeper regions (Figure 1.3). This is why we see C-features if the event is detected promptly, IMEs at early times (corresponding to the outer regions of the remnant), and evolution toward IGEs at later times (as the receding photosphere reveals the inner regions). It is important to note that these IGEs are dominated by ^{56}Ni (∼0.3-0.9 $M_\odot$ for normal events), and it is the radioactive decay of this ^{56}Ni ($^{56}\text{Ni} \longrightarrow {}^{56}\text{Co} \longrightarrow {}^{56}\text{Fe}$) that is thought to power the optical light curves (see Churazov et al., 2014, for recent evidence).

The homogeneous observational properties that we just outlined only hold for "normal" (Branch et al., 1993) SNe Ia, making up about 70-75% of all events. There are also "peculiar" subclasses of SNe Ia that account for the remainder of the population (Li et al., 2011).

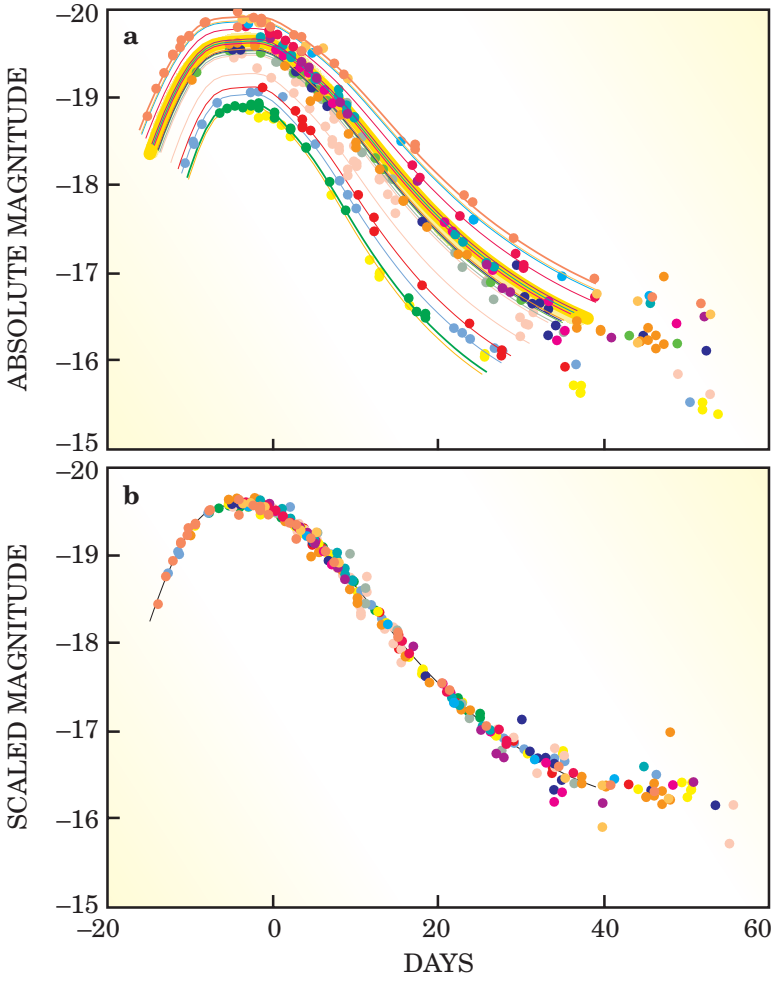


Figure 1.2: (a) Collection of nearby SNe Ia light curves as observed and (b) after parameter fitting. Hamuy et al. (1993)

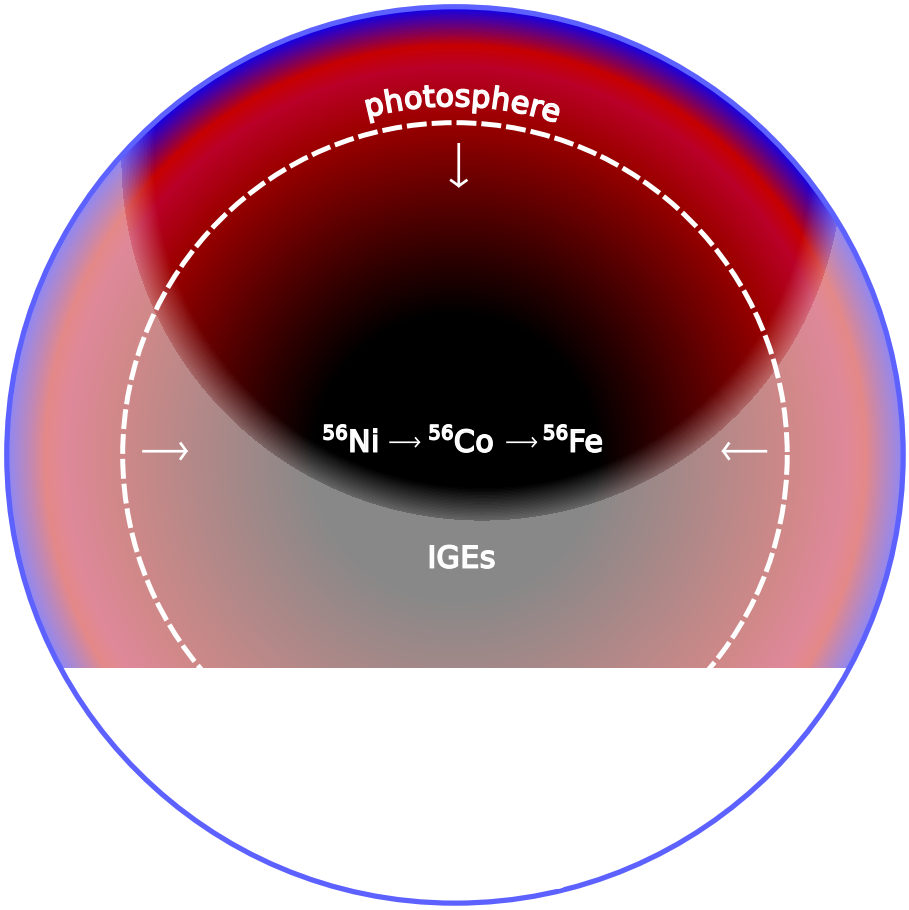


Figure 1.3: Cartoon depicting a dense, expanding SNe Ia remnant just after an explosion. The receding photosphere first shows the unburned C (blue) in the outer edge, followed by the IMEs (red), and subsequently IGEs (black)

About 20% of all events are noticeably dimmer than normal (∼1 magnitude fainter). These subluminous SNe Ia have faster declining light curves, higher amounts of IMEs and very little ^{56}Ni (∼0.1 $M_\odot$) relative to normal events. A prototypical example of this subclass is SN1991bg (Filippenko et al., 1992a). There are also SNe Ia that are much brighter than normal (∼1 magnitude brighter). These overluminous events, exemplified by SN1991T (Filippenko et al., 1992b), are very energetic and make up about 10% of the total Ia population. Their light curves rise and fall more slowly than normal and are estimated to produce as much as 1.5-1.8 $M_\odot$ of ^{56}Ni.

1.2 Cosmological Distance Indicators

In astronomy, a standard candle is an object whose intrinsic brightness is known, so its apparent brightness provides its distance through the inverse square law. Cepheid variables are one such example; their luminosity (directly related to intrinsic brightness) is related to the period of their oscillations in apparent brightness. Because there is a way to determine their intrinsic brightness, they can be used as distance indicators (standard candles). Although Cepheid variables can be about 100× as bright as the sun, they can only be seen out to distances of ∼30 Mpc. Type Ia supernovae, on the other hand, can be as bright as an entire galaxy, making them visible across the universe, up to distances of ∼10 Gpc. However, surveys of relatively nearby SNe Ia show that these events have variation in intrinsic brightness, so they are not "standard candles" as defined. Phillips (1993), however, determined a relationship between their intrinsic brightness and the shape of their light curves. He found that brighter SNe Ia have light curves that fall off more slowly after peak, whereas dimmer SNe Ia fall off more quickly. This "broader is brighter" relationship (Phillips relation) can be seen in Figure 1.2. By parameterizing SNe Ia light curves, their intrinsic brightness can be deduced, allowing their use as "standardizable candles" in observational cosmology. It is important to investigate the explosion mechanism that drives SNe Ia in order to refine our understanding of this relationship and what, if any, dependence it has on redshift.

1.3 Type Ia Explosion Mechanisms

Although there seems to be general agreement that SNe Ia arise from exploding C/O WDs, there is still no consensus on the path(s) that lead to explosion. But, if these C/O WDs are very stable, inert objects with no nuclear reactions occurring, what causes them to explode? As mentioned earlier, it appears that a companion star is required to drive them toward explosion, and it is the nature of the companion that divides the explosion scenarios into different categories. In the subsections that follow we will examine the most prominent of these scenarios and point out strengths and weaknesses of each of them.

1.3.1 Single-Degenerate Scenario

In the single-degenerate scenario (Wheeler and Hansen, 1971; Whelan and Icko, 1973), a C/O WD accretes matter (H or He) from a non-degenerate companion star (main sequence, giant, or He-burning star). This accreted matter is burned stably to C and O on the surface of the WD, thereby increasing its mass and central density. As the WD approaches the Chandrasekhar-mass[2], densities and temperatures near its center reach values where C-burning ignites. This ignition is followed by a phase of convective C-burning that lasts for centuries (Woosley et al., 2004) before eventually leading to a runaway that incinerates the entire object. The sequence of events that follows the onset of nuclear runaway is still uncertain, but in general, burning can proceed as a detonation or a deflagration. If a detonation occurs, a burning front will travel supersonically (driven by shock compression) through the WD. In this case, there is not sufficient time for the star to expand before it is processed entirely into IGEs (Arnett, 1969; Woosley and Weaver, 1986), in contrast to observations. Because they do not produce the IMEs observed in Type Ia spectra, pure detonations (in near-Chandrasekhar-mass WDs) are generally not accepted as a suitable explanation for thermonuclear supernovae. Deflagrations, on the other hand, propagate subsonically through the progenitor (driven by thermal conductivity and convection), leaving

[2]The Chandrasekhar-mass is the limiting mass beyond which the electron degeneracy pressure can no longer support a star against its own self gravity. For a C/O WD, this value is 1.4 $M_{\odot}$.

adequate time for the star to expand as the flame advances. This expansion causes some of the burning to occur at lower densities, leaving behind IMEs as observed. Hillebrandt and Röpke (2005) have shown that pure deflagrations can generate enough energy to explode a WD but does not produce enough ^{56}Ni to power the observed light curves, except perhaps in the lowest energy events. Another obstacle facing pure deflagration models is that a substantial amount of mixing occurs in the simulated ejecta (due to large-scale convection), which is inconsistent with the stratified composition inferred from the spectra (Stehle et al., 2005).

Due to these contrary results, it seems the most probable mechanism to explode a near-Chandrasekhar-mass WD via the single-degenerate channel is a turbulent deflagration which transitions into a detonation (Hillebrandt and Niemeyer, 2000) at some point during the explosion. The initial deflagration serves to "pre-expand" the WD as it burns subsonically, decreasing the density in the outer regions. Then, when the transistion to a detonation occurs, the remainder of the star in incinerated at these lower densities, resulting in a central region of ^{56}Ni (and other IGEs) surrounded by a substantial amount IMEs (from incomplete burning). The amount of pre-expansion determines how much ^{56}Ni will be provided by the explosion, and this ^{56}Ni establishes the luminosity of the event. There are several different variations of this deflagration-to-detonation transition (DDT) mechanism, each defined by the way in which the transition occurs; e.g. delayed-detonation (Khokhlov, 1991), gravitationally-confined detonation (Plewa et al., 2004), pulsating-reverse detonation (Bravo and García-Senz, 2006). For instance, in the delayed-detonation model, the subsonic flame is eventually torn apart by turbulence as it travels into the low-density fuel in the outer regions of the WD, leading to a spontaneous transition to a detonation. However, the DDT mechanism is poorly understood even in terrestrial combustion studies, so the transition to detonation must be manually implemented, leaving the critical density (ρ_c) at which the transition occurs as an unknown parameter: Previous studies suggest (Gamezo et al., 2005) that $\rho_c \sim 10^7$ g cm^{-3} can produce results consistent with SNe Ia observations. Such parameterized models have been shown to reliably match light curves and elemental

abundances (Kasen et al., 2009), but further investigation is needed to help establish a theoretical understanding.

In the past, the single-degenerate explosion scenario was favored due to its ability to explain the homogeneity among SNe Ia observations; explosions of near-Chandrasekhar-mass WDs (similar initial conditions) produce similar results. However, large SNe Ia surveys conducted over the last decade have pointed out the diversity of these events, opening the door for other explosion scenarios to account for (at least) peculiar events. There are also concerns of whether this scenario alone can produce the observed rate of normal SNe Ia, especially with the narrow range of mass transfer rates that are required for a successful explosion (Ruiz-Lapuente, 2014). In addition, studies of the observed delay-time distribution show a bimodal behavior, with a prompt (<500 Myr) and delayed (> 800 Myr) population. The evolutionary path of a binary system leading to explosion via the SD channel has difficulties explaining this temporal distribution. Thus, it seems likely that more than one progenitor scenario contributes to the overall SNe Ia population.

1.3.2 Double-Degenerate Scenario

In the double-degenerate scenario, the companion star is another WD, and it is the merger of the two WDs that leads to a thermonuclear explosion in this case (Webbink, 1984; Iben and Tutukov, 1984). The merger can occur under various circumstances. In the traditional version, the two WDs (with combined mass greater than the Chandrasekhar mass) slowly spiral inward toward each other as the system loses energy through the emission of gravitational waves. Eventually, the secondary (less massive) WD approaches too closely to the primary and is torn apart by their gravitational interaction, forming a thick accretion disk around the primary[3]. The primary gains mass through this accretion, and as it approaches the Chandrasekhar mass, C-burning ignites near its center and gives rise to a SNe Ia. However, the high mass transfer rate that this implies ($\dot{M} \sim 1{\times}10^{-5}$ $M_\odot$ yr^{-1}) should

[3]The mass transfer is expected to occur in a runaway manner because a WD increases its radius (and decreases its Roche lobe) as it loses mass.

cause a C-deflagration in the outer region of the merged object that would travel slowly inward, converting the C/O WD into an O/Ne/Mg WD. In this case, as the Chandrasekhar mass is approached, this object would collapse to form a neutron star (Saio and Nomoto, 1985) instead of producing a thermonuclear supernova.

Recent simulations, however, have shown that double WD systems with mass ratios near unity can lead to violent mergers (Pakmor et al., 2010, 2011, 2012). In this case, the secondary WD is torn apart just before the objects make contact, and the in-falling material directly impacts the surface of the primary. This leads to thermodynamic conditions suitable for a detonation to occur *during* the merger that incinerates the entire object. It is important to note that the primary WD is essentially unaltered by the merger, so the detonation occurs in a sub-Chandrasekhar-mass WD (densities $\lesssim 5{\times}10^7$ g cm^{-3}) surrounded by the disrupted matter of the secondary. As we will see in the next subsection, simulations of pure detonations in sub-Chandrasekhar-mass WDs produce explosion energies and isotopic yields that can agree with observations. These violent merger simulations have revived the double-degenerate scenario after its having fallen out of favor for decades. In addition, binary population studies (Ruiter et al., 2012) have shown this scenario to agree with the observed SNe Ia rate, but only if *all* mergers (total mass above or below the Chandrasekhar-mass) lead to SNe Ia. This is far from certain, however, as detonations in (even the most likely) violent merger models must be manually ignited (due to unresolved length scales) once thermodynamic conditions are believed to be suitable.

Another possible mechanism that falls into this category is the collision of two WDs. This might be realized in regions of high star density such as galactic centers or globular clusters (Benz et al., 1989), or possibly in triple-star systems (Thompson, 2011). Although most studies (e.g. Benz et al. (1989); Lorén-Aguilar et al. (2010); Raskin et al. (2009, 2010); Rosswog et al. (2009)) show these systems would lead to atypical SNe Ia events, recent work by Katz and Dong (2012) and Kushnir et al. (2013) show that collisions in triple-star systems might be capable of reproducing the observed SNe Ia rate.

1.3.3 Double-Detonation Scenario

In the double-detonation scenario a C/O WD stably accretes He from either a He-burning star or a He-rich WD, which builds up a layer of He on its surface. Compressional heating near the bottom of this layer, or direct impact of the accretion stream onto the WD, might lead to a He-detonation. This surface detonation is believed to be capable of inducing a subsequent detonation in the underlying C/O core, which then incinerates the entire object before reaching the Chandrasekhar-mass, producing a SNe Ia. This secondary detonation can be ignited either directly, as the He-detonation transitions into a C-detonation at the He-C/O interface ("edge-lit" case), or due to compression of the core as a converging shockwave (produced as the He-detonation travels around the WD surface) meets somewhere off-center ("core-compression" case). Unlike the single-degenerate scenario, which involves a Chandrasekhar-mass WD, pure detonations in these sub-Chandrasekhar-mass WDs (with lower densities) are capable of producing IMEs in the outer ejecta. Sim et al. (2010) simulated detonations of naked sub-Chandrasekhar-mass C/O WDs ranging from 0.81-1.15 $M_{\odot}$. They showed that, along with a substantial amount of IMEs, such detonations were capable of producing ^{56}Ni masses that correspond to the known range of SNe Ia luminosities. However, they did not include the initial He-detonations (or the resulting ashes) in their models. Traditionally, when the He-detonations are included in models, they produce a significant amount of IGEs (including ^{56}Ni) in the outer ejecta. These IGEs are the results of burning the massive (0.1-0.2 $M_{\odot}$) He-shells that were previously believed necessary to ignite and sufficiently strengthen the initial He-detonation. However, simulations by Fink et al. (2010) have recently shown that detonations can propagate in very thin He-shells ($\sim$0.005 $M_{\odot}$), which robustly lead to secondary detonations of the C/O core via core compression. Due to the lower masses of these He-shells, and the lower densities that this implies, incomplete burning leaves behind relatively little IGEs and no ^{56}Ni (Fink et al., 2010), resulting in much better agreement with observations. However, a remaining obstacle for this explosion models is the overproduction of ^{44}Ti, which is not seen in normal SNe Ia Kromer et al. (2010).

1.4 SNe Ia Simulations

It is clear from the previous section that detonations play a critical role in most SNe Ia explosion scenarios, and therefore it is important to study them. However, simulating thermonuclear supernovae is complicated by a range of length scales that spans roughly 10 orders of magnitude. The progenitor WD that is to be exploded has a radius of $\sim 10^8$ cm while the detonation fronts can be less than $\sim 10^{-1}$ cm. Even with our most advanced computing capabilities it is impossible to resolve these microscopic burning fronts in full-star simulations. Therefore, the shock interface is typically modeled as a discontinuity between fuel and ashes that is spread out numerically over several computational zones. The resolution of these zones is $\sim$1 km in the most expensive models. In order to evolve the unresolved nuclear burning that occurs in these simulations one can employ a nuclear reaction network (of various sizes) that is solved *in situ* during the calculations or use an approximate model of the burning. The latter approach is computationally less expensive but the fidelity of the results can be compromised due to inaccurate feedback of nuclear energy into the fluid and the altered abundances that this implies

1.5 Outline

In Chapter 2, we will give the necessary background information on detonation theory in preparation for discussions in the upcoming chapters. Chapter 3 investigates numerical complications that can arise when modeling reactive, astrophysical shocks. The results of this chapter will help inform our decisions of how to handle such issues during the remainder of this work. Chapter 4 focuses on how resolution and the fidelity of nuclear kinetics can affect the outcome of 1D detonations, while Chapter 5 is concerned with how the 1D results can be altered when moving into higher dimensions where burning occurs in a cellular mode. In Chapter 6, we apply what we have learned to an astrophysical problem and we conclude in Chapter 7.

Chapter 2

Detonation Theory & Previous Work

A detonation is a supersonic mode of combustion in which a compressed, reactive shock induces chemical or nuclear reactions as it moves into a fuel source, and it is the energy released by these reactions that sustains its propagation. The first theoretical model of detonations was developed by Chapman (1899) and Jouguet (1905) at the turn of the twentieth century (CJ-theory). In this 1D model, the shock is represented by a sharp discontinuity between burned (ashes) and unburned (fuel) material. As the shock moves into the fuel, the reactions occur instantaneously, releasing all energy and leaving completely burned ashes behind it. Given the energy released by burning fuel into ash, the detonation velocity and post-shock thermodynamic state can be obtained, however, this model fails to describe the structure of the detonation (e.g. reaction zone). The work of Zel'dovich (1940), von Neumann (1942), and Döring (1943) expanded on CJ-theory by allowing burning to proceed according to appropriate reaction rates (i.e. over a finite interval of time) after the passage of the discontinuous shock, thereby describing a finite reaction zone with an extended thermodynamic profile behind the shock (ZND-theory). In this 1D model, a *burning length* can be defined as the product of the detonation velocity and the total time to achieve a particular ash state.

The properties of such detonations can be determined by considering the conservation equations for mass, momentum, and energy flux at the shock interface. Assuming a frame

of reference where the shock is stationary, these equations are, respectively,

$$\rho_0 D = \rho(D - u), \tag{2.1}$$

$$P_0 + \rho_0 D^2 = P + \rho(D - u)^2, \tag{2.2}$$

and

$$E_0 + P_0 V_0 + \frac{1}{2}D^2 + q = E + PV + \frac{1}{2}(D - u)^2. \tag{2.3}$$

The variables with a "0" subscript represent the fuel conditions and the non-subscripted variables represent the conditions of the ashes, where P is the pressure, V is the volume, ρ is the specific density (1/V), u is the fluid velocity, E is the specific internal energy, D is the detonation velocity, and q is the specific energy released from burning the fuel to a particular ash state. By eliminating the fluid velocity, u, from equations (2.1) and (2.2) we obtain the *Rayleigh Line*,

$$\mathcal{R} = (P - P_0) - \rho_0^2 D^2 (V_0 - V) = 0, \tag{2.4}$$

which represents the fluid conditions inside the reaction zone after the passage of a shock moving into a fuel (of given initial conditions) with velocity D. By using equations (2.1) and (2.2) to eliminate the fluid velocity, u, and detonation velocity, D, from equation 2.3, we obtain the equation for the *Hugoniot curve*,

$$\mathcal{H} = (P - P_0)(V - V_0) - 2(E_0 - E + q) = 0. \tag{2.5}$$

This equation represents all possible fluid states behind the shock after energy q has been released from burning a fuel with given initial conditions. It is the intersection of the Rayleigh line with different Hugoniot curves (corresponding to different values of q) that describe the actual post-shock fluid conditions for a specific detonation.

Figure 2.1 shows a Hugoniot curve representing the final state of the fluid behind the shock after all reactions have finished, releasing energy q. There are also three Rayleigh lines shown with different slopes ($-\rho_0^2 D^2$) corresponding to different detonation velocities. The blue

Rayleigh line has a detonation velocity that is too small to intersect the Hugoniot curve and, therefore, does not represent a physical solution based on the assumptions of our initial conditions and energy release. The green Rayleigh line is tangent to the Hugoniot curve and so intersects it at a single point. The detonation velocity corresponding to this Rayleigh line is the one predicted by CJ-theory (D_{CJ}), and represents the minimum possible speed for the detonation. For this unique solution, there is a sonic point at the end of the reaction zone and, therefore, all energy released by the burning contributes to its propagation. For C/O fuel with initial densities less than 2×10^7 g cm^{-3}, self-sustained detonations travel at this speed. Above D_{CJ}, the Rayleigh line intersects the Hugoniot curve at two points marked S (strong) and W (weak) in Figure 2.1. Detonations corresponding to the strong point are *overdriven* and are characterized by an overdrive parameter $f = (\frac{D}{D_{CJ}})^2$. They do not have a sonic point in the reaction zone so the flow is subsonic relative to the shock. Therefore, disturbances can catch up to and influence the shock. Detonations corresponding to the weak point can be shown to be unphysical and so they are disregarded (Fickett and Davis, 1979). For fuel densities greater than 2×10^7 g cm^{-3}, Si-reactions become endothermic due to photodissociations, causing a sonic point within the reaction zone. These detonations are *pathological* and travel at speeds $D_P > D_{CJ}$ for the self-sustained case. Although greater than D_{CJ}, pathological detonation velocities only exceed D_{CJ} by a few percent. For such detonations, the overdrive parameter is defined as $f = (\frac{D}{D_P})^2$.

Figure 2.2 shows a Rayleigh line plotted along with two Hugoniot curves. Curve S is an adiabat representing the possible fluid states before any reactions have occurred (equation 2.5 with $q = 0$) while curve NSE represents a post-shock adiabat where burning has reached completion. The initial state of the ashes are represented by the point labeled IC, and the Rayleigh line must pass through (and pivot from) this point. After the passage of the shock, the fluid conditions jump to point Sh on the shock adiabat that is determined by the detonation velocity, D (because the slope of the Rayleigh line is $-\rho_0^2 D^2$). This point represents the post-shock conditions just behind the shock but before any reactions have

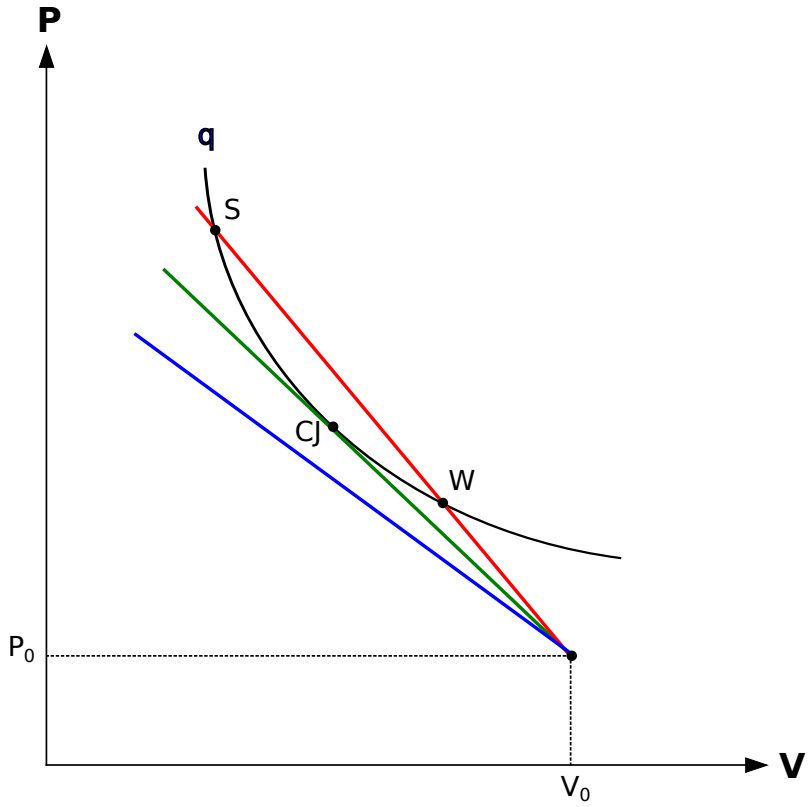


Figure 2.1: P-V diagram showing three different regimes for a given detonation velocity.

occurred. The state of the fluid then moves down the Rayleigh line until it intersects the Hugoniot curve (NSE) where it has reached its final state at point F.

Despite the many successes of these 1D models, they do not fully agree with experimental results. Real (i.e. multi-D) detonations exhibit a complex cellular pattern within their reaction zones and can propagate at a slightly reduced speed relative to 1D results. A physical burning front consists of alternating regions of Mach stems and incident shocks connected by transverse waves that extend back into the reaction zone (see subsection 3.2.2 and Figure 3.7). The points where these three structures meet are called triple-shock configurations, or triple-points, and it is the paths of these high-pressure points which trace out a characteristic cellular pattern (see Section 2.2). Cellular detonations were first observed in terrestrial gases by Denisov and Troshin (1959) and Voitsekhovskii et al. (1963). The cellular pattern can be recorded experimentally, for example, as the triple-points etch their paths on the inside of soot covered "flame-tubes" (Fickett and Davis, 1979). Computational studies (Oran et al., 1998; Gamezo et al., 1999a) show that cellular burning can create low-pressure pockets of unreacted gas, the presence of which increases the length of the reaction zone compared to 1D results and can play an important role in the propagation and extinction of detonations. Gamezo et al. (1999a) noted that the cell sizes and regularity of the final structure were only dependent on the chemical kinetics, and not on the peturbations used to disrupt the initially planar detonation front.

Boisseau et al. (1996) were the first to demonstrate the existence of cellular detonations in degenerate C/O fuel, representative of SNe Ia environments. They compared their results to the previous 1D studies of Khokhlov (1989), who calculated three distinct burning lengths ($x_C \ll x_O \ll x_{Si}$) corresponding to the burning time scales for C, O, and Si[1]. Analogous to terrestrial detonations, Boisseau et al. (1996) showed that cellular burning created pockets of incompletely burned material which increased the length of the C-burning region, slightly decreased the detonation velocity, and changed the resulting composition relative to 1D results. Similar to Gamezo et al. (1999a), the structure that developed was shown to depend

[1]This wide range of time scales will be important to the physics discussed in upcoming chapters.

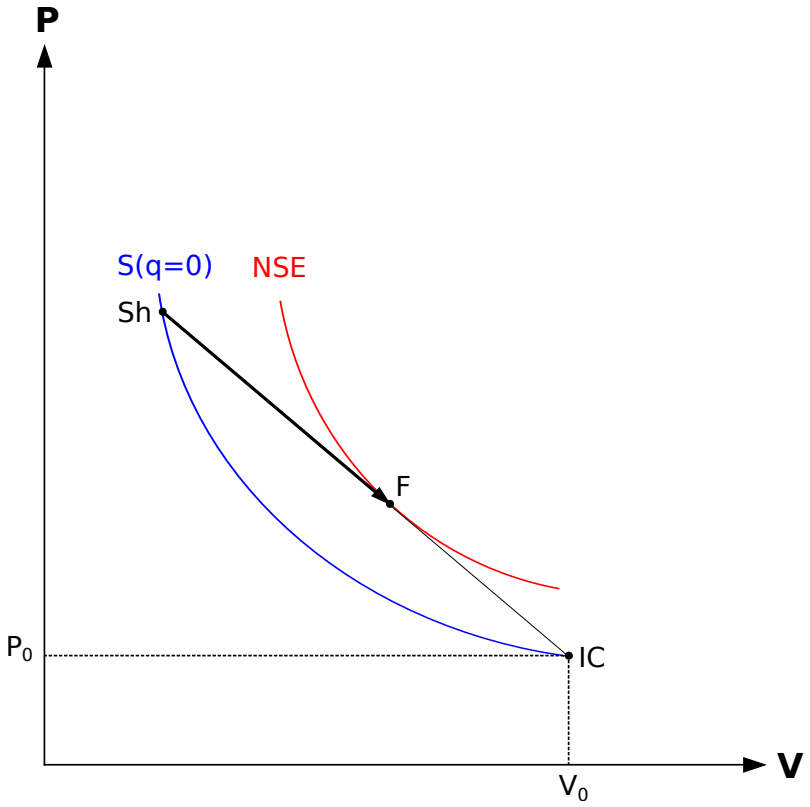


Figure 2.2: P-V diagram showing the path taken by a fluid element as a reactive shock front passes.

only on the material properties, and was independent of the initial perturbation, grid size, and boundary conditions. Although only the C-burning region was resolved in their study, Boisseau et al. (1996) speculated on the importance of the Si-burning cells, expressing the need to investigate their role in DDT models and detonation quenching.

Performing simulations of C/O detonations at low SNe Ia densities ($1 \times 10^6 - 3 \times 10^7$ g cm^{-3}), Gamezo et al. (1999b) investigated the different cell sizes corresponding to the 1D C-, O-, and Si-burning regions. They found that cellular structure increased the length of the C- and O-burning regions by a factor of 1.6 and the Si-burning region by a factor of 1.3 relative to 1D results. The increased burning lengths imply that incomplete burning can occur at higher densities than determined from 1D calculations. Gamezo et al. (1999b) explained that, considering these revised results, fits of delayed-detonation models to observation would yield a higher critical density at which DDT can occur. They estimated that ρ_c could be increased by $\sim$6% when the Si-length is increased by $\sim$30%. They also anticipated increased mixing of species due to the presence of incomplete and complete burning regions in the reaction zone, and suggested that this could be observable in the final composition distribution and velocities of the ejecta. The incomplete energy release from low-density burning was found to create conditions sufficient for detonation extinction in some cases.

Timmes et al. (2000b) simulated cellular detonations in pure C to investigate how spatial resolution might affect such simulations. With a fuel density of 10^7 g cm^{-3}, they showed that the size of the burning cells were not significantly affected over the range of resolutions they considered (10^{-1} - 1.25×10^{-2} cm), but the main features of the detonation front were strongly dependent. The curvature of the weak incident shocks and the strength of the triple-points and transverse waves were all shown to be influenced by the spatial resolution, and the differences between the incomplete and complete burning regions were also affected. These results help to define the minimum resolution necessary for multi-D SNe Ia models involving cellular detonations.

Chapter 3

Burning Within Numerical Shocks

As discussed in Section 1.4, simulating detonations in astrophysical environments can be complicated by numerical approximations to shock structure. A common prescription to ensure correct detonation speeds and associated quantities is to prohibit burning inside the numerically broadened shock. In this chapter, we present a series of simulations intended to verify the efficacy of this approximation and to understand how resolution and dimensionality might affect its use[1].

3.1 Introduction

Shocks are ubiquitous in astrophysical settings. In particular, the mechanisms which drive events such as novae, x-ray bursts, and Type Ia supernovae are all posited to involve detonations, a supersonic burning regime maintained by energy release from the propagation of a compressed, reactive shock. In all these cases, the explosive events are powered by rapid thermonuclear energy release and, therefore, share several characteristics. Here, we restrict our immediate attention to the most energetic of these thermonuclear events – thermonuclear supernovae – but the bulk of our results are generally applicable.

[1]Note that this material appeared in Papatheodore and Messer (2014).

Modern hydrodynamics codes are capable of realistically modeling such stellar detonations, however, numerical approximations to shock structure can threaten the fidelity of such simulations if not properly treated. A *physical shock* is considered to be infinitesimally thin under such conditions, so fuel spends very little time within the shock itself as the detonation propagates. This means that an insignificant amount of burning occurs naturally inside of a shock. The width of a *numerical shock*, however, is constrained by the hydrodynamics scheme and spatial resolution employed in a simulation. For example, an Eulerian PPM scheme typically artificially widens a shock to approximately 2-4 computational zones, so on a sufficiently coarse grid an appreciable amount of burning may occur inside the shock (for other methods, the shock can be spread to 20 zones or more (see Oran and Boris, 2000). Any burning that takes place within the numerical shock does so under erroneous thermodynamic conditions since the density and temperature have not yet reached their post-shock values where the reactions would physically occur.

Astrophysical shocks are very often under-resolved because of the disparity of scales in these problems, and therefore the discrepancy between real and numerical shock structure can lead to behavior that is not realized in nature. Specifically, Fryxell et al. (1989) showed that energy deposition in the leading edge of an under-resolved C-burning shock can generate a secondary shock structure, but is a numerical artifact, that propagates ahead of the true shock at speeds greater than the Chapman-Jouguet velocity. These results are unacceptable since both the increased detonation speed and double shock sequence disrupt the structure of the reaction zone. Behind the location of the true shock, the resulting abundances and thermodynamic state converge to the correct values when evolving the simulation with a conservative method, but conclusions which depend on specific aspects of the propagation and reaction zone details will be fundamentally flawed and possibly misinterpreted. A common prescription to ameliorate these nonphysical results is to prohibit burning inside of a numerical shock (Fryxell et al., 1989), ensuring that burning does not occur until the correct post-shock conditions are reached. This approach eliminates the secondary shock structure and restores the proper detonation speed to the models. This remedy is especially relevant

for astrophysical simulations where burning lengths are often smaller than the numerical shock width.

Here, we explore the effects of modifying the burning prescription in both 1D and 2D detonation simulations in order to fully understand the ramifications of this prescription, and, in particular, its effect on cellular burning. Simulations which intend to inform sub-grid flame models (for use in full-star simulations) with realistic detonation input must be capable of capturing the dynamic cellular burning front when densities of interest are such that detonation cellular sizes become comparable to scales just below the spatial resolution actually achieved in full-star simulations. As we shall see, an arbitrary prohibition on burning within a simulated shock can have a direct effect on the formation of cellular structure due to numerical considerations.

3.2 Simulations

1D and 2D detonations were modeled in a numerical laboratory which approximates conditions in the outer reactive regions of SNe Ia[2]. The fuel consisted of a 50-50 C/O composition at rest with a temperature of 1×10^7 K. Fuel densities were chosen separately for the 1D and 2D cases to demonstrate two distinct issues that can arise when modeling reactive shocks. The computational domain spanned 6144 cm in length by 128 cm wide with reflecting boundary conditions at the left (ash) end, outflow at the right (fuel) end, and periodic conditions along the length at $y = 0$ and $y = 128$ cm. This setup was chosen to resemble a small section of a detonating WD with adequate resolution to track the details of the reaction zone. Figure 3.1 illustrates the setup, including only a small section of the domain so that the match head region and the structure of the adaptive mesh may be discerned. The detonations were ignited by a "match head" region with a temperature and x-velocity of 1×10^{10} K and 1×10^9 cm s^{-1} at the left end of the domain. After, ignition, these detonations evolved to their self-sustained conditions (Sharpe, 1999) as they

[2]These simulations, as well as all others in this work, were implemented using the FLASH code (see Appendix 7

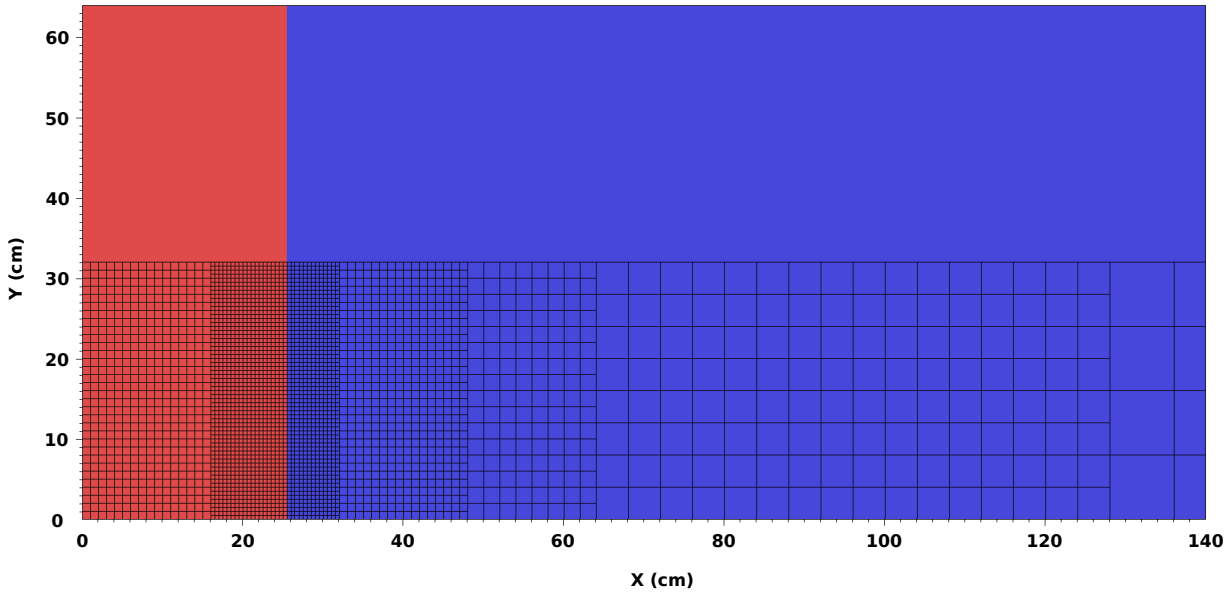


Figure 3.1: Temperature as a function of position for a small section of the problem setup along with the adaptive mesh (shown only on the bottom of the figure). Red (1×10^{10} K) denotes the "match head" region used to ignite the fuel shown in blue (1×10^{7} K).

propagated down the "tube". Nuclear kinetics were advanced according to a 13-isotope α-chain plus heavy-ion reaction network, Aprox13, which has been shown to capture energy generation rates for C and O comparable to larger networks without their computational burden (Timmes et al., 2000b). The reactions included (α, γ) and $(\alpha, p)(p, \gamma)$ links as well as their reverse sequences among the 13 isotopes ^{4}He, ^{12}C, ^{16}O, ^{20}Ne, ^{24}Mg, ^{28}Si, ^{32}S, ^{36}Ar, ^{40}Ca, ^{44}Ti, ^{48}Cr, ^{52}Fe, and ^{56}Ni.

3.2.1 1D

We simulated 1D detonations with fuel densities of 1×10^{9}, 5×10^{8}, 1×10^{8}, and 5×10^{7} g cm^{-3} in order to quantify and explain the issues found by Fryxell et al. (1989) in under-resolved numerical shocks for a variety of SNe Ia regimes. These simulations were performed with a maximum spatial resolution of 0.5 cm, with burning allowed and then forbidden within the numerical shock. With no restrictions on burning, the 1×10^{9} and 5×10^{8} g cm^{-3} models were both found to exhibit the characteristic secondary shock wave described by

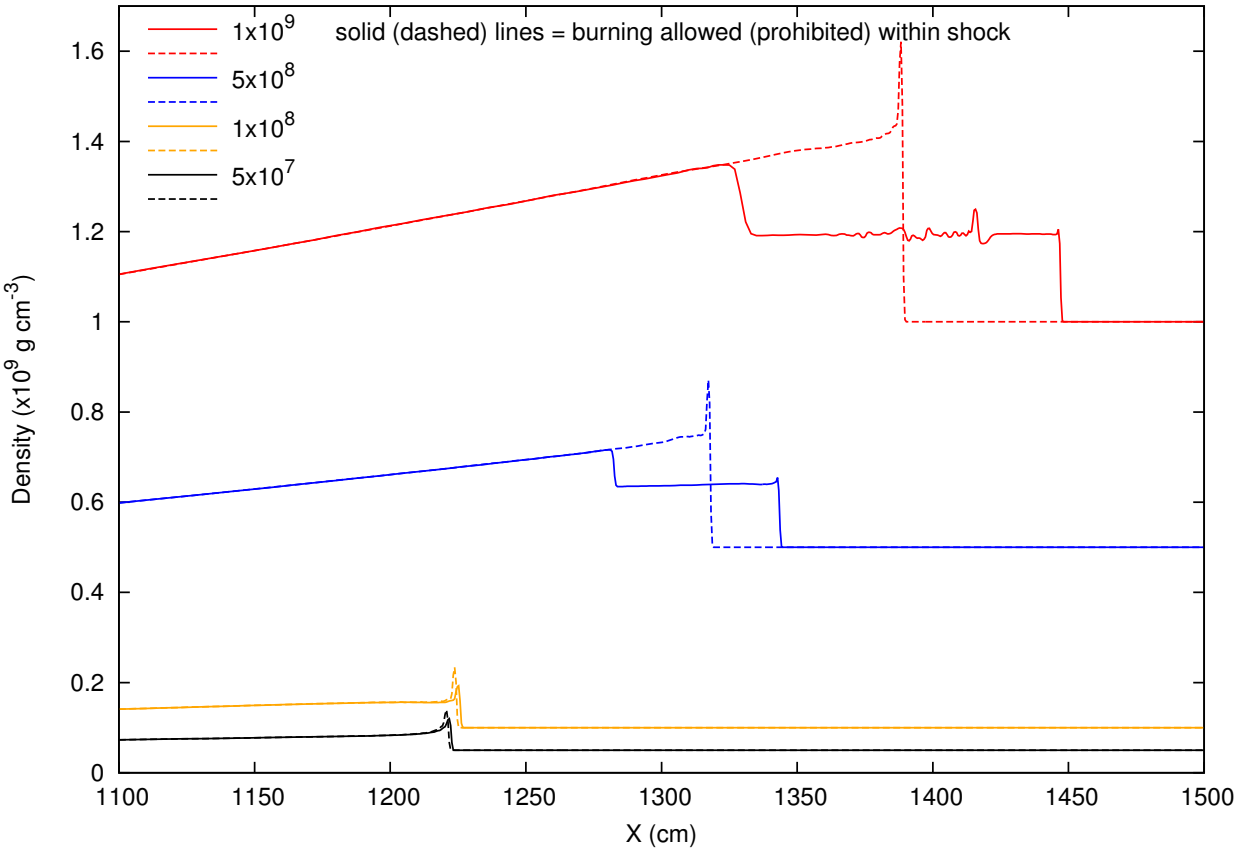


Figure 3.2: Results from the 1D simulations showing the secondary shock structure in the density profile due to unresolved C-burning (0.5-cm resolution) at t $\sim 10^{-6}$s. The solid curves show the outcome when shock burning is allowed and the dashed curves show the results when burning is prohibited in the shock. The different pairs of curves correspond to the different initial fuel densities of 1×10^9, 5×10^8, 1×10^8, and 5×10^7 g cm^{-3}. We can see that preventing burning in the shock eliminates the nonphysical shock structure in the two higher-density simulations, leading to the correct detonation velocity and physically acceptable results.

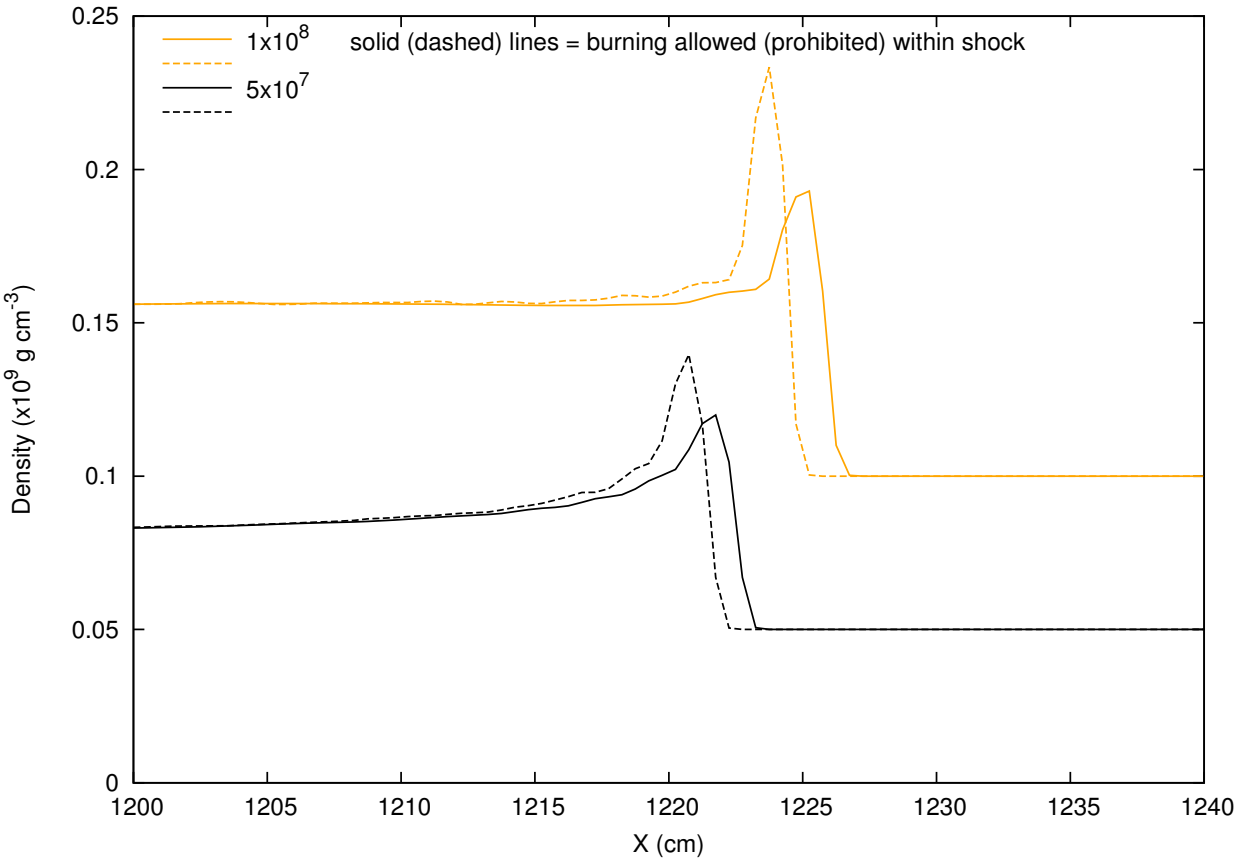


Figure 3.3: A zoomed in view of the density profiles from the 1×10^8 and 5×10^7 g cm^{-3} simulations. Although they do not show a secondary shock, there are differences in their peak values corresponding to premature burning conditions inside the shock as opposed to the proper post-shock conditions.

Fryxell et al. (1989) while the lower-density models did not. With burning prohibited in the shocks, the nonphysical shock waves were eliminated and correct detonation velocities were restored to the affected higher-density models, again in agreement with the results of Fryxell et al. (1989). This behavior is illustrated in Figure 3.2 which shows the resulting density profiles from the simulations. The solid and dashed curves in this figure correspond to the cases where burning within the shock is allowed and forbidden, respectively. Figure 3.3 is a magnified view of the lowest-density profiles, showing that although the two lower-density models do not exhibit a secondary shock, they differ in peak density since the case with burning within the shock forbidden processes the fuel at post-shock conditions while the case which allows burning in the shock does so under premature conditions. The observed offset of the front position between the two cases (with burning allowed and forbidden within the shock) is due to the numerical extent of the shock.

Significant adverse effects due to burning within the shock are only observed for the higher-density models since their C-burning lengths are smaller than those at lower densities. This allows a significant amount of C to be burned in the leading zones of the shock on a sufficiently coarse grid, creating a secondary shock structure. The speed of the nonphysical shock is greater than the CJ-velocity and is resolution-dependent (LeVeque et al., 1998), confirming it as a numerical artifact. Although the lower-density models are not afflicted by a secondary shock, it should be noted that all of these detonations are under-resolved. This can be seen in Figure 3.4 which shows the maximum value of nuclear energy generation versus simulation time for $\rho_i = 5 \times 10^7$ g cm^{-3} at three different grid resolutions. Only the 0.03125-cm model is well enough resolved that the energy release has converged to the correct value. The oscillations in this figure are a numerical consequence of stepping through individual computational zones at the detonation front at discrete time intervals.

3.2.2 2D

We simulated 2D detonations to determine how the treatment of burning in and around the numerical shock might affect cellular structure. First we performed a series of simulations

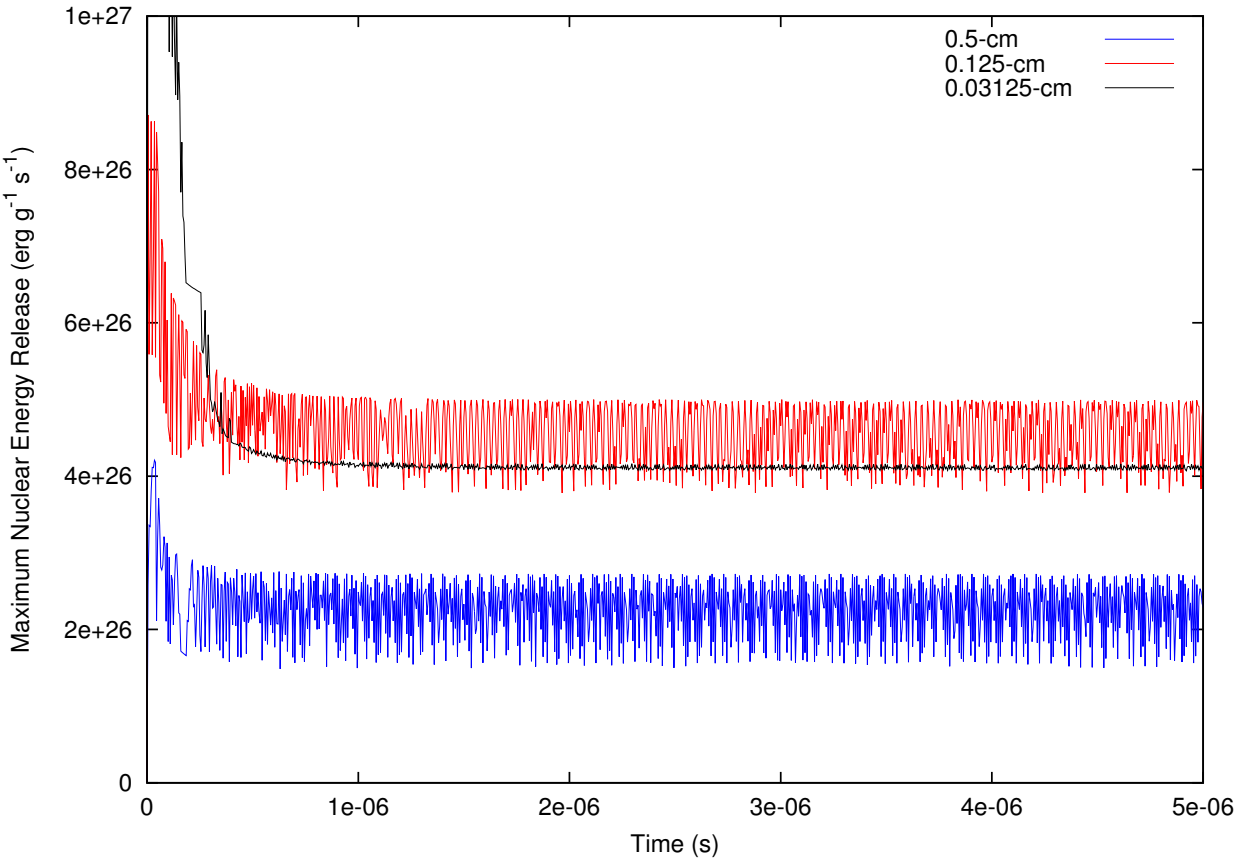


Figure 3.4: Maximum of nuclear energy release rate versus time for the $\rho_i = 5 \times 10^7$ g cm^{-3} simulation with 0.5-, 0.125-, and 0.03125-cm maximum resolution. At 0.5-cm resolution the energy release is under-resolved and at 0.03125-cm and above the rate has converged to its steady value.

without explictly perturbing the fuel, although numerical noise from roundoff errors can be sufficient to seed the transverse instability (Gamezo et al., 1999a) that leads to cellular burning. For comparison, we then performed a second series in which fuel perturbations were explicitly defined. The perturbation was a 5-cm wide region, placed 20 cm in front of the match head, in which the density of each zone was assigned a random value from a range 1% above to 1% below the density assigned to the rest of the flame tube. The detonations propagated in to fuel with a density of 5×10^7 g cm^{-3} and were simulated with burning allowed and forbidden within the shock as spatial resolution was improved. At this density, the grid was sufficiently refined to prevent the development of a secondary shock over the range of resolutions that we considered, thereby eliminating 1D complications from the results.

Here we have restricted our attention to densities greater than 2×10^7 g cm^{-3} (pathological regime) to avoid using over-driven detonations (Domínguez and Khokhlov, 2011). Indeed, all of our detonations begin with over-driven initial conditions but eventually relax to a steady, self-sustained state at which they propagate. At densities below 2×10^7 g cm^{-3}, our detonations decay and are eventually quenched as the over-driven support diminishes with time. It is possible to include constant support to these low-density detonations: Gamezo et al. (1999b) effectively support their simulated detonations at low densities (1×10^6 - 3×10^7 g cm^{-3}) by utilizing a moving grid. However, the structure of supported detonations differ from their unsupported counterparts (higher temperatures lead to decreased burning lengths and change the subsequent energy release; Sharpe, 1999). Therefore, we choose a density range to make connections with earlier works and to clearly delineate the effects of burning in numerical shocks.

The results from the unperturbed series can be seen in Figure 3.5. At the lowest level of resolution (0.5-cm) we observed that cellular structure was not established in either case, whether burning was allowed or forbidden within the shock. At 0.125-cm resolution the main difference between the two cases is apparent in that cellular structure developed where burning was allowed within the shock but did not develop where it was prohibited. At the

highest resolution (0.03125-cm) cellular structure was observed in both cases. The results of the perturbed series were similar to those of the unperturbed series, except that only the 0.5-cm resolution simulations showed the discrepancy between the two cases, where burning was allowed and forbidden within the shock, while all higher-resolution runs exhibited cellular burning (See Figure 3.6).

In order to interpret these results, first consider the development of the transverse instability that leads to cellular burning. As an initially planar detonation propagates through a fuel source it inevitably encounters inhomogeneities within the fuel. These perturbations can disrupt the detonation front, introducing transverse motions to the fluid in the reactive flow behind the shock front. The magnitudes of these transverse motions grow as they are nurtured by nuclear energy release. Interactions at the detonation front between adjacent volumes of fluid with large, oppositely-oriented transverse velocities can create "hot-spots" of increased density and temperature capable of igniting micro-detonations. These miniature detonations emit spherical shock waves which expand to overtake the main detonation front. These strong, expanding regions of the main front are called Mach stems, each of which is framed by a set of incident shocks. As neighboring Mach stems expand into the common incident shock lying between them, their transverse waves collide, creating a hot-spot which will then expand as a newly created Mach stem. Then, effectively, the segment of the detonation front that was an incident shock has evolved into a Mach stem and the segments of the front that were previously Mach stems are now the weaker incident shocks. The points on the front where a Mach stem, incident shock, and transverse wave coexist are called triple-shock configurations. These triple-points are high-pressure regions that move back and forth across the main front as the dynamic system propagates into the fuel, and it is these points that trace out the characteristic pattern of the cellular burning regime (see Figure 3.7). Burning that occurs under the weaker conditions of the incident shock segments of the detonation front is incomplete relative to the burning that occurs at the Mach stem segments. This creates pockets of under-reacted, low-density material found by previous studies (Gamezo et al., 1999b; Boisseau et al., 1996).

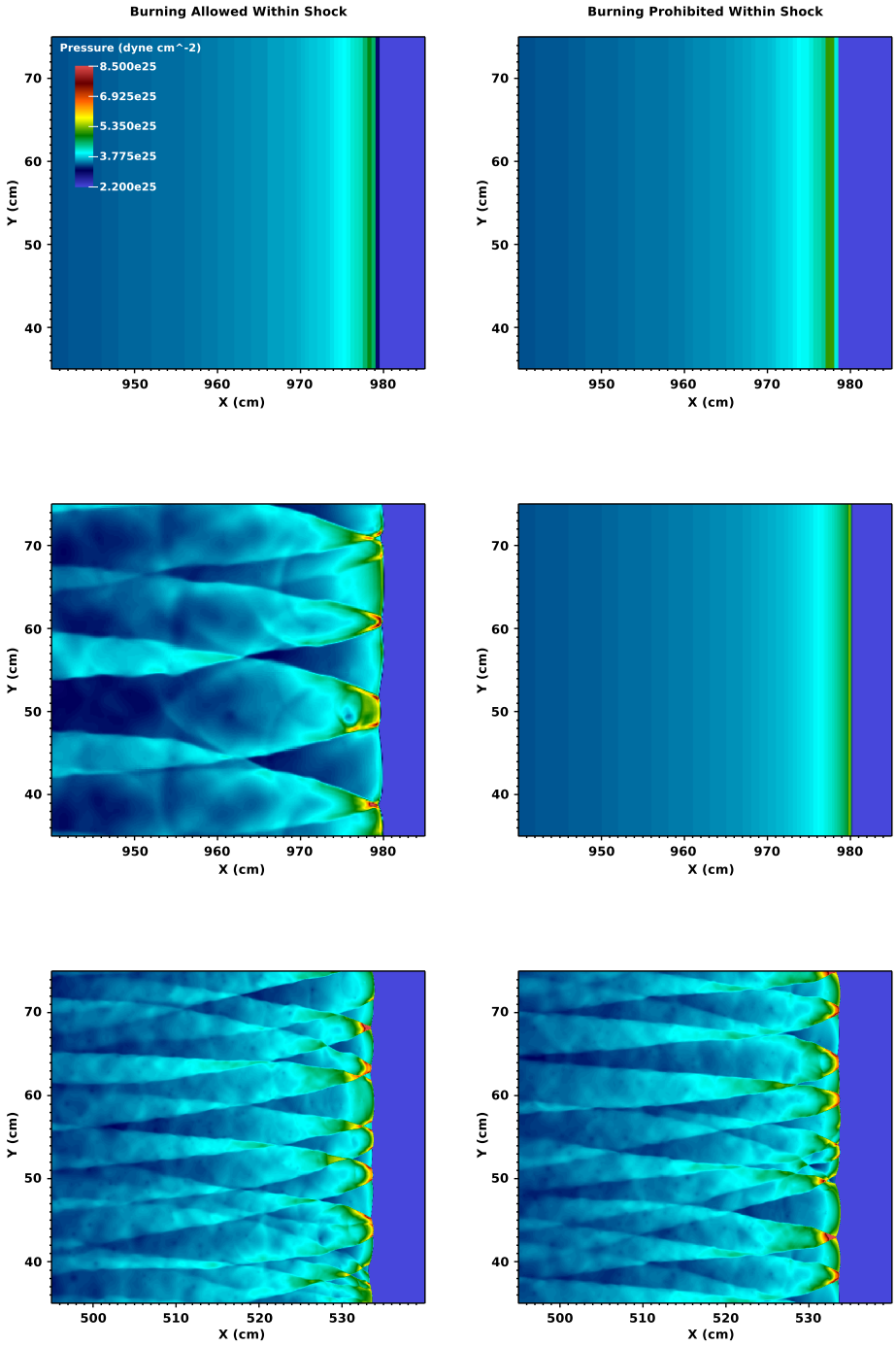


Figure 3.5: Snapshots of pressure from unperturbed, 2D series. The top, middle, and bottom rows show the results from the 0.5-, 0.125-, and 0.03125-cm maximum resolution simulations, respectively. The 0.5- and 0.125-cm panels show the results at t = 8×10^{-7}s and the 0.03125-cm panels show the results at t = 4.15×10^{-7}s. The differences in the fine features of the detonation fronts are due to various onset times for cellular burning.

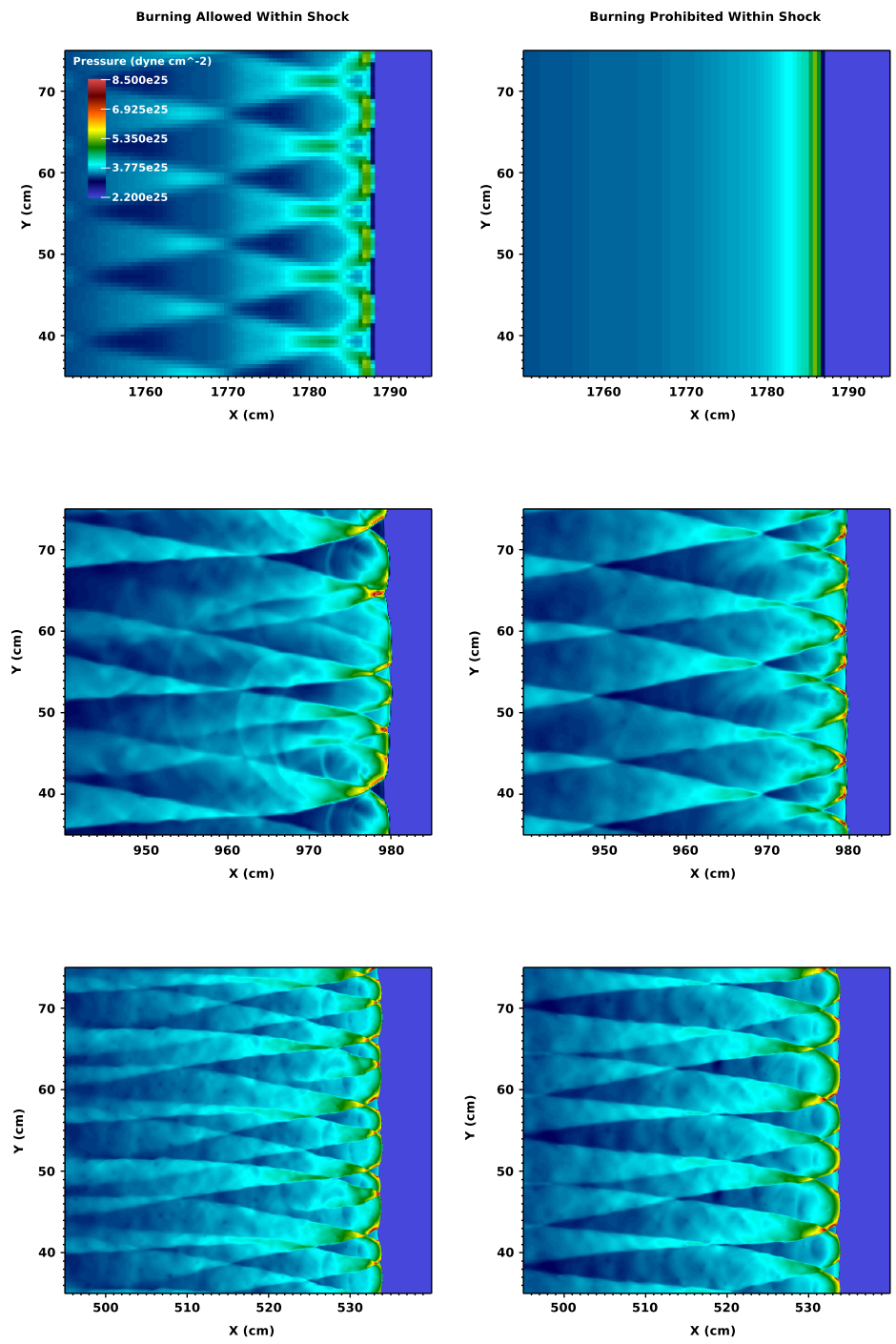


Figure 3.6: Snapshots of pressure from the perturbed, 2D series. The top, middle, and bottom rows show the results from the 0.5-, 0.125-, and 0.03125-cm maximum resolution simulations, respectively. The 0.5-, 0.125-, 0.03125-cm panels show the pressure at t = 1.5×10^{-6}s, t = 8×10^{-7}s, and t = 4.15×10^{-7}s, respectively. The differences in the fine features of the detonation fronts are due to various onset times for cellular burning.

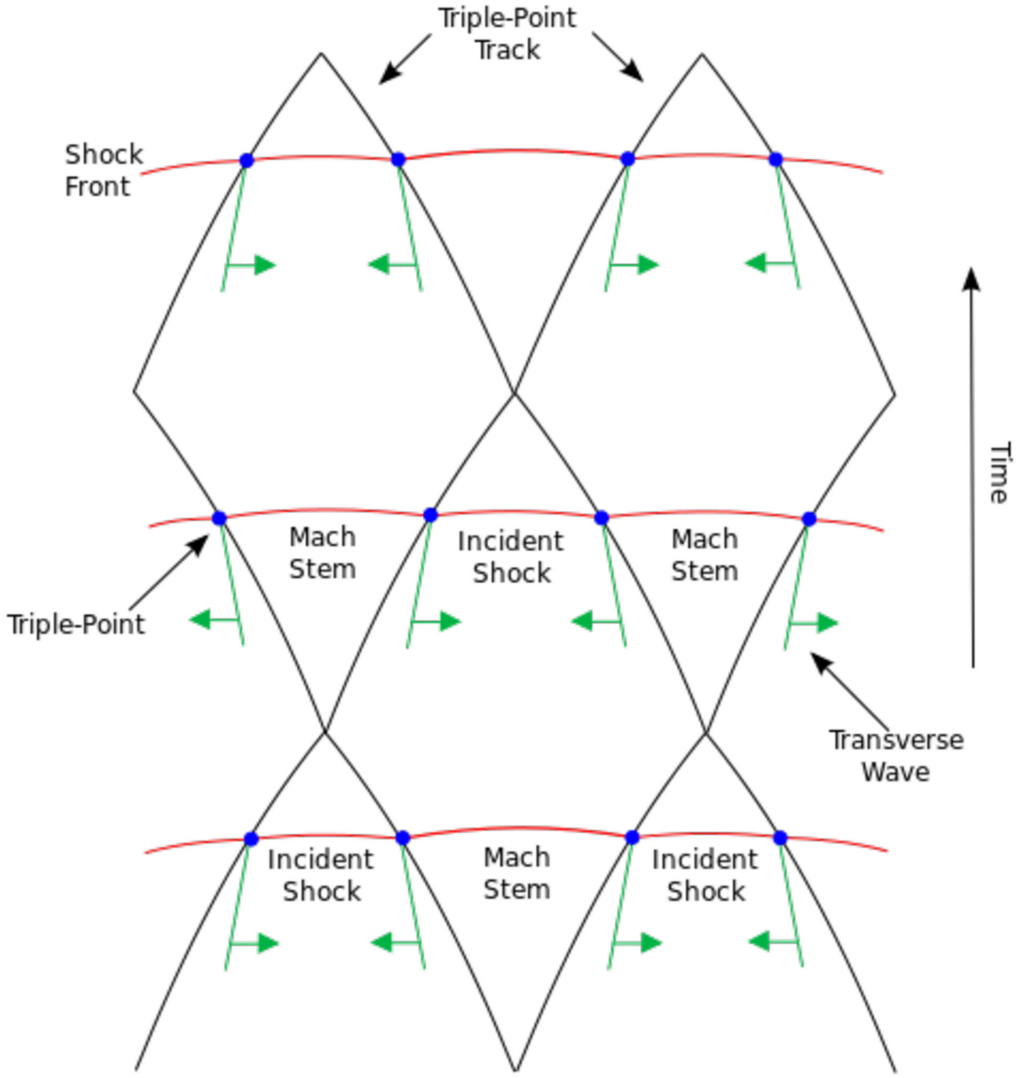


Figure 3.7: Diagram illustrating the formation of cellular structure. The shock front is shown at three times, superimposed on the triple-point paths (Fickett and Davis, 1979; Timmes et al., 2000a). The main features of the detonation front are the Mach stems, incident shocks, and transverse waves. The points where these three features coexist are high-pressure regions called triple-shock structures, or triple-points, which trace out the cellular pattern shown in black.

Next consider a numerical interpretation of this scenario. A detonation is initially ignited with only an x-component of velocity and perturbations are introduced explicitly or through numerical noise on the grid. The perturbations induce the transverse fluid motions described above, however, in this case the shock is artificially stretched and dependent on grid resolution. On a coarse grid, if burning within the shock is prohibited, the burning and subsequent energy release are displaced away from their natural location just behind the detonation front. If the displacement is large enough, the transverse waves cannot interact properly with the detonation front and cellular burning will be inhibited.

Let us return to the recurrent picture of cell formation portrayed in Figure 3.7, considering first the unperturbed series followed by the perturbed. In the unperturbed series, the 0.5-cm resolution simulations do not show cellular structure, regardless of their treatment of burning within the shock. This occurs because the energy release is not sufficiently localized to properly nurture the small transverse motions created by numerical noise. Figure 3.4 shows the maximum rate of nuclear energy generation on the grid versus time, illustrating this inadequacy for the 0.5-cm resolution case. For the 0.125-cm resolution simulation where burning within the shock is allowed, cellular structure does occur. In this case the energy release is sufficient to develop the small transverse velocities to larger magnitudes. However, for the corresponding simulation where burning within the shock is prohibited, we do not see cellular structure. With the previous considerations in mind, we can see that this occurs because the energy deposition is displaced from the detonation front far enough that the resulting transverse components of the fluid fail to effectively interact with the front: The transverse velocities do not escalate and the dynamic triple-shock interactions cannot develop, inhibiting the formation of cellular structure. The 0.125-cm resolution simulations with burning allowed within the shock showed accumulated growth and interaction of the transverse components of the fluid until cellular structure developed. Conversely, for the case where burning within the shock was prevented, large, coherent regions of transverse velocities never developed. At the highest resolution (0.03125-cm), with burning prevented inside the shock, the transverse waves were able to interact with the front because the finer

resolution leads to a numerical shock with smaller physical extent. Therefore, no qualitative differences are seen for the simulations at this resolution regardless of whether burning was allowed or prohibited within the shock.

Explicitly-defined perturbations imparted larger regions of higher-amplitude transverse motions to the fluid than those seeded by numerical noise, producing somewhat different results. Indeed, with explicit perturbations, the 0.5-cm resolution simulation with burning allowed within the shock exhibited cellular structure while its unperturbed counterpart did not. The energy release in the explicitly perturbed case did not need to nurture very small transverse motions to the point where they could effectively interact with the detonation front, as was required in the unperturbed series. Instead, the transverse motions, as created, were large enough that the energy release only needed to maintain the motion. In contrast, the 0.5-cm resolution model with burning prevented within the shock did not exhibit cellular structure in either the perturbed or unperturbed simulations. This is because the energy release was sufficiently displaced from the leading edge of the numerical shock that transverse motions could not be maintained near enough to the detonation front for the triple-point interactions to occur. This is illustrated in Figure 3.8, which shows transverse velocities at the detonation front for the perturbed, 0.5-cm resolution simulations. The left column of panels shows a time sequence of the results when burning is allowed within the shock and the right column shows the same time sequence for the case when burning is prohibited within the shock. In the top panels both cases show structured transverse motions, owing to the perturbed initial conditions (although there is a marked difference in the scale of the magnitudes). However, as we follow the time sequence forward (down the columns), it is clear that when burning is allowed within the shock the transverse motions evolve to a stable structure but when burning is prevented within the shock the structure of the transverse motions decays until it is unrecognizable in the bottom panel. The increased spatial resolution found in the 0.125-cm resolution simulations with burning forbidden within the shock surmount this particular problem and cellular structure is seen in the perturbed series at this resolution, again due to the larger transverse motions imparted on the fluid.

Because the numerical shock had smaller physical extent at the finer resolution, the stronger transverse waves were able to effectively interact with the detonation front from the time they were created. Conversely, the unperturbed simulations at this resolution require some time for the growth of very small transverse velocities before cellular structure can begin to form.

As in Timmes et al. (2000b), we find that the strength of the cellular features are resolution-dependent. Furthermore, we also find that these features are dependent on the treatment of burning within the shock. Figure 3.9 is a plot of maximum density versus time for the unperturbed 0.125- and 0.03125-cm resolution simulations. For most of the evolution (i.e. always after the initial transient period and whenever cellular structure is achieved), these data correspond to the highest-density triple-point at each time step. Before the onset of cellular burning, it is the simulations that prevent burning within the shock which have higher densities, as burning does not occur until post-shock conditions are reached. However, during cellular burning, it is the simulations that allow burning within the shock which exhibit the highest densities. With burning allowed within the shock the triple-points are enhanced by the multi-D dynamic effects of energy release within the leading zones of the main shock front. This "pre-conditions" the fluid before the triple-points are fully formed, increasing the density and temperature within the triple-points. However, the corresponding consumption of fuel within the shock leaves less fuel available to burn in the triple-points. These effects conspire to result in lower values of instantaneous maximum energy release in the triple-points than was the case where burning was prohibited within the shock.

3.3 Summary and Discussion

We find that prohibition of burning within a numerically-widened shock is important when a significant amount of fuel will burn within it, consistent with the results of Fryxell et al. (1989). A sufficiently resolved shock does not require application of this prescription, however its promiscuous use can ensure integrity without demanding a search for adequate refinement

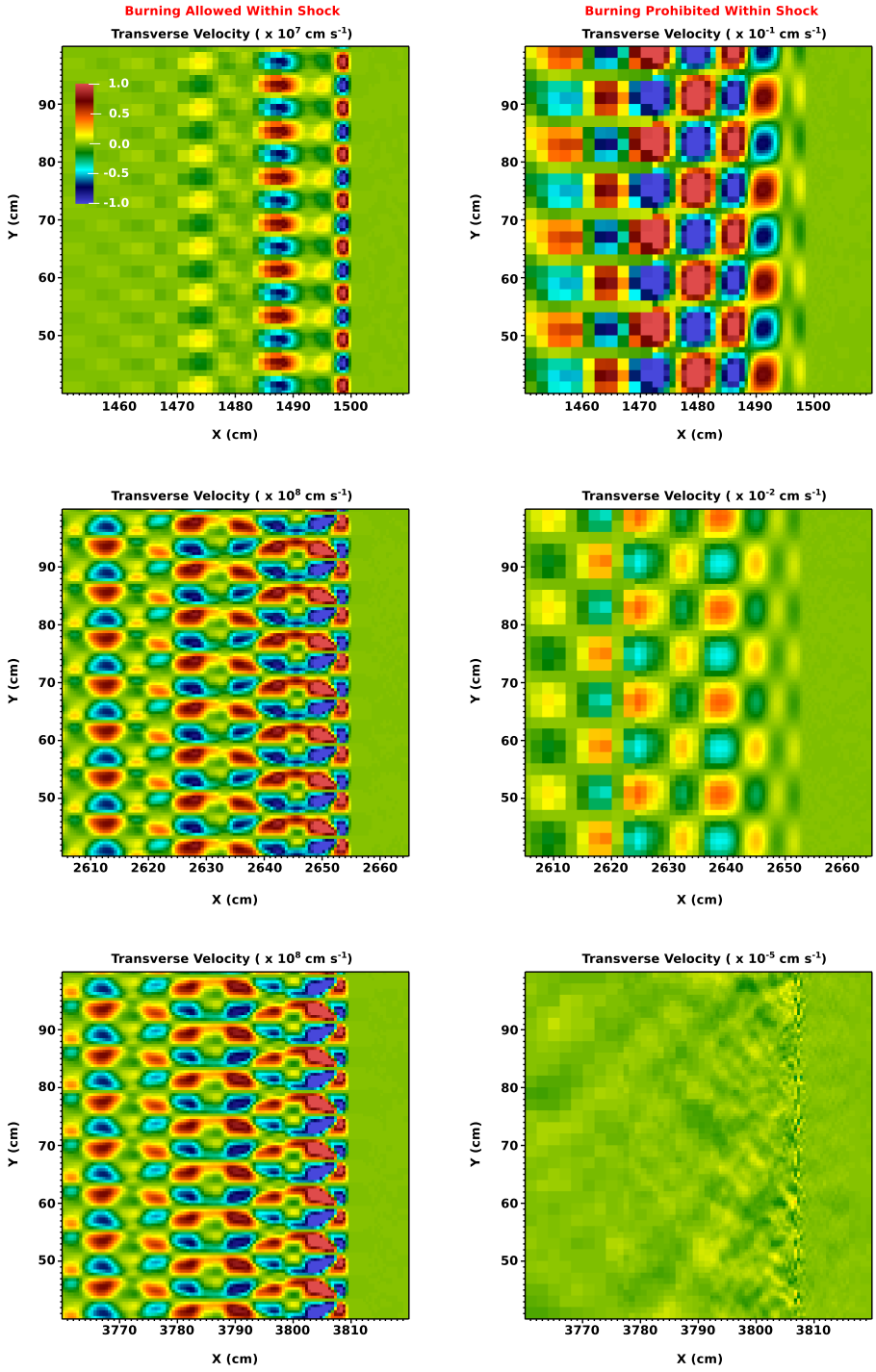


Figure 3.8: Transverse velocity versus position for the perturbed, 0.5-cm resolution model. The left and right panels show the cases where burning is allowed and prohibited within the shock, respectively. The color map can be seen in the top left panel only, while each panel has its own scale. The top, middle, and bottom rows show the results for the two cases at 1.25×10^{-6} s, 2.25×10^{-6} s, and 3.25×10^{-6} s, respectively.

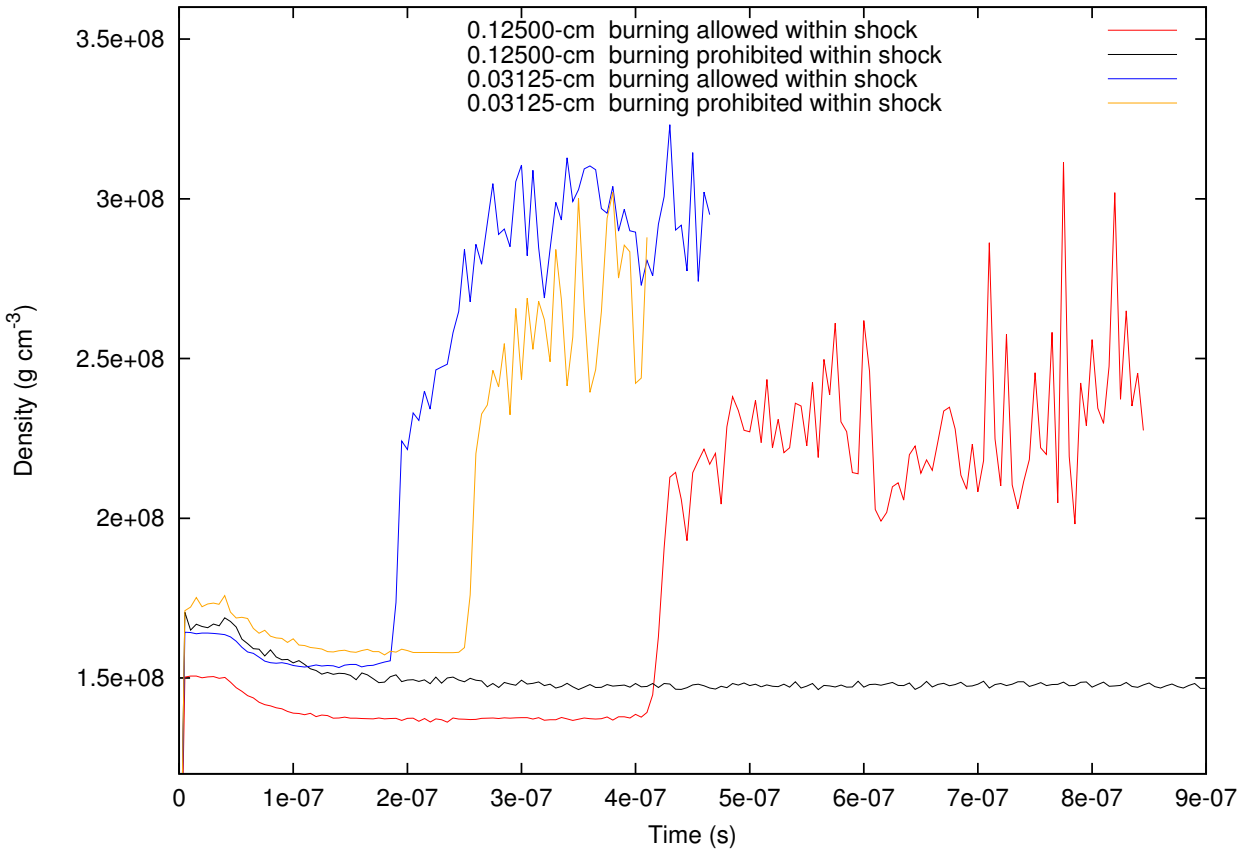


Figure 3.9: Maximum density profiles from the unperturbed, 2D series showing the onset of cellular burning (steep increases in density). The strength of the triple-points corresponding to these maximum values are dependent on resolution as well as the treatment of burning within the numerical shock.

at different fuel densities. Hence the well-known recommendation to prevent burning inside of a simulated shock. In 2D we find that imposing this treatment can unintentionally inhibit the formation of cellular structure by displacing the release of nuclear energy to the region behind a coarsely resolved shock, therefore obstructing the development of transverse perturbations. In addition, we find that the strength of the triple-points, as well as the energy release realized in the triple points, is affected by the treatment of shock burning.

Due to the disparity of length scales involved in simulating SNe Ia, approximate burning models are required to incorporate small-scale flame physics into full-star explosion models, and it is direct numerical simulations (DNS) such as those presented here that are used to inform these models. We assert that our results may influence the fidelity of large-scale SNe Ia simulations through this channel. Previous simulations of multi-D detonation fronts in Type Ia environments (Boisseau et al., 1996; Gamezo et al., 1999b; Timmes et al., 2000b) have shown that pockets of incompletely-burned material, created by the presence of cellular structure, can increase the effective size of burning regions relative to 1D calculations. Because the production of IMEs would be possible at higher densities, Gamezo et al. (1999b) argued that this increases the critical density at which a DDT can occur. Our results suggest this effect can be hidden due to a particular treatment of burning within the numerical shock, either in approximate burning models or *in situ* at very low density. Importantly, these effects are most prominent in sub-Chandrasekhar-mass models due to their larger amounts of material at low densities. Recent simulations (Fink et al., 2010; Sim et al., 2010; van Kerkwijk et al., 2010; Pakmor et al., 2012) have shown that pure detonations of sub-Chandrasekhar-mass WDs commonly result in incomplete burning due to these low densites ($< 10^7$ g cm^{-3}). The elongation of burning lengths due to cellular structure can exacerbate the incompleteness of burning in these cases: At a given time, cellular formation will lead to more partially burned material behind the shock. For unresolved cellular formation, a sub-grid model that does not account for this modification will lead to incorrect energy release and isotopic composition. At lower densities, cellular structure might well be resolved (albeit

coarsely) in large-scale simulations. At these densities, the prohibition of burning within the shock will effectively retard this effect, leading again to incorrect results.

Detailed abundances are required for use in comparison to observations, especially at low densities ($< 10^7$ g cm^{-3}). A sub-grid model will be necessary to account for multi-D, small-scale structure if this comparison is to be of predictive value. Although previously thought to be rare in Type Ia spectra (believed to be mostly related to super-Chandrasekhar-mass events, e.g. Howell et al., 2006), recent observations (Parrent et al., 2011; Silverman and Filippenko, 2012; Zheng et al., 2013) have shown the presence of unburned C (C_{II} λ6580 features) in the early spectra of a significant number ($\sim 30\%$) of all events. It may be that these features are possible in sub-Chandrasekhar-mass *and* near-Chandrasekhar-mass channels as well. Pockets of unburned C formed by cellular burning may remain if nuclear burning is arrested due to expansion in low-density material, essentially "freezing out" C in the outer ejecta. Failure to account for cellular burning would hide the presence of unburned C from this process. In the case of near-Chandrasekhar-mass models, the amount of material at these densities is small, but in sub-Chandrasekhar-mass models there are significant amounts of mass at these densities. The ability to discriminate between the two models depends on a quantatative calculation of the total amount of unburned C. In order to determine if "freezing out" of unburned C pockets actually impacts C abundance predictions from simulations, care must be taken to obviate the effects of burning within the numerical shock.

Chapter 4

1D Simulations

Having established some new results regarding burning prescriptions in both resolved and unresolved C/O detonations, we now examine how resolution and nuclear network size can affect the outcome of simulating such detonations. Specifically, we discuss how these changes can alter the C- and O-burning lengths, detonation velocities, and resulting abundances. As the name of the chapter implies, we confine our attention to 1D detonations here and discuss the multi-D results in the next chapter.

The detonation models in this chapter were simulated using a custom version of the FLASH code, where we added the ability to evolve the nuclear kinetics using XNet (Hix and Thielemann, 1999), a general thermonuclear reaction network (see Appendix 7 for details). With this new capability, we were able to evolve our detonations with a 13-, 14-, 42-, and 150-species reaction network. The 13-species network is the "Aprox13" α-chain that we encountered in Chapter 3. Recall that this network includes (α,γ)-links (and their inverse links) among its 13 isotopes as well as He-burning and heavy-ion reactions between ^{12}C and ^{16}O. At temperatures above 2.5×10^9 K, this network also includes approximate (α,p)(p,γ)-links (and their inverse reactions) between the isotopes ranging from ^{24}Mg-^{56}Ni because these channels are faster than (α,γ) at these temperatures. These reactions are "approximate" in the sense that steady-state proton flows are assumed so that protons and the intermediate isotopes in the (α,p)(p,γ)-links do not need to be explicitly evolved (see Figure 4.1 and

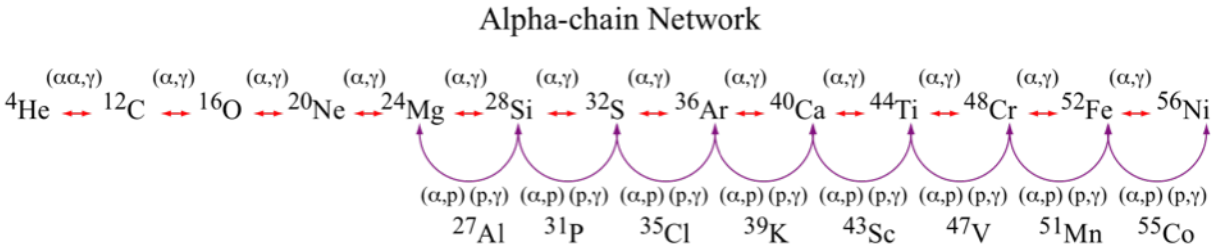


Figure 4.1: Schematic representation of the Aprox13 network showing the approximated (α,p)(p,γ)-links (see Frank Timmes' website – http://cococubed.asu.edu)

Table 4.1). The other three networks are specific implementations of XNet. The 14-species network (X14) is a strict α-chain that tracks the α-isotopes from ^{4}He-^{60}Zn (Table 4.1) and models all reactions that link them, including heavy-ion reactions between ^{12}C, ^{16}O, and ^{20}Ne. Notice though that without including (explicitly or implicitly) protons or the intermediate species such as ^{27}Al, ^{31}P, ^{35}Cl, ^{39}K, ^{43}Sc, ^{47}V, ^{51}Mn, ^{55}Co, this network does not include effective (α,p)(p,γ)-links (or their inverse links), which is the reason it is a "strict" α-chain in contrast to the Aprox13 network. The 42-species network (X14+ap+an) is an extended version of X14 (see Table 4.1) that *does* track the additional isotopes necessary to include not only (α,p)(p,γ)-links (and their inverse links) but also those needed to include (α,n)(n,γ)-links (and their inverse links). The 150-species network (X150) represents our most realistic nuclear kinetics, including the species required to model p- and n-reactions in addition to the reactions modeled by X14+ap+an (see Table 4.1) as well as a much wider range of neutron-rich species, allowing it to follow burning for a much wider range of electron fractions.

Our numerical models consisted of the same sort of 1D "tubes" that we used in Chapter 3. Again, they were filled with a homogeneous 50-50 C/O composition in which detonations were ignited at their left ends. In this study, we explored low fuel densities (ρ_{fuel} = 1×10^{7}, 5×10^{7} g cm^{-3}) that represent conditions in either the pre-expanded, outer regions of near-Chandrasekhar-mass WDs (e.g. single-degenerate scenario) or throughout the entire volume of sub-Chandrasekhar-mass WDs. The spatial extent of these tubes was set at 8192 cm. This extent is small enough to resolve the detonation front but large enough to allow time for the detonations to relax from their initial conditions before the C- and O-burning lengths

Table 4.1: Isotopes tracked in the four nuclear reaction networks.

Network	Participating Isotopes
X14	^{4}He, ^{12}C, ^{16}O, ^{20}Ne, ^{24}Mg, ^{28}Si, ^{32}S, ^{36}Ar, ^{40}Ca, ^{44}Ti, ^{48}Cr, ^{52}Fe, ^{56}Ni, ^{60}Zn
X14+ap+an	n, p, ^{4}He, ^{11}B, $^{11-12}$C, ^{15}N, $^{15-16}$O, ^{19}F, $^{19-20}$Ne, ^{23}Na, $^{23-24}$Mg, ^{27}Al, $^{27-28}$Si, ^{31}P, $^{31-32}$S, ^{35}Cl, $^{35-36}$Ar, ^{39}K, $^{39-40}$Ca, ^{43}Sc, $^{43-44}$Ti, ^{47}V, $^{47-48}$Cr, ^{51}Mn, $^{51-52}$Fe, ^{55}Co, $^{55-56}$Ni, ^{59}Cu, $^{59-60}$Zn
X150	n, p, d, $^{3-4}$He, $^{6-7}$Li, ^{7,9}Be, $^{8,10-11}$B, $^{12-14}$C, $^{13-15}$N, $^{14-18}$O, $^{17-19}$F, $^{18-22}$Ne, $^{21-23}$Na, $^{23-26}$Mg, $^{24-27}$Al, $^{28-32}$Si, $^{29-33}$P, $^{32-36}$S, $^{33-37}$Cl, $^{36-40}$Ar, $^{37-41}$K, $^{40-48}$Ca, $^{43-49}$Sc, $^{44-50}$Ti, $^{46-51}$V, $^{48-54}$Cr, $^{50-55}$Mn, $^{52-58}$Fe, $^{53-59}$Co, $^{56-62}$Ni, $^{57-63}$Cu, $^{59-66}$Zn
Aprox13	^{4}He, ^{12}C, ^{16}O, ^{20}Ne, ^{24}Mg, ^{28}Si, ^{32}S, ^{36}Ar, ^{40}Ca, ^{44}Ti, ^{48}Cr, ^{52}Fe, ^{56}Ni Approximates (α,p)(p,γ)-links (and inverse reactions) through (untracked) intermediate species: p, ^{27}Al, ^{31}P, ^{35}Cl, ^{39}K, ^{43}Sc, ^{47}V, ^{51}Mn, ^{55}Co

were calculated. These burning lengths were measured from the back of the numerical shock to a distance where the initial C or O mass fractions were reduced by either 50% or 90%, defining the 50% and 90% C- and O-burning lengths (see Figure 4.2). At the low densities that we considered, we could not resolve both the fine features of the C and O burning and the large extent of the Si burning on the same grid, so the Si-burning lengths were not measured here. The velocities of our detonations were calculated by tracking the peak value of pressure as it travels across the grid. These detonations were evolved with either the Aprox13, X14, X14+ap+an, or X150 reaction networks and each was performed at 6, 8, 10, 12, and 14 levels of maximum grid refinement (corresponding to 0.5, 0.125, 0.03125, 0.0078125, and 0.001953125 cm resolution)[1]. Based on the results of Chapter 3, we chose to suppress burning within numerical shocks because C-burning is not resolved in all of our models.

4.1 Case 1: $\rho_{fuel} = 1{\times}10^7$ g cm^{-3}

We will begin by examining the results of detonations simulated with the lowest fuel density of $1{\times}10^7$ g cm^{-3}. The temperature of the fuel was set at $1{\times}10^7$ K and was initially at rest. As mentioned above, at this low fuel density, the full reaction zone is much larger than our computational domain. Also, recall that detonations in C/O fuel with densities less than $2{\times}10^7$ g cm^{-3} propagate in the CJ regime (Chapter 2). This means that the sonic point is located at the end of the reaction zone, so all of the energy that is released can be used to drive the detonation. Therefore, because we are not capturing the full reaction zone (and full energy release) on our grid, we must support our detonations from behind in order to ensure their survival. To do so, we ignited our detonations with a hotspot that was 250 cm wide with elevated temperature, density and x-velocity of $4.5{\times}10^9$ K, $4.25{\times}10^7$ g cm^{-3}, and $3.5{\times}10^8$ cm s^{-1}, and used outflow boundary conditions at both ends of the domain. Because of FLASH's implementation of ghost zone updates, these outflow boundary conditions allow

[1]When we refer to the resolution of a particular simulation we will quote its maximum resolution or highest level of grid refinement; this can be confusing due to the adaptive-mesh grid.

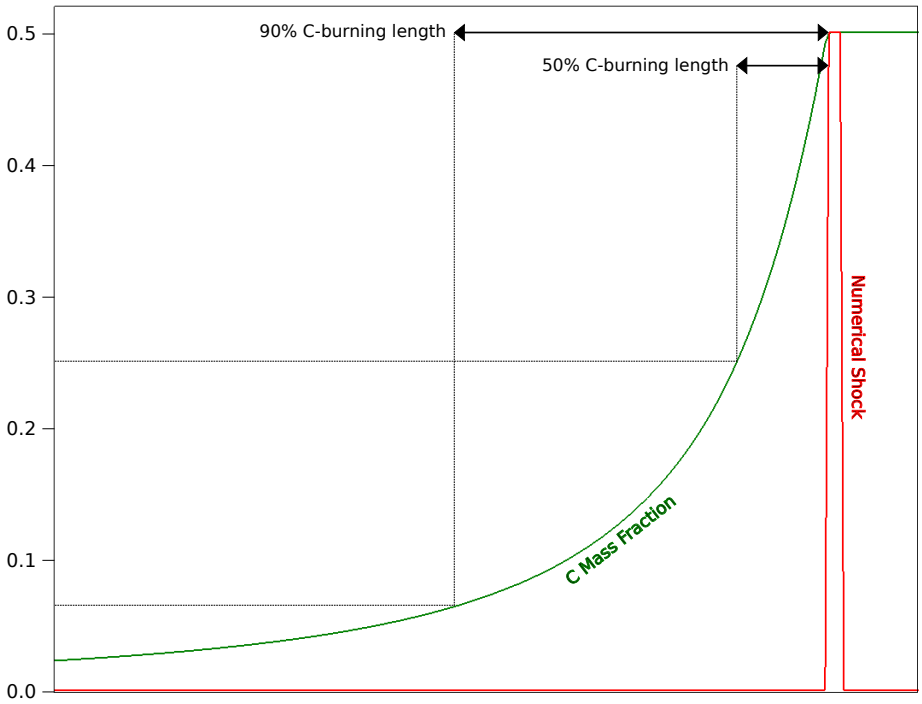


Figure 4.2: The 50% and 90% burning lengths were measured from the back of the numerical shock to a distance where the initial mass fraction of the fuel was reduced by 50% or 90%, respectively.

fluid velocities to let matter flow into the grid (at the left boundary where the detonation is ignited), which effectively creates a piston that travels (from left to right) down the tube at a velocity related to the initial fluid velocity of the hotspot. This piston supplies the necessary support to the back of our detonations by keeping the thermodynamic conditions of the fluid greater than or equal to the values of a self-sustained detonation at a given distance behind the shock. This becomes apparent when we attempt to use reflecting boundary conditions at the left end of the tube instead of outflow. In this case a rarefaction forms near the reflecting wall which deteriorates the rear support and causes the detonation to fail. In addition to ensuring survival of our detonations, the piston also causes them to be slightly overdriven. This overdrive can cause the burning lengths to be slightly decreased relative to the self-sustained case. Here, however, we are concerned with differences between simulations evolved with different reaction networks and different resolutions.

Figures 4.3 and 4.4 show how the 50% and 90% C-burning lengths differ at this density when using each of the four reaction networks and also how they depend on grid resolution. The differences in these burning lengths are due to the C-burning reactions that are available to each network. The main reaction that dominates C-burning under these conditions is

$$^{12}\mathrm{C} + {}^{12}\mathrm{C} \longrightarrow {}^{24}\mathrm{Mg}^{*}, \tag{4.1}$$

where $^{24}\mathrm{Mg}^{*}$ is an excited nucleus that can decay by many processes. The most important of these processes are

$$^{12}\mathrm{C} + {}^{12}\mathrm{C} \longrightarrow {}^{24}\mathrm{Mg}^{*} \longrightarrow {}^{20}\mathrm{Ne} + {}^{4}\mathrm{He} \tag{4.2}$$

$$\longrightarrow {}^{23}\mathrm{Na} + \mathrm{p}. \tag{4.3}$$

All three XNet networks include the $^{12}\mathrm{C} + {}^{12}\mathrm{C} \longrightarrow {}^{20}\mathrm{Ne} + {}^{4}\mathrm{He}$ reaction branches because the isotopes involved in this reaction are tracked in all three networks. However, X14 does not track protons or non-α isotopes such as $^{23}\mathrm{Na}$, so it does not include the reaction $^{12}\mathrm{C} + {}^{12}\mathrm{C} \longrightarrow {}^{23}\mathrm{Na} + \mathrm{p}$. Therefore, because X14 fails to model a reaction that accounts for

almost half of the C-burning, the corresponding burning length is about 2× longer than the other networks that model both reactions. The Aprox13 network does not include protons or the isotope ^{23}Na either, but it still gives a similar C-burning length compared to the networks that do track these species because it uses the reaction rate for the $^{12}C + {}^{12}C \longrightarrow {}^{24}Mg^*$ trunk as the reaction rate for $^{12}C + {}^{12}C \longrightarrow {}^{20}Ne + {}^{4}He$, whereas XNet uses the rates of $^{12}C + {}^{12}C \longrightarrow {}^{20}Ne + {}^{4}He$ and $^{12}C + {}^{12}C \longrightarrow {}^{23}Na + p$ branches individually (assuming the participating isotopes are included in the specific network). Aprox13 simply assumes that the only decay channel resulting from the excited $^{24}Mg^*$ nucleus is Equation 4.2. Continuing with this same line of reasoning, the X150 network models p- and n-reactions such as $^{12}C(p,\gamma)^{13}N$ and $^{12}C(n,\gamma)^{13}C$ (that are not available in the other networks) because it tracks the participating species ^{13}N and ^{13}C. However, because the heavy-ion reactions dominate the C-burning processes (due to very small n and p abundances during the initial burning), these n- and p-reactions do not have a large effect on the C-burning length. But, by the end of the C-burning region, these reactions do lead to a slightly shorter C-burning length for X150 relative to the X14+ap+an network as can be seen in the 90% C-burning lengths of Figure 4.4. The Aprox13 network does not include these n- and p-reactions either but it still gives similar results for the C-burning lengths as the X150 network because the reaction rates in Aprox13 have been hand-tuned to give results similar to larger networks. Figures 4.3 and 4.4 also show the dependence of the C-burning lengths on grid resolution. The 50% C-burning length are smaller than our coarsest zones[2] as measured by all four networks, so as resolution is improved, the burning lengths become resolved and converge toward their correct values for each network (Figure 4.3). The 90% C-burning lengths are larger than our coarsest zones as measured by all networks (Figure 4.4), so although there is still a slight dependence on resolution, it is less obvious than for the 50% C-burning lengths.

Figures 4.5 and 4.6 show the 50% and 90% O-burning lengths for the different reaction networks. Similar to C-burning, the reactions involving two ^{16}O nuclei create an excited

[2]By coarsest zones we mean the finest resolution at 6 levels of maximum grid refinement; 0.5 cm

state of $^{32}S^*$ which decays by many processes. The most likely of these decays are

$$^{16}O + {}^{16}O \longrightarrow {}^{32}S^* \longrightarrow {}^{28}Si + {}^{4}He \tag{4.4}$$

$$\longrightarrow {}^{31}P + p. \tag{4.5}$$

Because X14 does not include protons or the isotope ^{31}P, it does a poor job of tracking the O-burning lengths, similar to the C-burning case. Aprox13 does not explicitly track these species either but does account for the proper reduction in O (due to $^{16}O + {}^{16}O$ reactions) by employing the reaction rate of the $^{16}O + {}^{16}O \longrightarrow {}^{32}S^*$ trunk as the rate for $^{16}O + {}^{16}O \longrightarrow {}^{28}Si + {}^{4}He$ instead of the reaction rates of the individual branches of Equations 4.4 and 4.5 as is done in XNet. In addition, the heavy-ion reactions

$$^{12}C + {}^{16}O \longrightarrow {}^{27}Al + p \tag{4.6}$$

$$^{12}C + {}^{16}O \longrightarrow {}^{24}Mg + {}^{4}He. \tag{4.7}$$

also take part in diminishing the O abundance. In fact, the rates of these reactions are high enough, and there is enough ^{12}C still present, that these reactions are comparable with the $^{16}O + {}^{16}O$ reactions of Equations 4.4 and 4.5. However, at these high temperatures ($T_9 = 5.5$), and among the ashes of the previous C-burning phase (i.e. larger amounts of p and n present), it is the p- and n-reactions

$$p + {}^{16}O \longrightarrow {}^{13}N + {}^{4}He \tag{4.8}$$

$$n + {}^{16}O \longrightarrow {}^{13}C + {}^{4}He. \tag{4.9}$$

that dominate O-burning. Therefore, because none of the other networks track the isotopes ^{13}N and ^{13}C, the X150 network has a significantly shorter O-burning length as can be seen in Figures 4.5 and 4.6. This behavior can also be seen in Figure 4.7, which shows the ^{12}C, ^{16}O, and ^{28}Si mass fractions resulting from detonations evolved with the four reaction networks at the highest resolution (0.001953125 cm). The profiles of these mass fractions are shown

over the same 1000-cm region near the right end of the domain. The time at which these profiles were captured is the same time (t=6×10^{-6} s) that the C- and O-burning lengths were calculated. The main decline of C is not visible at this length scale, but there is a noticeable region of C just behind the shock for the X150 network. The differences in the O-burning lengths that we saw in Figures 4.5 and 4.6 are visibly apparent here in the mass fraction plots. In addition, the rise of Si can be seen. The X150 results show the peak of Si as well as the start of its decline on this relatively small region, suggesting that the Si-burning lengths might also be reduced by using a larger network. Neither the 50% or 90% O-burning lengths are dependent on grid resolution because they have large physical extents relative to the resolutions that we considered (Figure 4.5 and 4.6).

The detonation velocity found by Gamezo et al. (1999b) in a previous study of C/O detonations with a fuel density of 1×10^7 g cm^{-3} was 1.22×10^9 cm s^{-1}. Table 4.2 shows the values of detonation velocities, and their corresponding overdrive parameters ($f = (\frac{D}{D_{CJ}})^2$), that we obtained from our direct numerical simulations using the four different networks at this density (these measurements were taken from the highest-resolution runs). Using these different networks affects not only the reactions and energy release as the detonation propagates across the domain, but also slightly alters the piston velocities (because of the ignition of fuel with different networks), both of which conspire to give the slight variation seen in the detonation velocities. It is difficult to disentangle these effects, but the variation between networks is only ~2%. Figure 4.8 shows these detonation velocities versus time for the four networks, illustrating their evolution as they relax from the ignition at the left end of the tube[3]. Figure 4.9 shows the total energy generation rate versus time for these same detonations. The different peaks in each of the plots are caused by igniting the hotspots, and continuing to burn the resulting matter, with different reaction networks. This behavior corresponds to the different rise times of the detonation velocities in Figure 4.8. Figure 4.10 compares the detonation velocities for the Aprox13 network calculated at all

[3]Note that the velocities are set to zero until the pressure peak reaches ≥1000 cm in the tube. This is done because the rear support at the left boundary can exceed the pressure peak at the start of a simulation, which can impair our ability to track the peak.

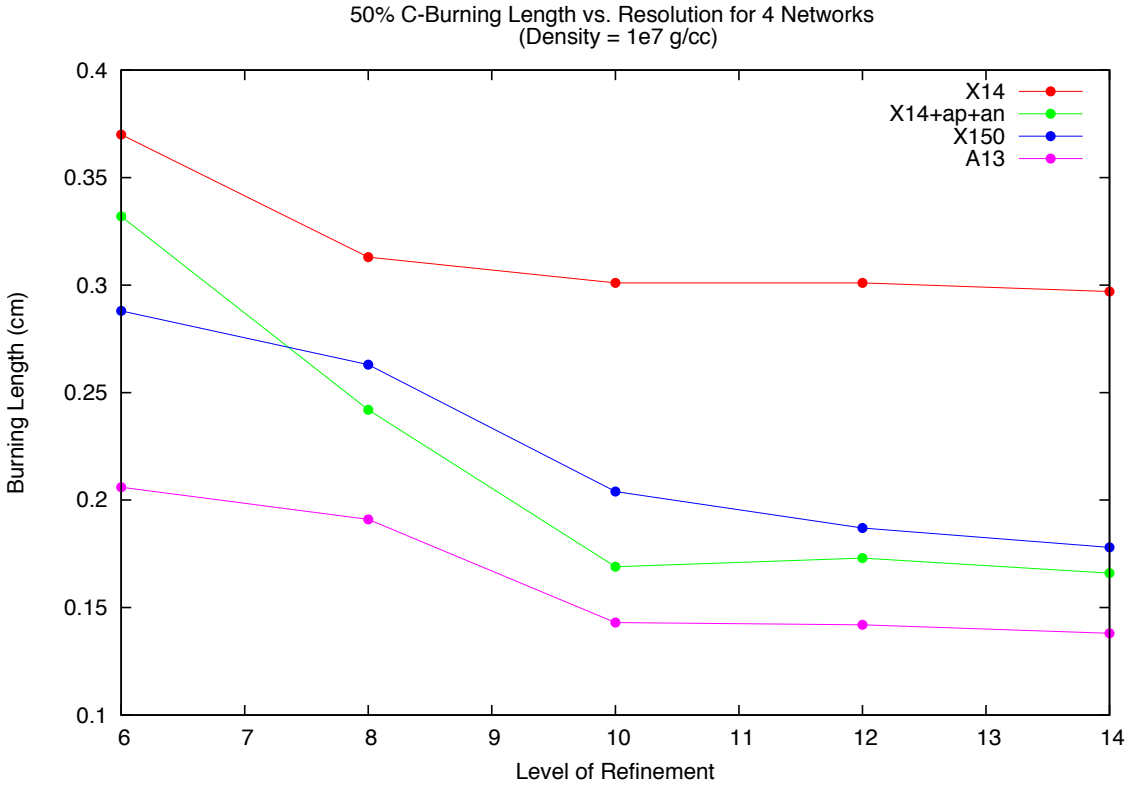


Figure 4.3: 50% C-burning length versus level of grid refinement for four reaction networks in Table 4.1. Level 6, 8, 10, 12, and 14 correspond to 0.5, 0.125, 0.03125, 0.0078125, and 0.001953125 cm resolution.

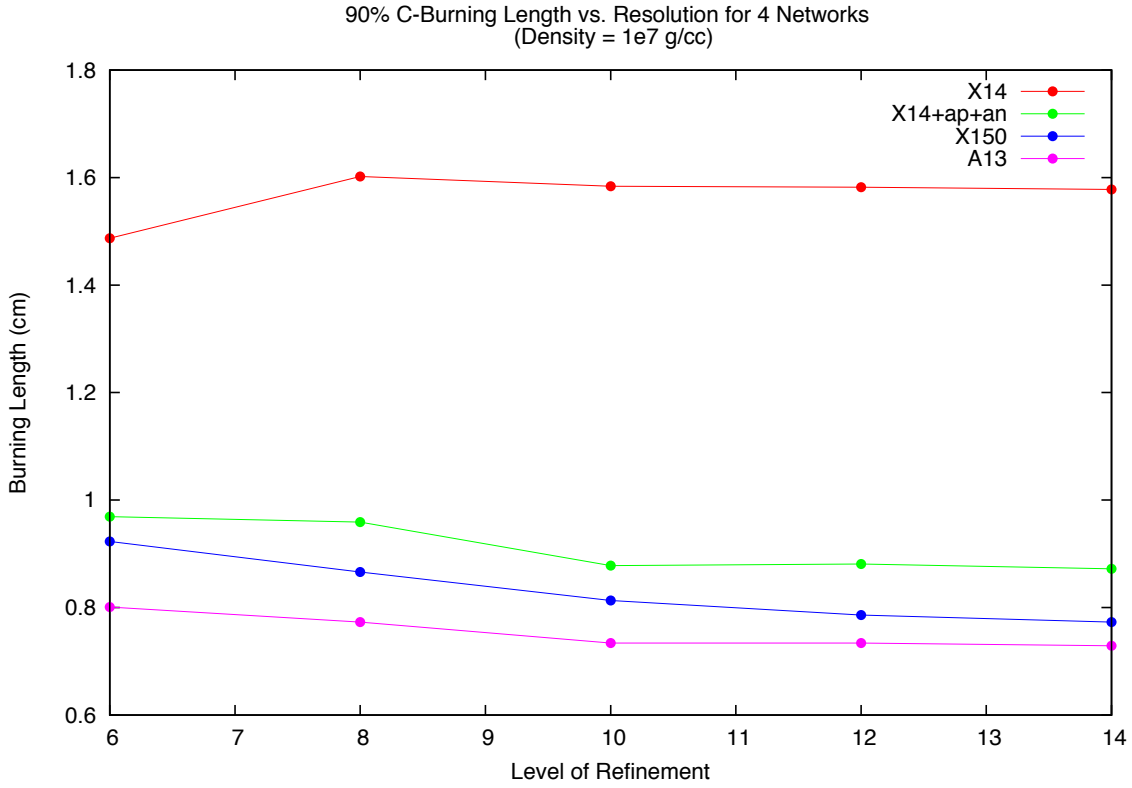


Figure 4.4: 90% C-burning length versus level of grid refinement for four reaction networks in Table 4.1. Level 6, 8, 10, 12, and 14 correspond to 0.5, 0.125, 0.03125, 0.0078125, and 0.001953125 cm resolution.

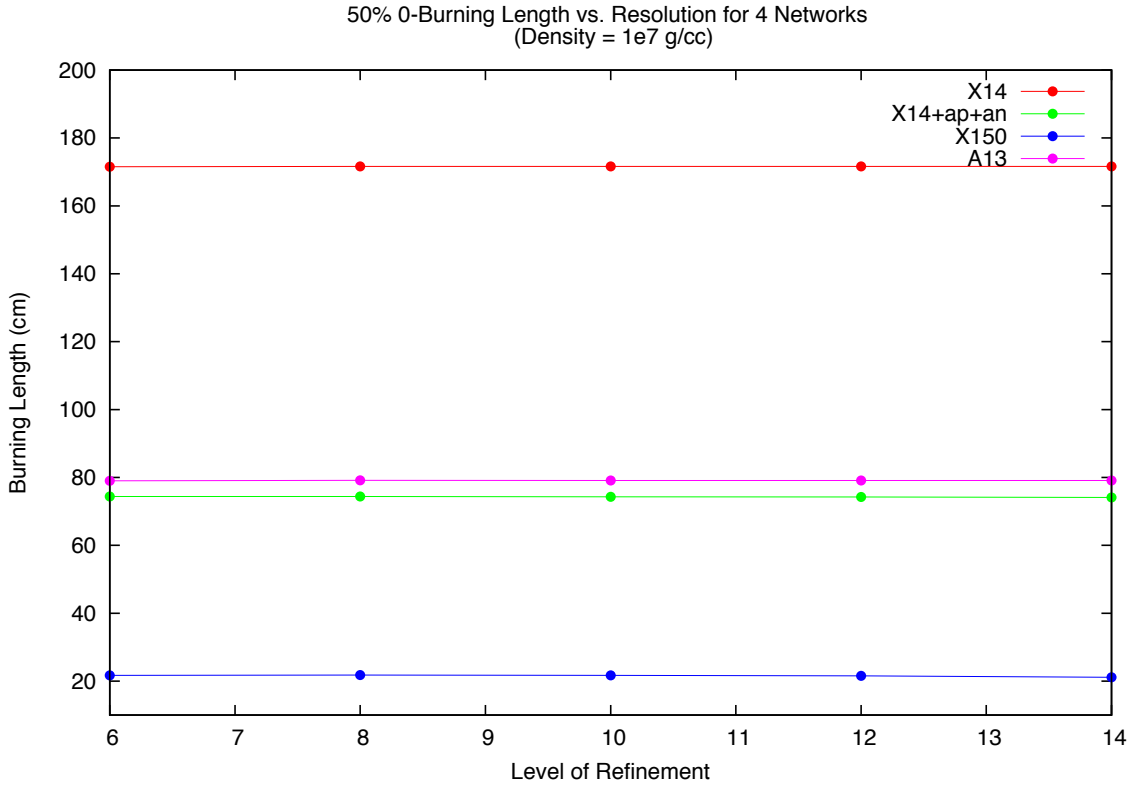


Figure 4.5: 50% O-burning length versus level of grid refinement for four reaction networks in Table 4.1. Level 6, 8, 10, 12, and 14 correspond to 0.5, 0.125, 0.03125, 0.0078125, and 0.001953125 cm resolution.

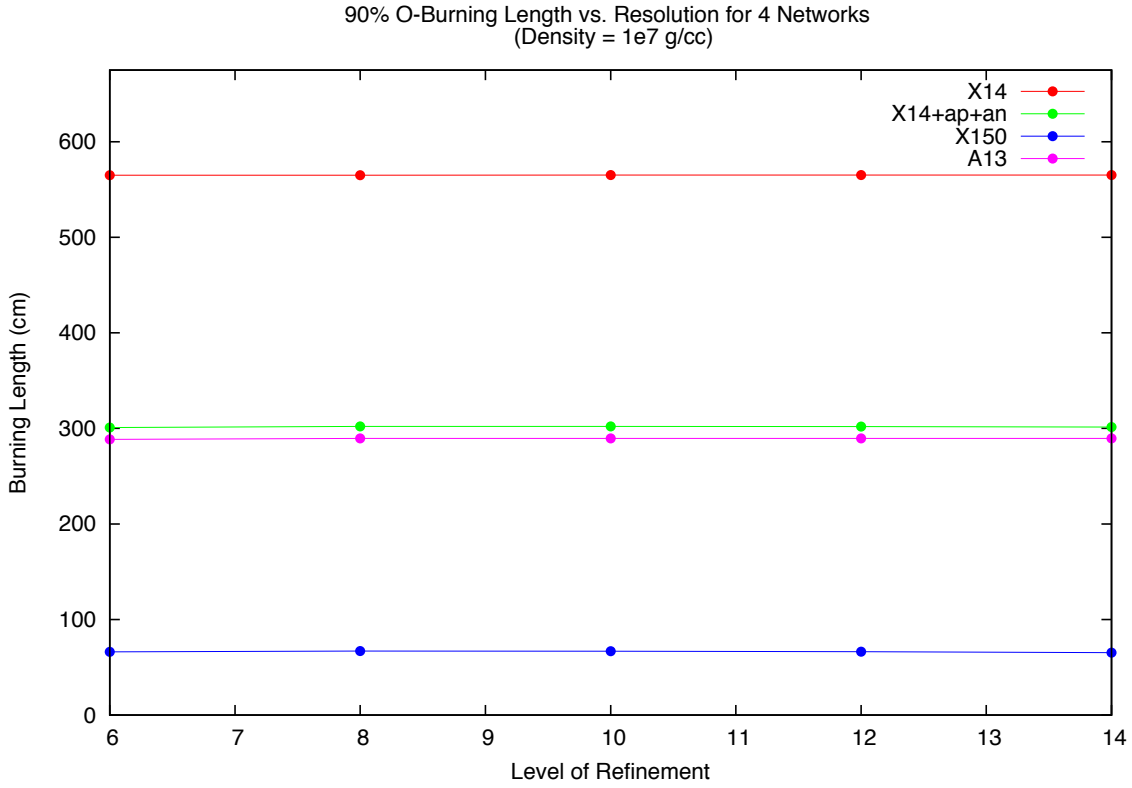


Figure 4.6: 90% O-burning length versus level of grid refinement for four reaction networks in Table 4.1. Level 6, 8, 10, 12, and 14 correspond to 0.5, 0.125, 0.03125, 0.0078125, and 0.001953125 cm resolution.

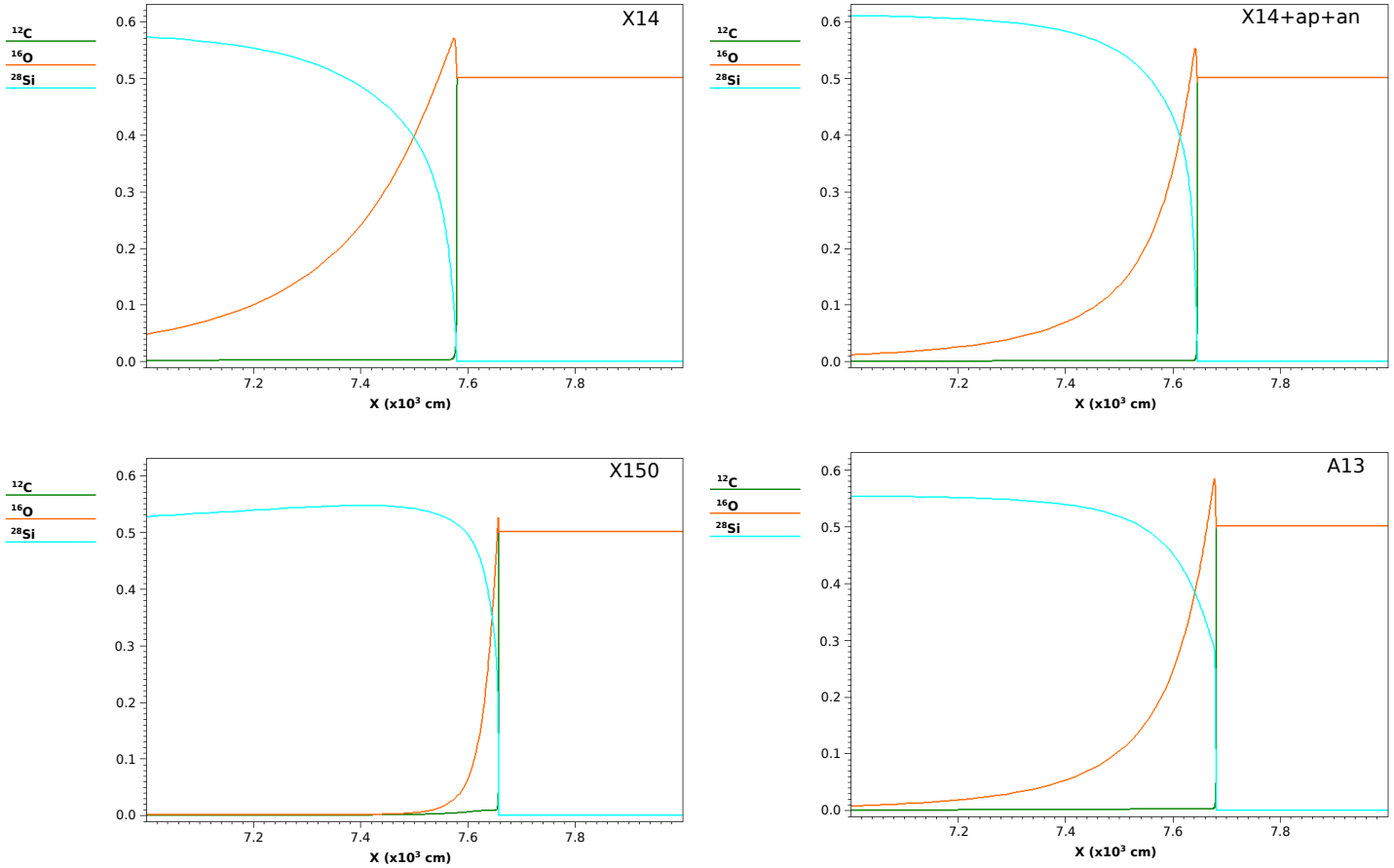


Figure 4.7: ^{12}C, ^{16}O, ^{28}Si mass fractions resulting from detonations with fuel density of 1×10^7 g cm^{-3} (t=6×10^{-6} s).

five grid resolutions, demonstrating that these velocities appear to have no dependence on the resolutions that we considered. This is due to the fact that the total amount of energy that is generated by a given network is the same at all resolutions, even if its distribution is different. Because the entire reaction zone is in sonic contact with the front, the same amount of energy is available to drive the detonations. This seems to be supported by the results in Figure 4.11, which shows the total energy generation rate versus simulation time for the same detonations shown in Figure 4.10. This behavior was verified for all four networks, but only the Aprox13 results are shown here.

4.2 Case 2: $\rho_{fuel} = 5{\times}10^7$ g cm^{-3}

Next, we will examine the results of the detonations with the higher fuel density of $5{\times}10^7$ g cm^{-3}. As before, the temperature of the fuel was set to $1{\times}10^7$ K and was initially at rest. The hotspot used to ignite these detonations was 250 cm wide and had an elevated temperature, density, and x-velocity of $4.25{\times}10^9$ K, $1{\times}10^8$ g cm^{-3}, and $5{\times}10^8$ cm s^{-1}. Again, we used outflow boundary conditions at both ends of the tube which supported our detonations from behind. Although the reaction zone is smaller due to having faster reaction rates at higher densities, it is still too large to fit onto our domain. It should be noted, that here we do not necessarily need the support created by the outflow boundary conditions behind the detonation. The reason for this is that above $2{\times}10^7$ g cm^{-3} C/O detonations become pathological due to endothermic Si-reactions (Chapter 2), so the sonic point moves from the end of the reaction zone (toward the shock) to a position near the end of O-burning. Therefore, even if we did not support our detonations they would propagate in a self-sustained mode because, although the entire reaction zone is not contained on our grid, the part of it that is in sonic contact with the front is included. This was verified by running a simulation where reflecting boundary conditions were used and the detonations propagated without support. However, we decided to still use outflow boundary conditions in order to keep similar initial conditions as were used in the lower-density simulations.

Table 4.2: Detonation velocities and overdrive parameters calculated for the four reaction networks at a fuel density of $1{\times}10^7$ g cm^{-3} (refinement level 14: 0.001953125 cm).

Network	D ($\times 10^9$ cm s^{-1})	$f = (\frac{D}{D_{CJ}})^2$
A13	1.2525	1.0540
X14	1.2509	1.0513
X14+ap+an	1.2457	1.0426
X150	1.2369	1.0279

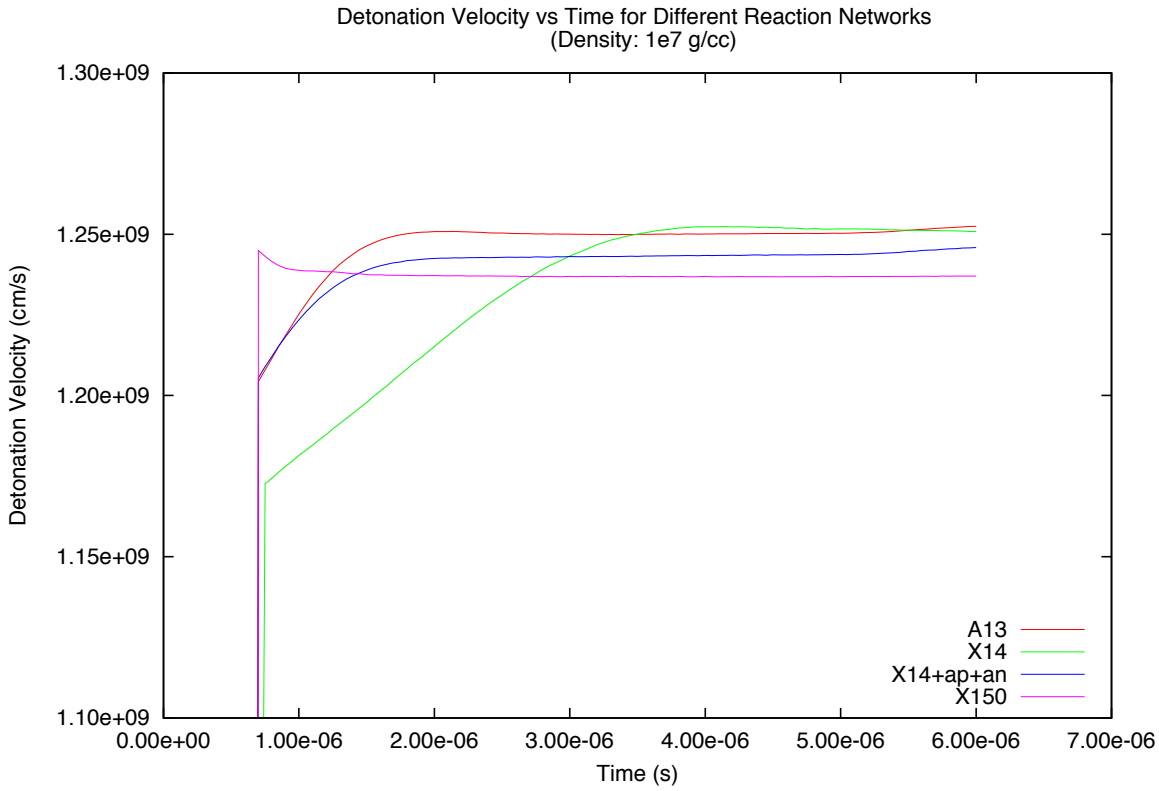


Figure 4.8: Detonation velocity vs time for the four nuclear reaction networks at the highest grid resolution.

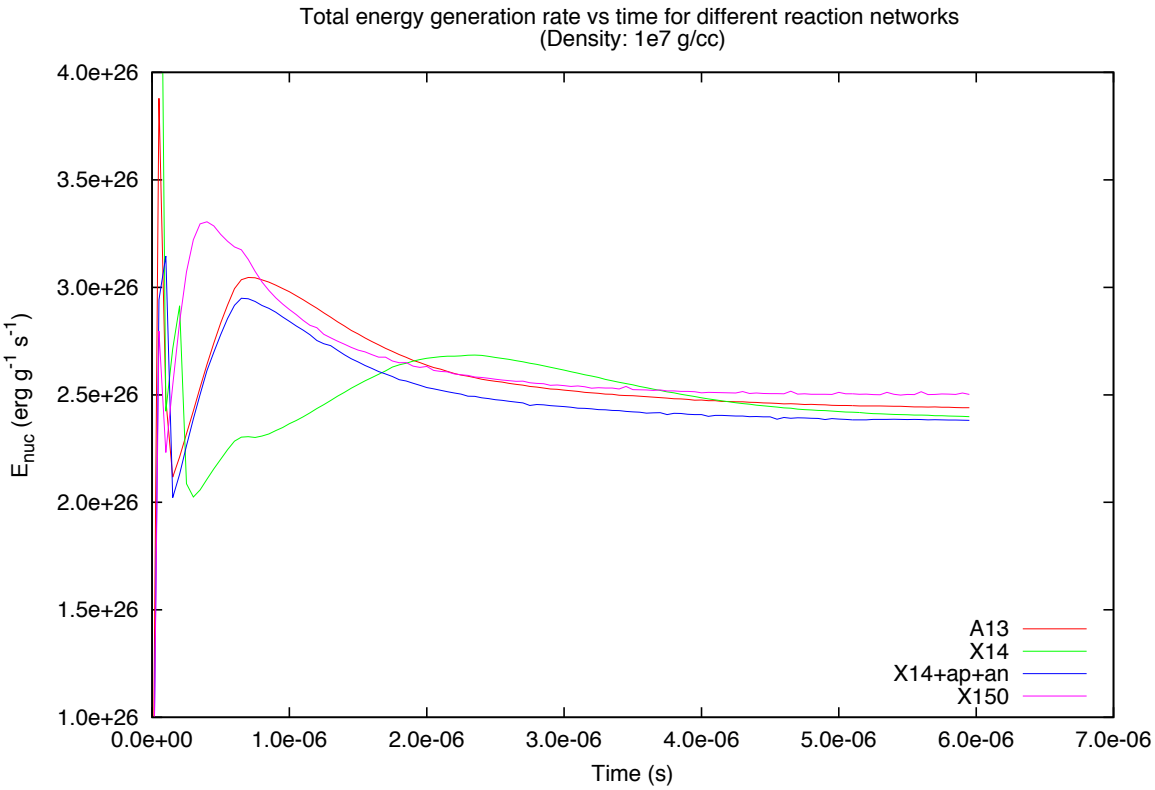


Figure 4.9: Total energy generation rate vs time for the four nuclear reaction networks at the highest grid resolution.

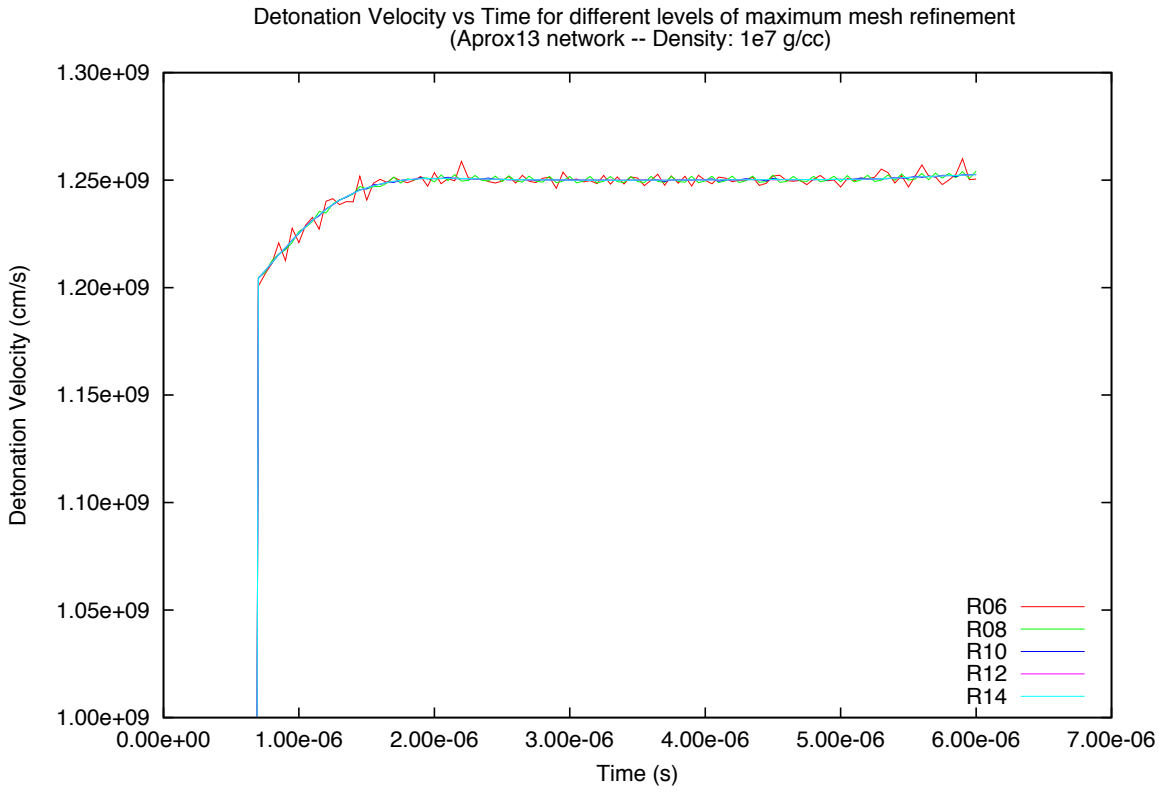


Figure 4.10: detonation velocity vs time for the Aprox13 network at different resolution.

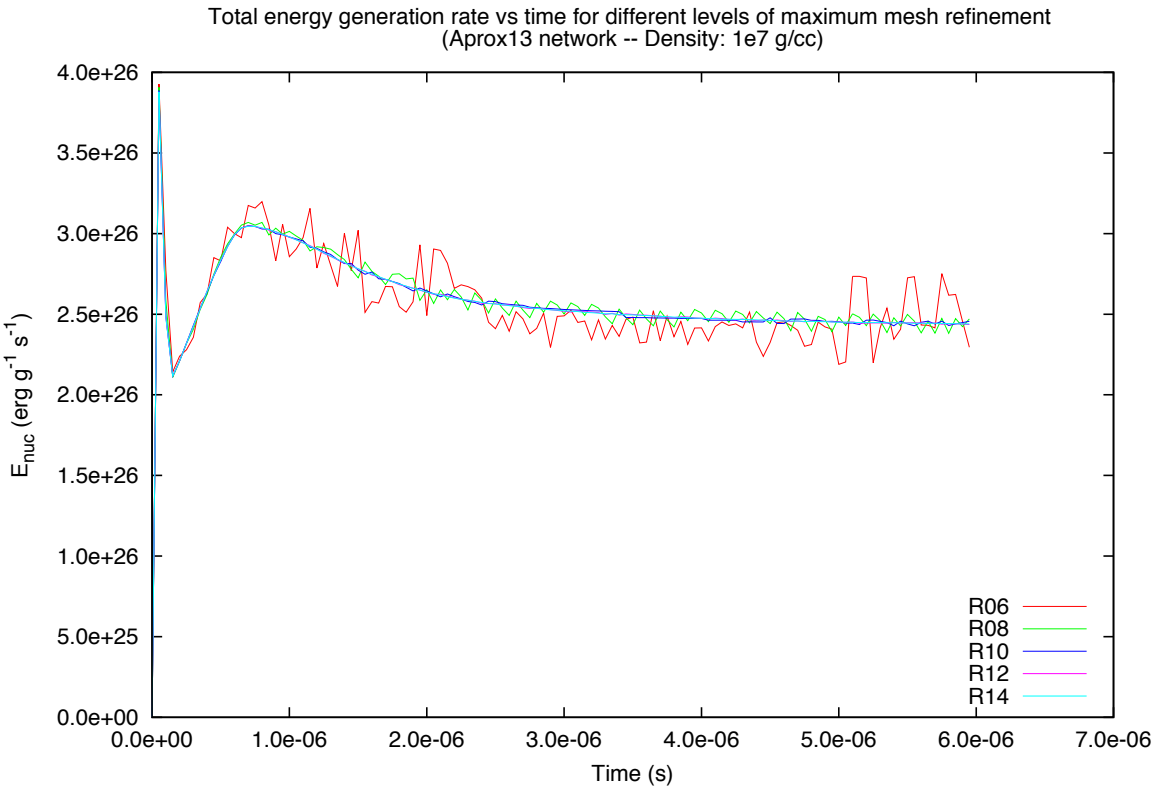


Figure 4.11: Total energy generation rate vs time for the Aprox13 network at different resolution.

An important point to highlight before discussing the results at this higher density is a longitudinal instability that is known to cause oscillations in 1D C/O detonations above 2×10^7 g cm^{-3} (Khokhlov, 1993). When simulating such detonations (where the burning lengths are short compared with the induction lengths), small longitudinal fluid perturbations can grow due to feedback between nuclear energy release and hydrodynamics. This can lead to oscillations in the thermodynamic profiles and resulting abundances and is a physical phenomenon that can be demonstrated in terrestrial detonation experiments (Fickett and Davis, 1979). Although we did not explicitly add such perturbations to our models, the detonations evolved using the 150-species network exhibited oscillations due to this instability (seeded from numerical noise on the grid) for resolutions at or below 0.03125 cm. For these simulations, we were unable to make meaningful measurements of the C- or O-burning lengths because the oscillations led to intermittent quenching and reignition of the detonations. Figure 4.12 shows the oscillations in the pressure profile for a detonation evolved with the X150 network at 10 levels of grid refinement (0.03125 cm resolution). The feedback between energy release and hydrodynamics manifests as a C-pocket that builds up and then explodes just behind the main detonation front (Figures 4.13-4.18). In Figure 4.13, the back of the numerical shock (black dotted curve) is located at about 593.5 cm. The C-pocket can be seen as the abnormally-wide decrease in ^{12}C (green line) that has built up behind the shock. The temperature (magenta line) rises from its initial condition due to shock compression and then rises again as the ^{12}C is burned behind the shock. In Figure 4.14, the C-pocket has ignited explosively, causing the pressure peak to jump and the temperature behind the shock to rise faster. In Figure 4.15, the C-pocket is almost completely burned (notice its decreased extent behind the shock relative to Figures 4.13 and 4.14). Now a peak in temperature is apparent as well as the fact that the ^{16}O behind the shock has also been ignited by the C-explosion. Figure 4.16 shows the decreasing pressure peak as the C- and O-pockets begin to build back up. Figure 4.17 shows both the C- and O-pockets continuing to grow as the pressure and temperature return to their lower values. In Figure 4.18, the isotopic and thermodynamic profiles have returned to their initial states before the C-explosion (ready to begin the next cycle), but the effects of the explosion cycle

can still be seen in their extended profiles. This lingering effect is more obvious if we show a larger region behind the shock as is illustrated in Figure 4.19. Khokhlov (1993) showed this same phenomena led to the oscillations in his study, but did not mention the burning of the O-pocket in addition to the C-pocket.

Figures 4.20 and 4.21 show the resulting 50% and 90% C-burning lengths for this density (5×10^7 g cm^{-3}) over the range of resolutions that we considered. As mentioned above, the reaction rates are faster at this higher density and so the burning lengths are correspondingly shorter than the lower-density results. Here, we see roughly the same behavior as before with X14 giving C-burning lengths that are about $2\times$ the size of the other networks (due to the exclusion of the reaction branch of Equation 4.3). Because the detonations evolved with the X150 network exhibited oscillations at 10 levels of grid refinement and higher (0.03125 cm of resolution and lower), the C-burning lengths for these simulations are not accurate and the highest resolution result is not included due to its large extent relative to the scale shown in the figure. Neither the 50% or 90% C-burning lengths are resolved at this density by our coarsest grid resolutions, so both burning lengths converge as resolution is improved (except for the X150 results at 10 levels of grid refinement and higher due to oscillations).

The O-burning lengths show similar behavior to the lower-density results as well (Figures 4.22 and 4.23). As expected, the X14 network does a poor job of measuring these burning lengths, A13 and X14+ap+an give similar results as one another, and X150 shows significantly smaller values compared to all other networks. This behavior is due to the same reasoning as outlined above for the lower-density case and can be seen in Figure 4.24, which shows the ^{12}C, ^{16}O, and ^{28}Si mass fractions resulting from detonations evolved with the four reaction networks at this density. The scale of these plots shows the domain 15 cm in front of the shock and 5 cm behind it, so they have the same physical extent but include different regions of the domain. These results are taken from the highest resolution simulations for the X14, X14+ap+an, and Aprox13 networks, while the X150 results are taken from the 0.125-cm resolution run (due to oscillations at higher resolutions for this network). At this higher density, the C- and O-burning lengths can be seen on the same scale, because

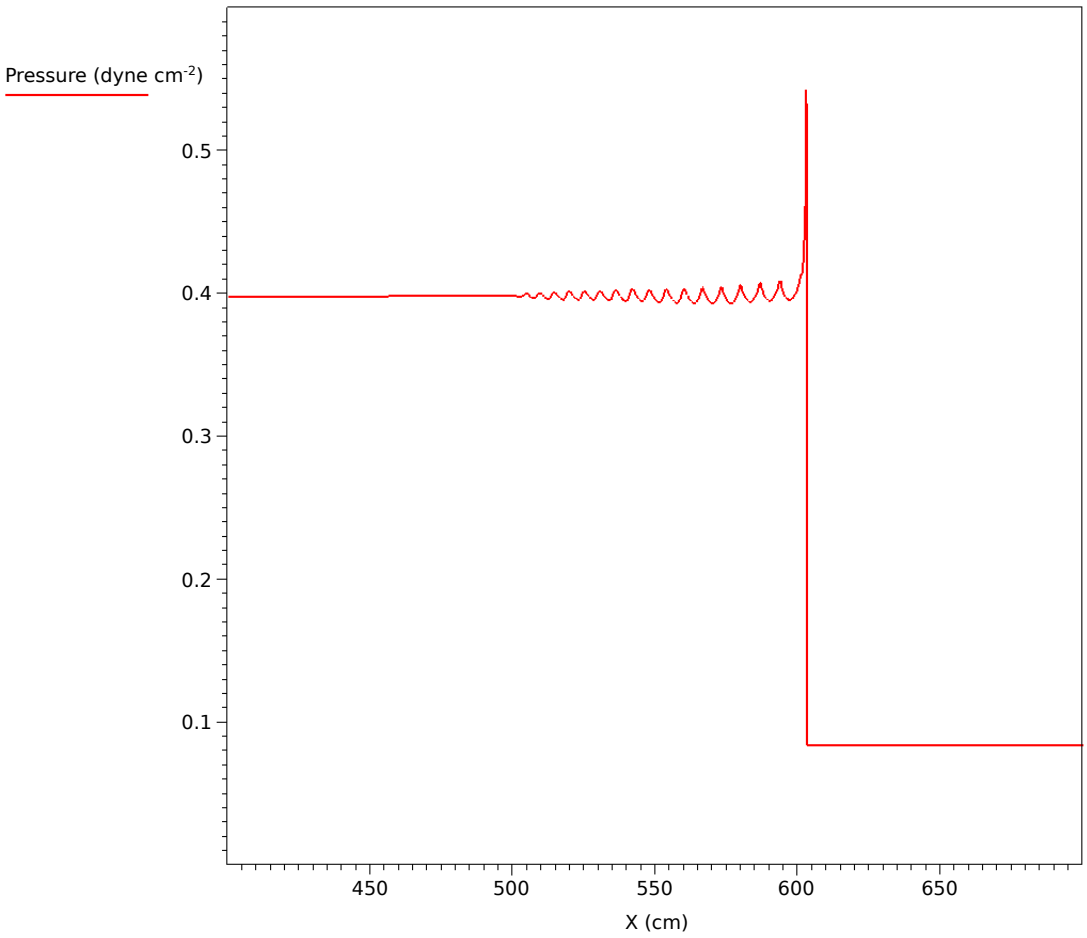


Figure 4.12: A pressure profile showing the oscillations behind the main shock front for a detonation evolved with the X150 network at 0.03125 cm resolution.

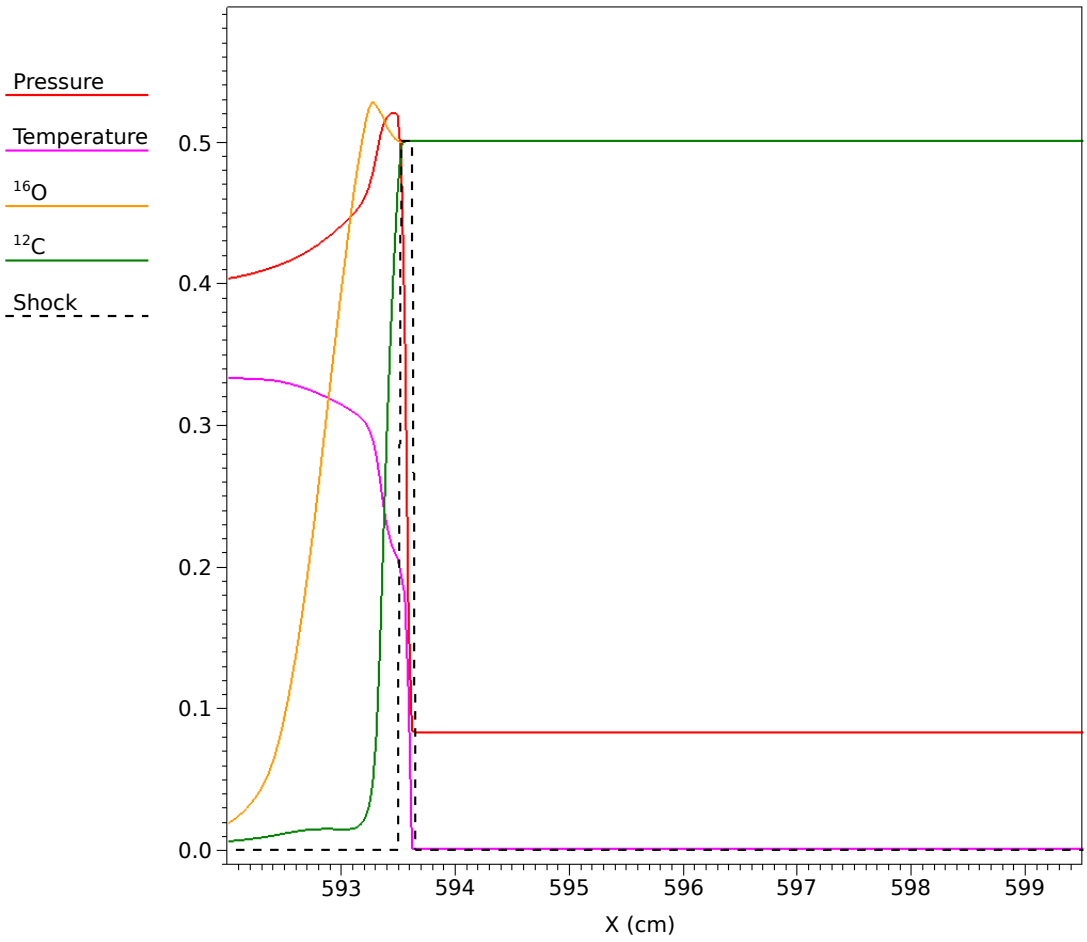


Figure 4.13: Thermodynamic and isotopic profiles along with the numerical shock. Here we see the C-pocket behind the shock before it explodes (t = 0.0 s).

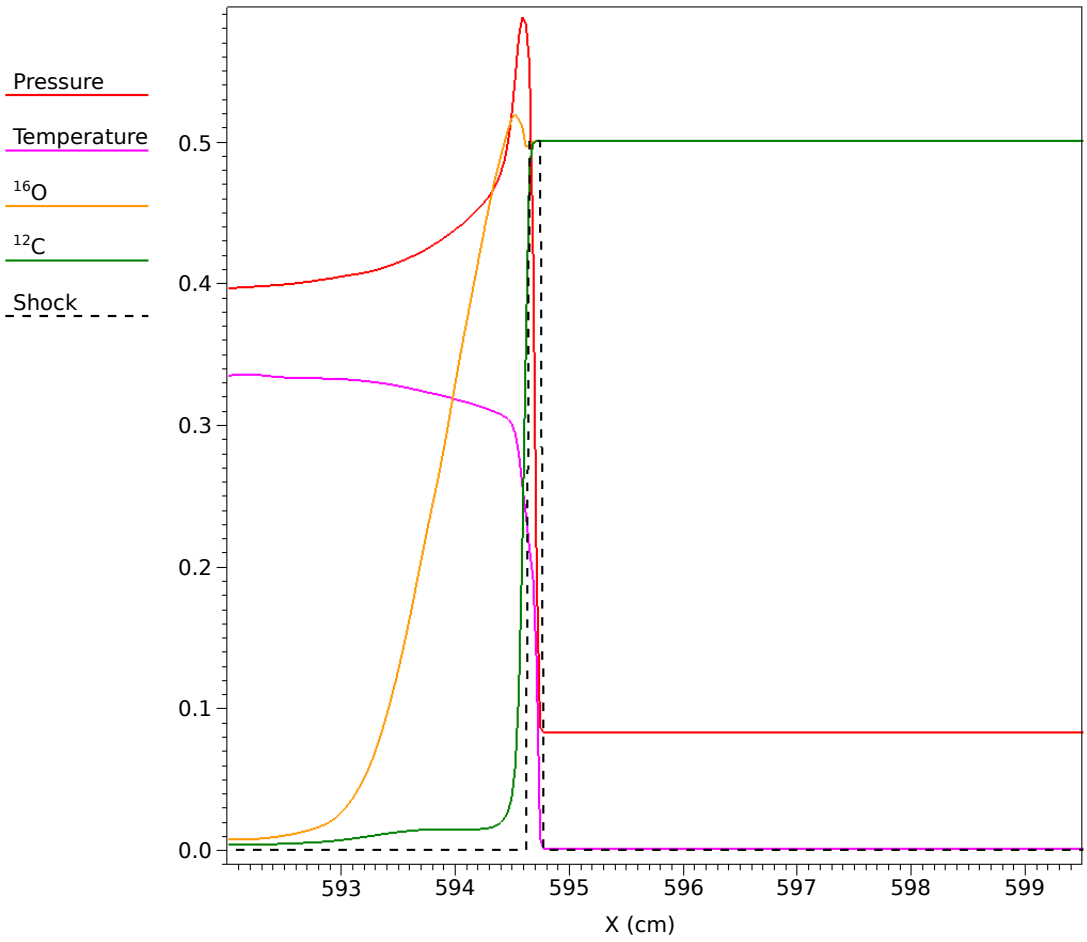


Figure 4.14: Thermodynamic and isotopic profiles along with the numerical shock. Here we see the profiles just after ignition of the C-pocket (t = 1.0×10^{-9} s).

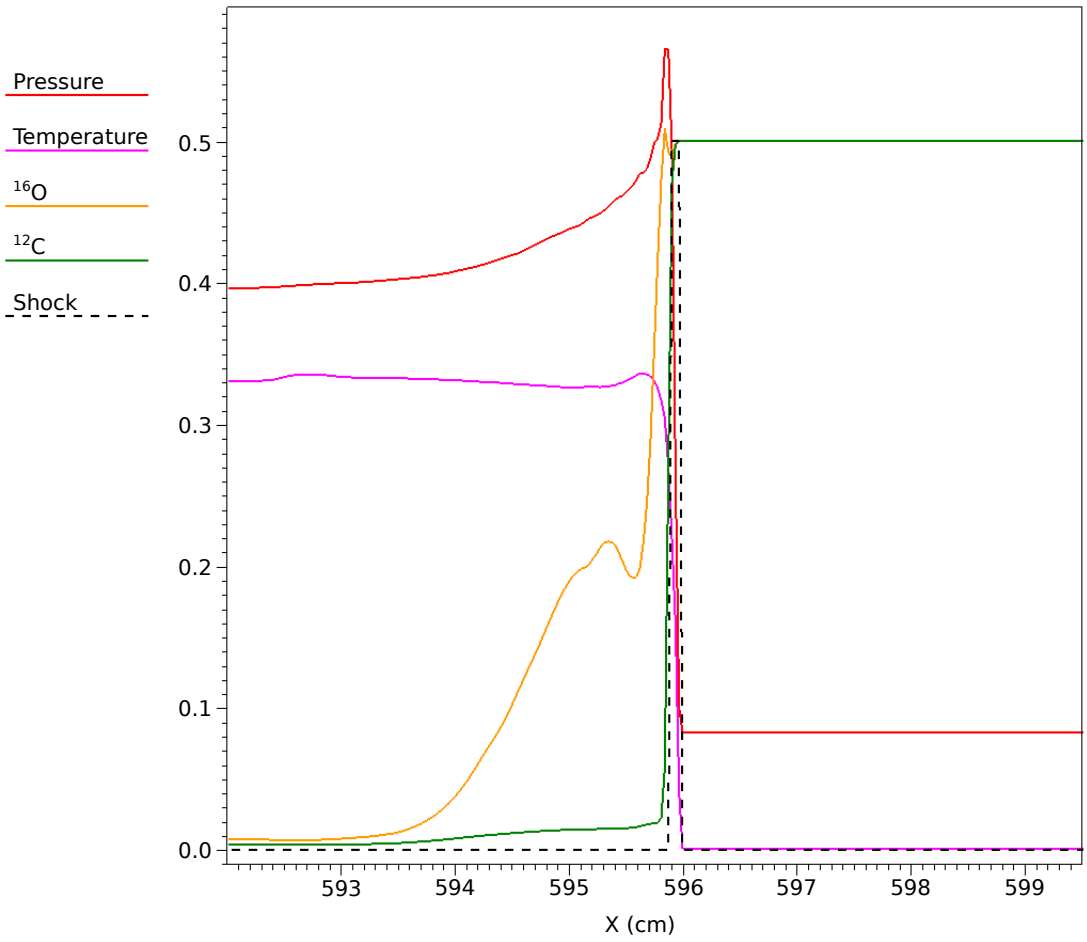


Figure 4.15: Thermodynamic and isotopic profiles along with the numerical shock. Here the C-pocket has finished burning and now the O-pocket has ignited (t = 2.0×10^{-9} s).

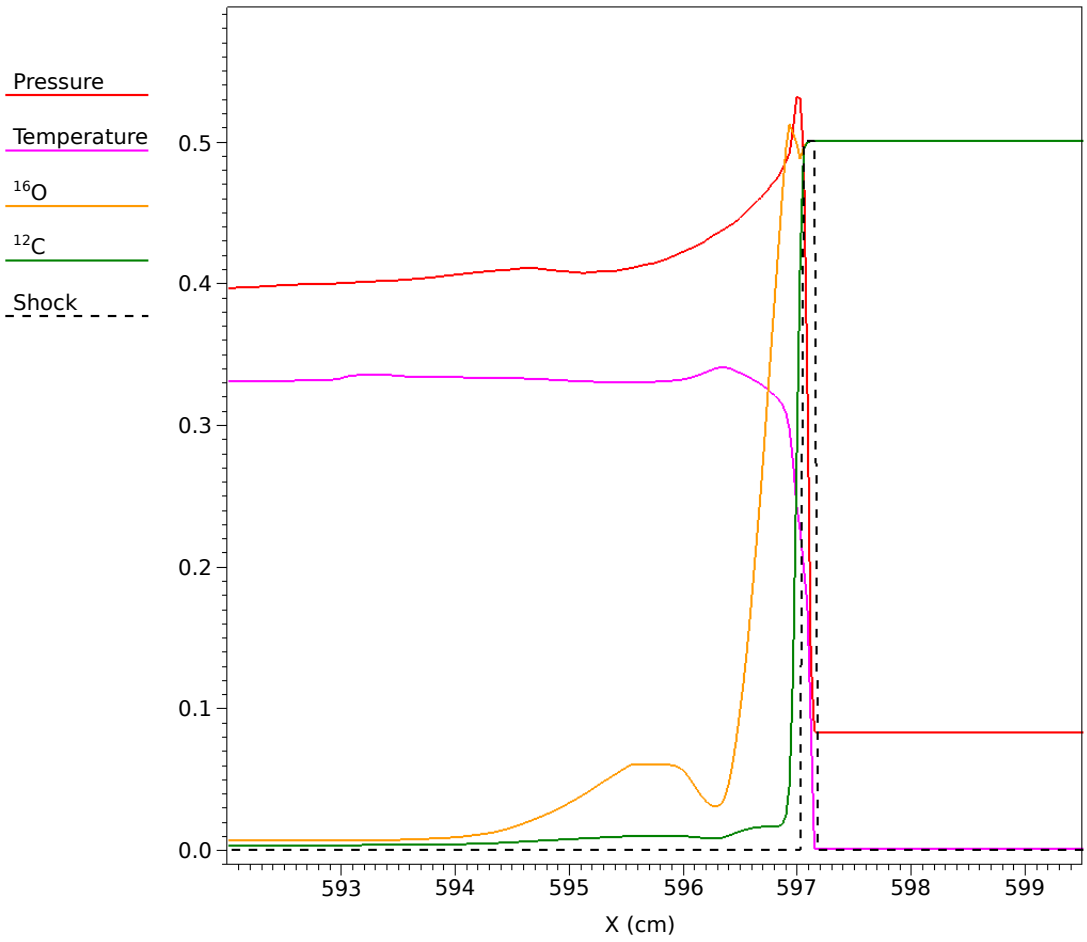


Figure 4.16: Thermodynamic and isotopic profiles along with the numerical shock. Here the C- and O-pockets are building back up (t = 3.0×10^{-9} s).

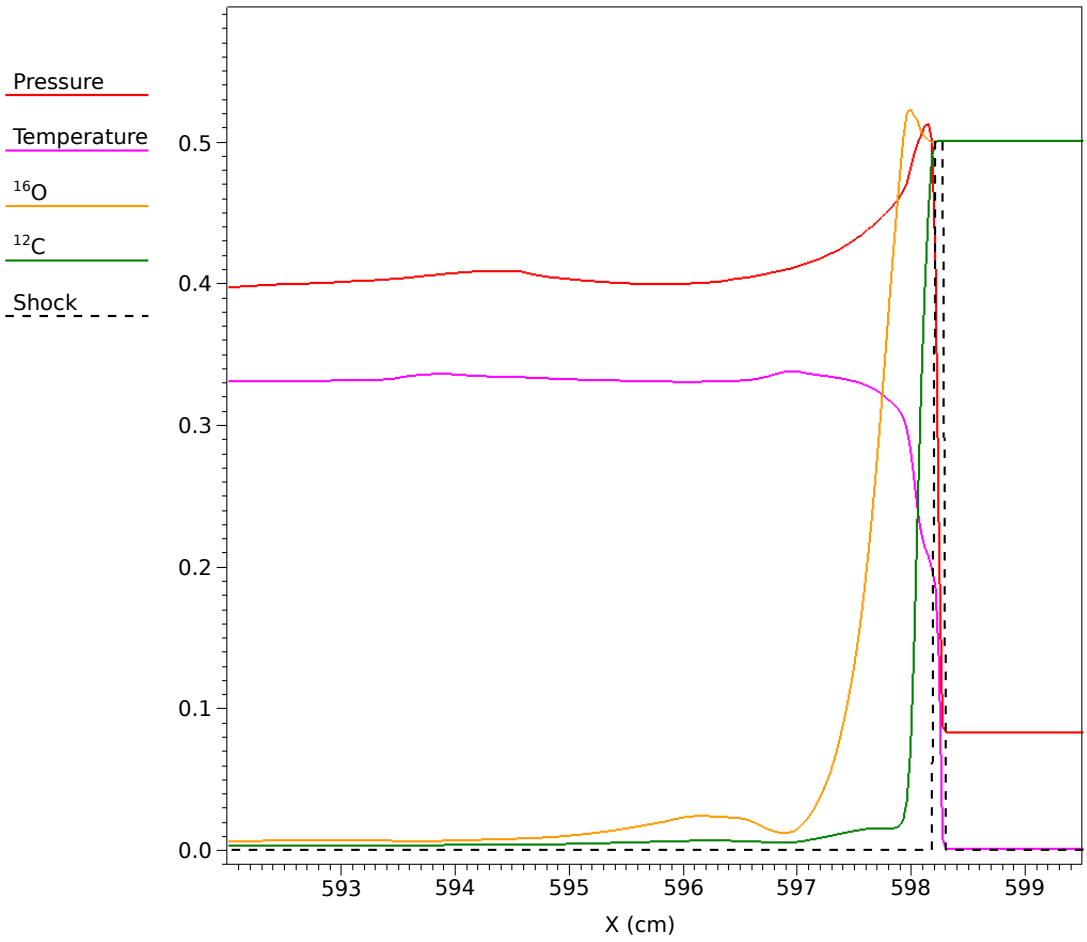


Figure 4.17: Thermodynamic and isotopic profiles along with the numerical shock. Here the C- and O-pockets continue to grow (t = 4.0×10^{-9} s).

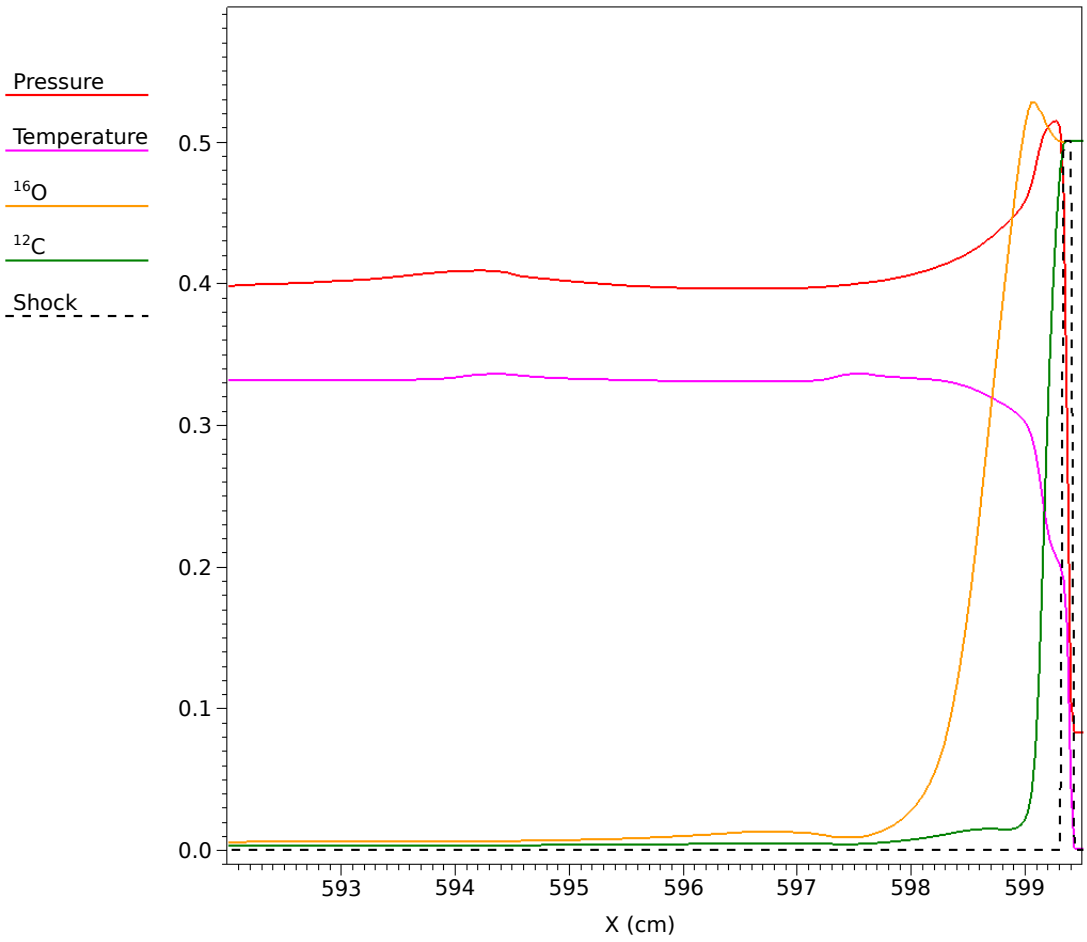


Figure 4.18: Thermodynamic and isotopic profiles along with the numerical shock. Here the profiles have returned to their initial states as in Figure 4.13 (t = 5.0×10^{-9} s).

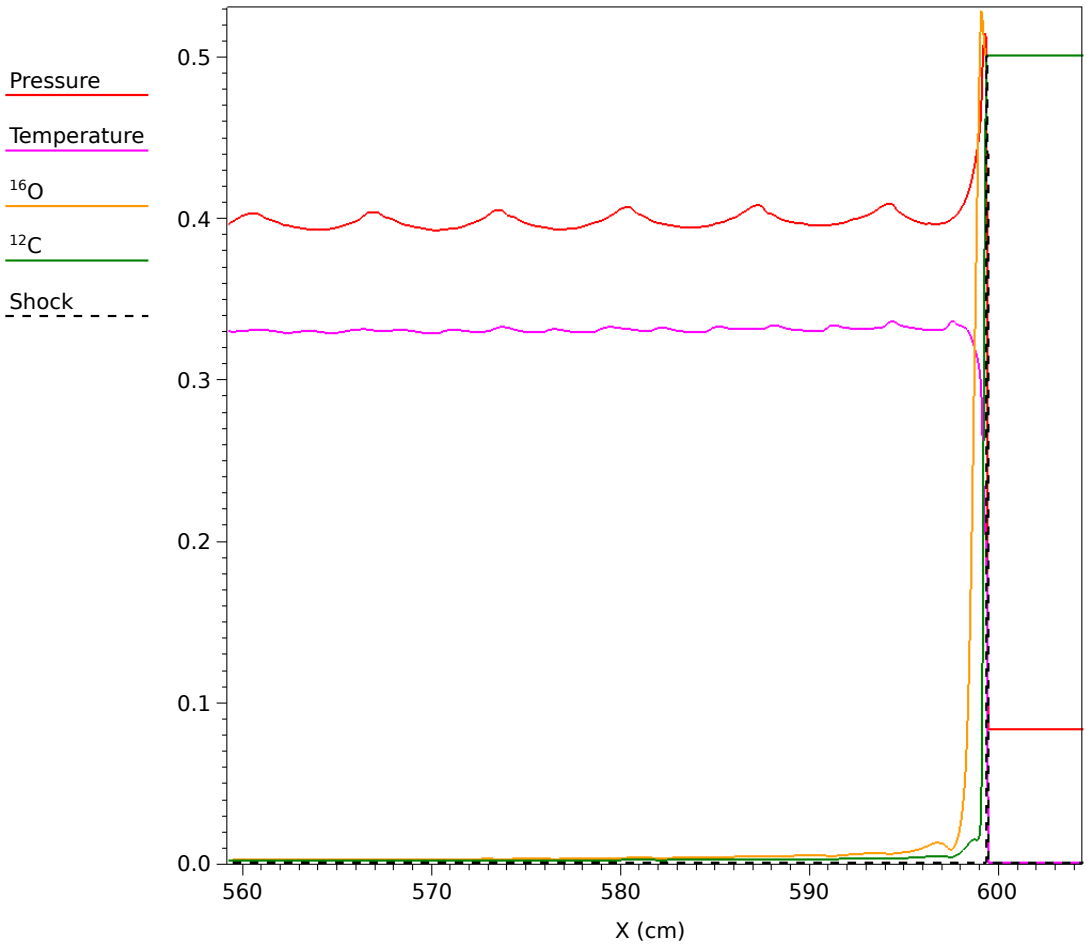


Figure 4.19: A larger view of the domain showing the oscillations embedded in the profiles.

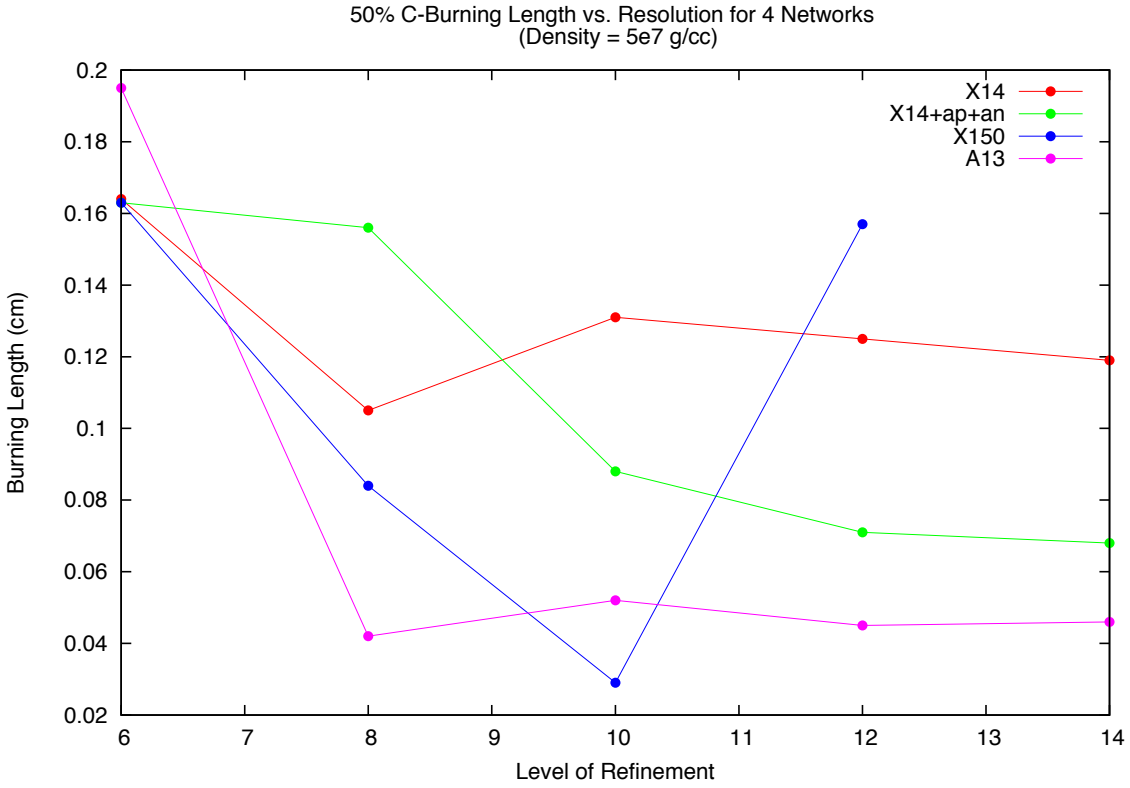


Figure 4.20: 50% C-burning length versus level of grid refinement for four reaction networks in Table 6.1. Level 6, 8, 10, 12, and 14 correspond to 0.5, 0.125, 0.03125, 0.0078125, and 0.001953125 cm resolution.

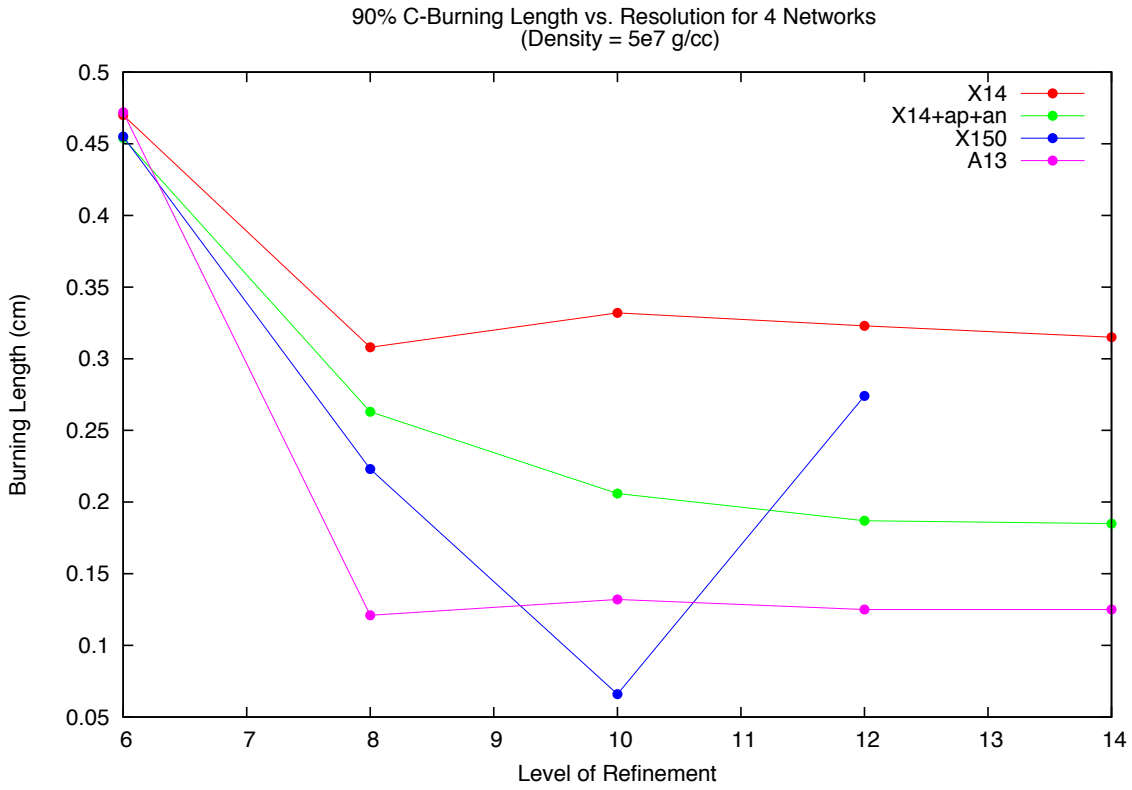


Figure 4.21: 90% C-burning length versus level of grid refinement for four reaction networks in Table 6.1. Level 6, 8, 10, 12, and 14 correspond to 0.5, 0.125, 0.03125, 0.0078125, and 0.001953125 cm resolution.

although both burning lengths are shorter relative to the lower-density case, the C-burning lengths have only been reduced by ∼3-5× whereas the O-burning lengths were reduced by ∼30-50×. As before, the Si-burning lengths are too large to be calculated on our domain. Here, the X150 results clearly show the peak and start of Si burning, again suggesting that the Si-burning lengths might be decreased similarly to the O-burning lengths when using this larger network. Although these O-burning lengths are smaller than their lower-density counterparts, they are still resolved at even our coarsest resolution, and therefore do not show a noticeable trend with maximum grid refinement. Note, however, that the deviations of the O-burning lengths for the X150 network are due to the oscillations and not resolution effects above 8 levels of grid refinement.

At this fuel density (5×10^7 g cm^{-3}), C/O detonations propagate in the pathological regime with velocities slightly larger than their CJ values. Previous studies (Gamezo et al., 1999b; Sharpe, 1999) have found a value of about 1.16×10^9 cm s^{-1} at the density considered here. Table 4.3 shows the values of the detonation velocities and overdrive parameters that we obtained from simulations using the four networks. Again, we see variation in these velocities that are due to a convolution of effects between the ignition (piston) and the burning that occurs as the detonation propagates when using different networks, but the variation is still small (∼2%). Figure 4.25 shows the detonation velocities for the highest resolution results for each network as they evolve and eventually reach a steady value (for X150, 8 levels of refinement is the highest refinement level achieved where oscillations were not present). Figure 4.26 shows the corresponding energy generation plots for these detonations. The transient features that were present in the lower-density results are not seen in the energy release or detonation velocity here because the burning rates are much faster at this higher density. Again, the detonation velocities do not appear to depend on grid resolution as can be seen in Figure 4.27, which shows the results for the Aprox13 network at the resolutions that we considered. Figure 4.28 shows the energy generation results for these simulations. Again, the similar results at different resolutions lead to the similar detonation velocities. All other networks showed the same behavior with resolution.

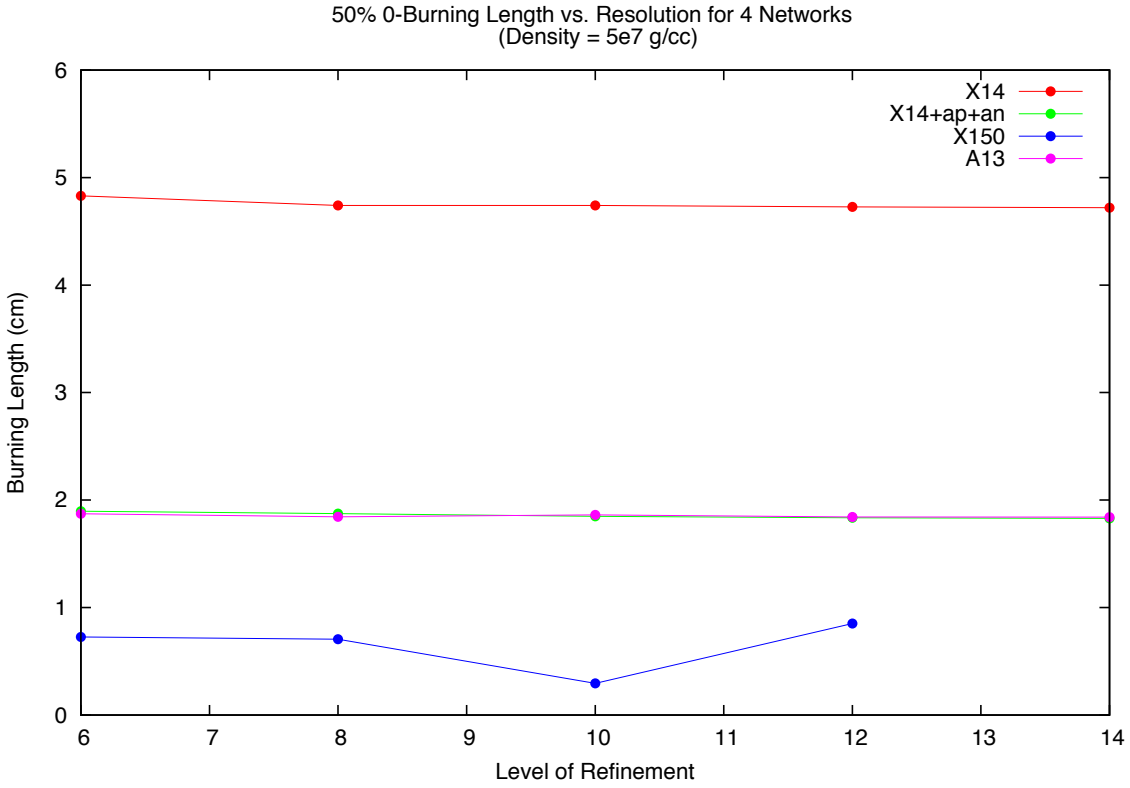


Figure 4.22: 50% O-burning length versus level of grid refinement for four reaction networks in Table 6.1. Level 6, 8, 10, 12, and 14 correspond to 0.5, 0.125, 0.03125, 0.0078125, and 0.001953125 cm resolution.

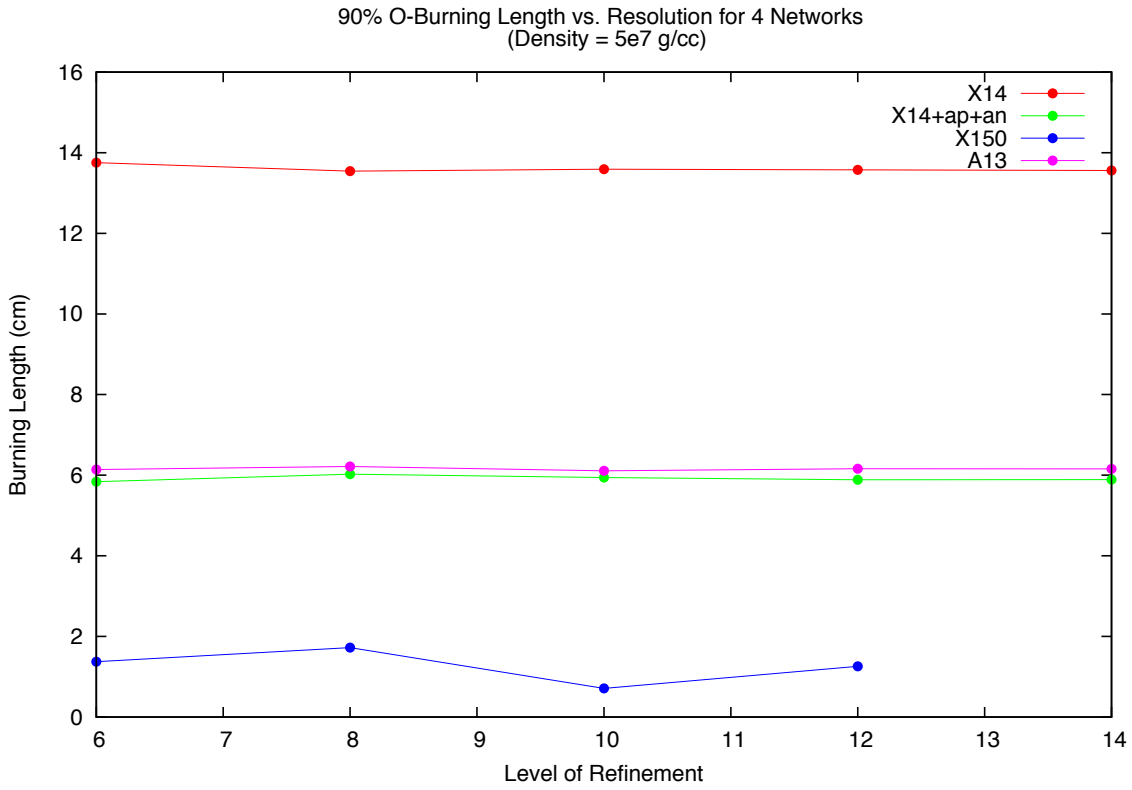


Figure 4.23: 90% O-burning length versus level of grid refinement for four reaction networks in Table 6.1. Level 6, 8, 10, 12, and 14 correspond to 0.5, 0.125, 0.03125, 0.0078125, and 0.001953125 cm resolution.

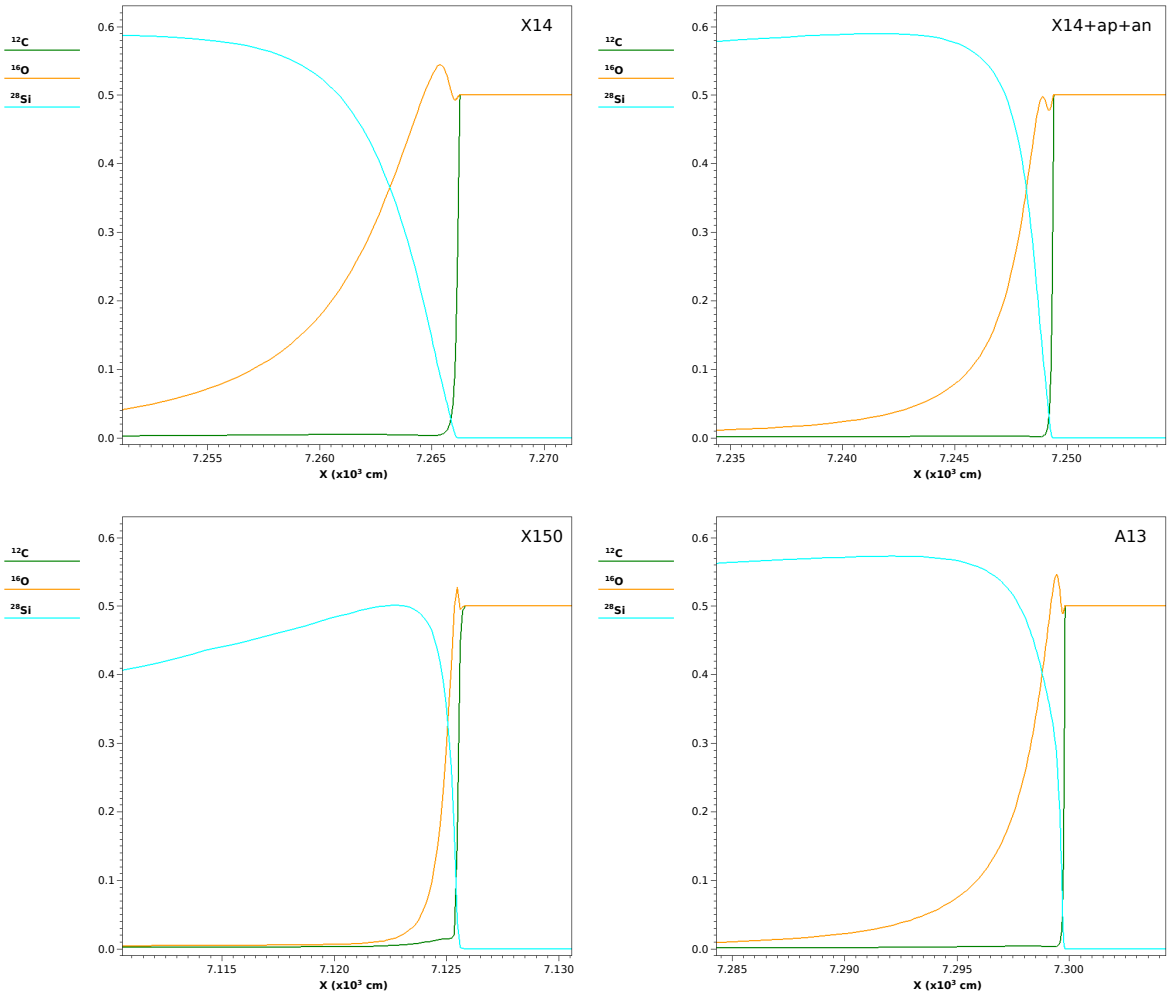


Figure 4.24: ^{12}C, ^{16}O, ^{28}Si mass fractions resulting from detonations with fuel density of 5×10^{7} g cm^{-3} (t=6×10^{-6} s).

Table 4.3: Detonation velocities and overdrive parameters calculated for the four reaction networks at a fuel density of 5×10^7 g cm^{-3}.

Network	D ($\times10^9$ cm s^{-1})	$f = (\frac{D}{D_P})^2$
A13	1.1745	1.0431
X14	1.1679	1.0314
X14+ap+an	1.1647	1.0257
X150	1.1430	0.9879

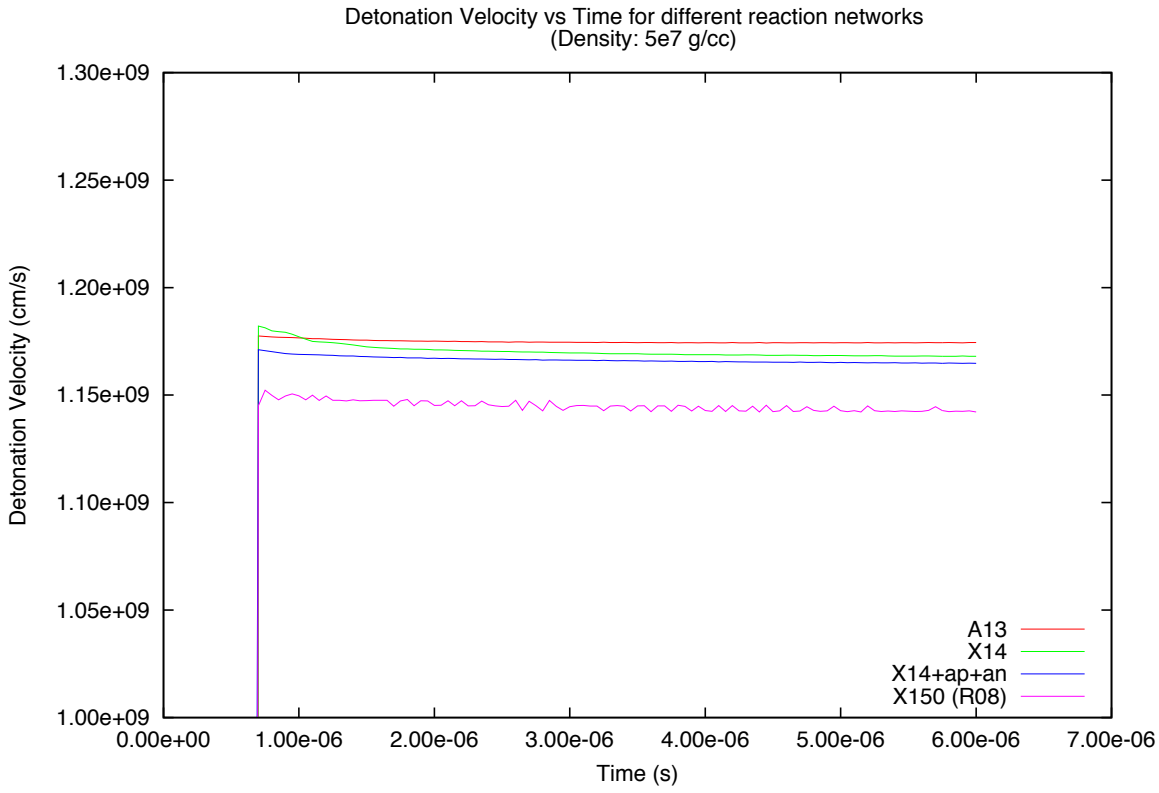


Figure 4.25: Detonation Velocity vs Time for the four nuclear reaction networks.

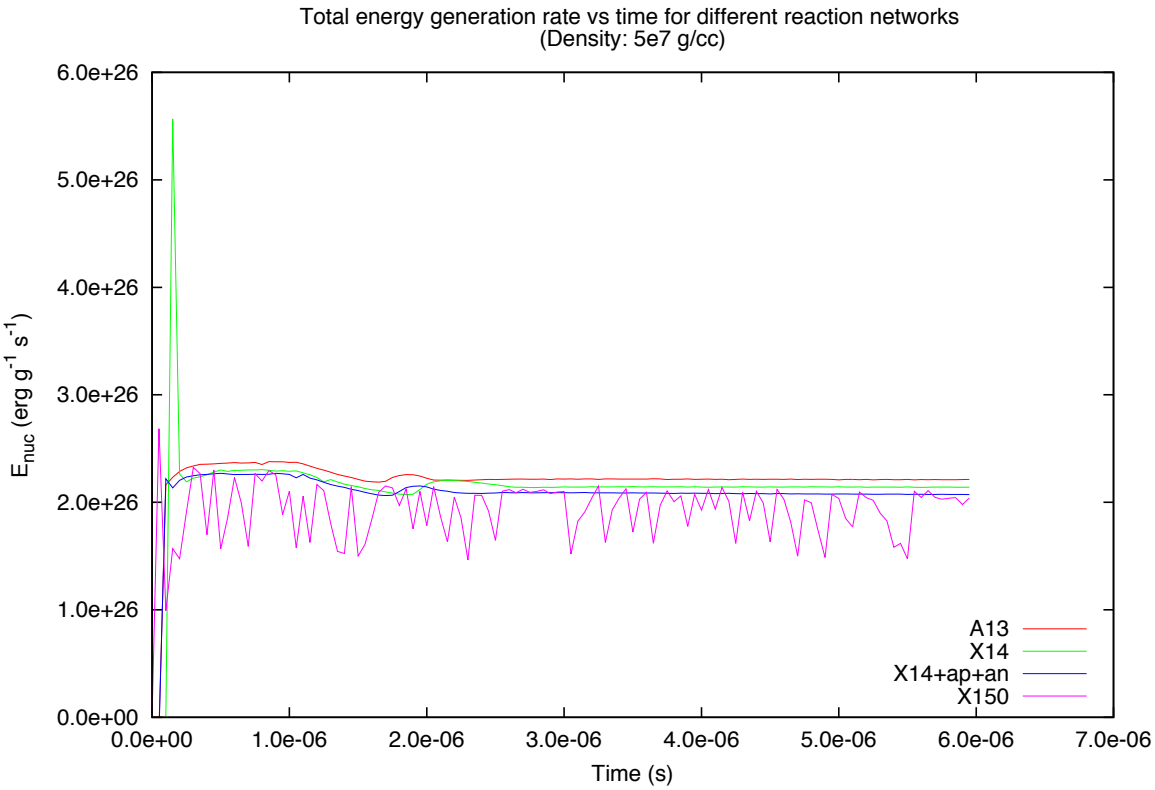


Figure 4.26: Total energy generation rate vs time for the four nuclear reaction networks at the highest grid resolution.

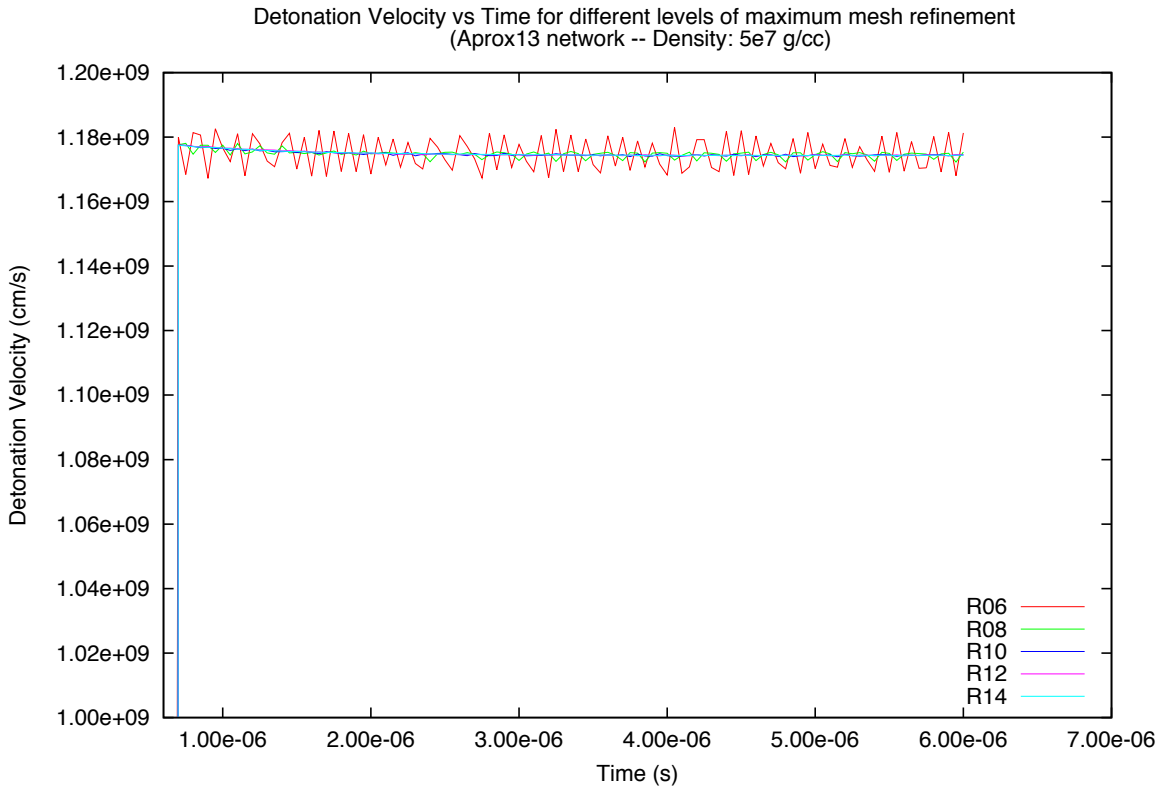


Figure 4.27: Detonation Velocity vs Time for the Aprox13 network at different resolution.

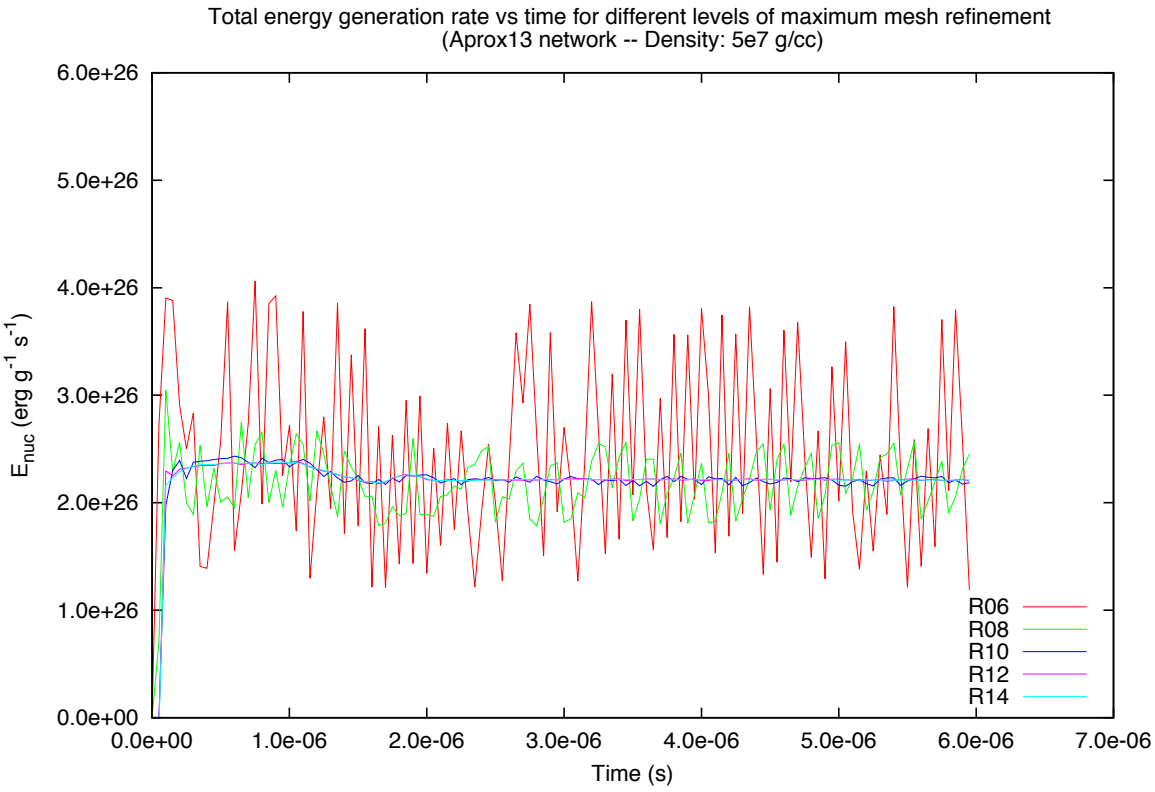


Figure 4.28: Total energy generation rate vs time for the Aprox13 network at different resolution.

4.3 Conclusions

In this chapter, we have shown that the 1D C- and O-burning lengths (and possibly Si-burning lengths) have a dependence on nuclear network size that is determined by the reaction channels available to each network. In general, larger networks that have more reaction pathways to diminish a given isotope have smaller burning lengths relative to reduced networks with fewer pathways. This is only true however if the additional reactions of the larger network have reaction rates that are comparable to the reaction channels shared

by both networks. Another caveat is exemplified by the Aprox13 network, which has hand-tuned C-reaction rates to give comparable energy generation rates to those of larger networks. The C-burning lengths measured for this network were shown to be comparable to those of the 150-species network, but the O-burning lengths were not comparable because there was no tuning of the O-reaction rates. In addition, we also showed that as resolution is improved, the C-burning lengths converged in size, whereas the O-burning lengths were unaffected by resolution due to having larger physical extents relative to the range of grid resolutions that we considered. The detonation velocities that we measured do not appear to be strongly dependent on network size. This is due to the fact that the energy release is roughly the same when processing the C/O fuel with different networks. It was also shown that these detonation velocities do not have a dependence on resolution. Again, this is because the total amount of energy that is released is the same even if the distribution of this energy release is different as resolution is improved. However, this argument hinges on the fact that the entire reaction zone is in sonic contact with the front. For a non-supported, pathological detonation a coarsely resolved grid, might displace a portion of the energy release beyond the sonic point so that it cannot be used to drive the detonation.

The most resolved full-star SNe Ia simulations to date have computational zones of about 1 km, with corresponding time steps of about 10^{-4} s. Burning that occurs at high densities ($> 10^8$ g cm^{-3}) in such simulations will proceed directly to iron-group elements because the burning lengths (time scales) for even Si are unresolved. However, at lower densities ($< 10^7$ g cm^{-3}) the burning lengths for Si and O can be resolved on these coarse grids, and become important in determining the amount of intermediate-mass elements that remain after an explosion. Therefore, we assert that the reduction in O-burning lengths (and possibly Si-burning lengths) that we found in this chapter can alter these incomplete burning products at a given low density whether using large *in situ* nuclear reaction networks or incorporating these results into approximate burning models as is attempted in Aprox13. Our results might also be used to address high fidelity nuclear burning simulations on smaller scales. For example, Seitenzahl et al. (2009) investigated the critical radius needed for successful

ignition of C/O detonations within a large range of fuel densities. They found that no failures occurred for radii large enough to successfully ignite O, and so used O ignition as their criteria for success of a detonation. They performed their simulations with the Aprox13 network in FLASH. In doing so, they recognized that using this network only gives energy generation rates within $\sim$20% of a larger network, however they did not take into account the effects of reduced burning lengths from using larger networks. Both of these considerations (increased energy release and reduced O-burning lengths) might affect the criteria for ignition resulting from such a study, which are used to decide whether or not to manually ignite a detonation in unresolved full-star explosion models.

Chapter 5

Multi-D Simulations

In this chapter we extend our investigation of detonation characteristics into higher dimensions. As discussed in Chapter 2, cellular structure can increase the effective burning lengths for a particular fuel by extending the region behind the shock where that fuel has been depleted everywhere by a given amount. In addition, pockets of unreacted fuel can persist into the reaction zone, which are capable of reducing detonation velocities in 2D relative to 1D. Here, we attempt to quantify those differences for detonations in our lowest-density environment (1×10^7 g cm^{-3}) as we improve resolution and the fidelity of our nuclear kinetics. In addition, we compare the size, shape, and regularity of the detonation cells as we make these improvements.

5.1 2D

The numerical models used in this section are very similar to those of the previous chapter. The computational domain spanned 8192 cm in length by 128 cm in width with outflow boundary conditions at the left and right ends and periodic conditions along the width (at y = 0 and y = 128 cm). As before, the outflow boundary conditions provided necessary support to the back of our detonations. We ignited these detonations with a hotspot that was 250 cm in length and 128 cm in width, with elevated temperature, density and x-velocity of 4.5×10^9 K, 4.25×10^7 g cm^{-3}, and 3.5×10^8 cm s^{-1}. Similar to the setup used for the 2D

simulations in Chapter 3 (see Section 3.2), we added random perturbations to the density of the fuel with values ranging from 1% above to 1% below the density given to the rest of the fuel in order to encourage the formation of cellular structure. These perturbations were confined to a region that was 5 cm in length, 128 cm wide (width of the domain), and placed 20 cm in front of the hotspot.

The most striking difference between 1D and 2D detonations, as demonstrated in Chapter 3, is the formation of cellular structure. Figures 5.1 - 5.4 show this structure for detonations evolved with each of the four reaction networks introduced in Chapter 4. These figures show that the size and regularity of the detonation cells differ when using each network. In addition, the strength of the triple-points and the curvature of the front also appear to depend on the network size. Table 5.1 presents the detonation cell sizes for all four reaction networks at 6 and 8 levels of grid refinement, and for X14 and Aprox13 the results are given at 10 levels of refinement as well. At the lowest resolution, the detonations evolved with X14, X14+ap+an, and Aprox13 all exhibit large, very regular detonation cells. The X150 detonation also produces very regular cell sizes at this resolution, but with a smaller cell size relative to the other networks. At 8 levels of refinement (Figures 5.1 - 5.4), the X14 cells remain large while the X14+ap+an and Aprox13 cells have evolved to a slightly more irregular pattern with cells sizes about half the length as at the lower resolution. The X150 cells have also decreased at higher resolution, and have a smaller length-to-width ratio than the other networks. At 10 levels of refinement, the X14 cells have decreased in size, now having values similar to the other networks. The Aprox13 cells are approximately the same at 8 and 10 levels of refinement, suggesting they have converged in size.

The cell sizes that we have reported here appear to be consistent with previous studies. Gamezo et al. (1999b) investigated cellular detonations in C/O fuel with densities in the range 10^6-3×10^7 g cm^{-3}. Although they used a different hydrodynamics scheme (flux-corrected transport technique) and different reaction rates in their nuclear reaction network, the cell sizes that we estimate from their results are similar to ours: 13.2 cm by 7.0 cm with a length-to-width ratio of 1.9. Timmes et al. (2000b) investigated cellular detonations in pure

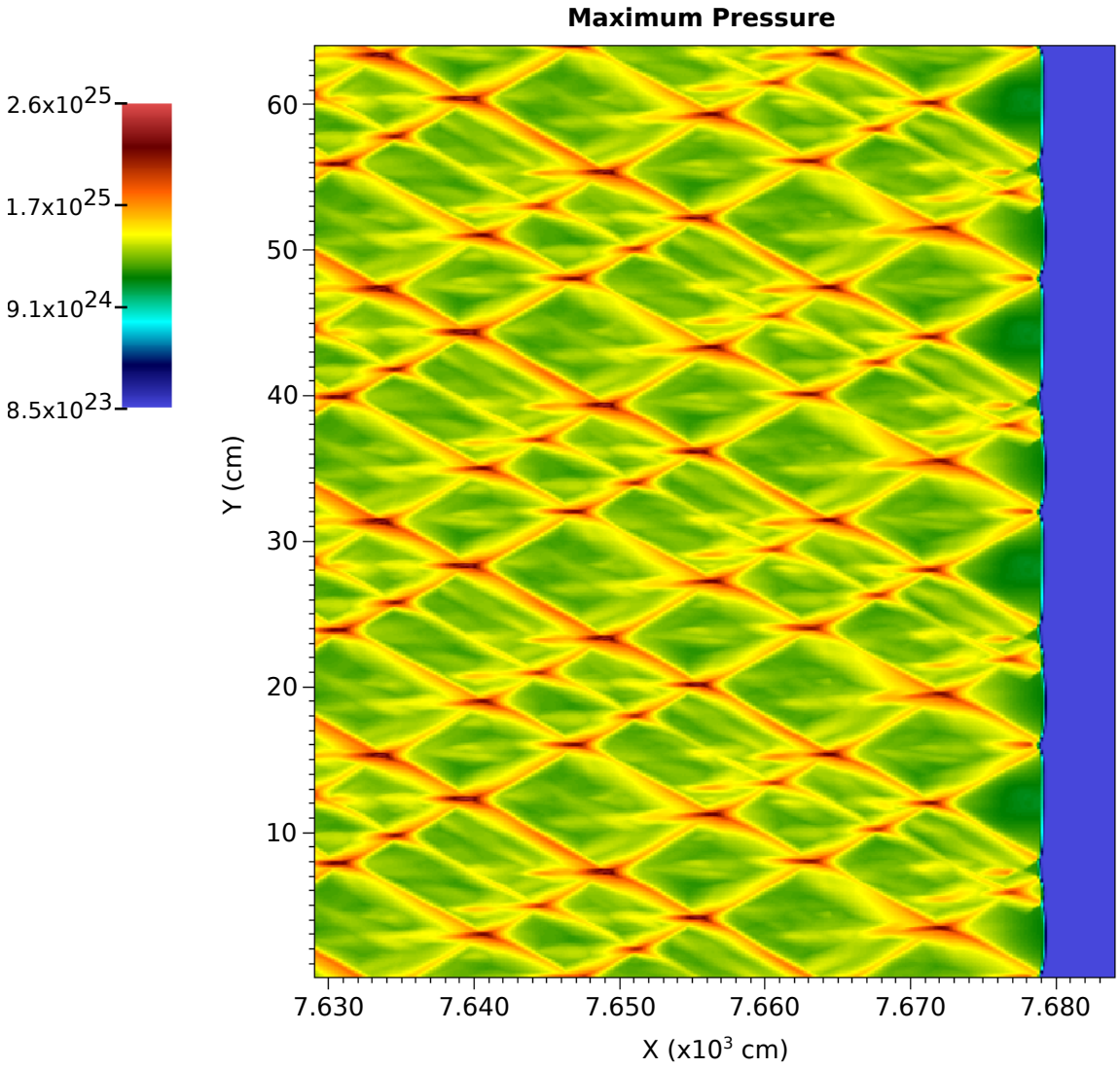


Figure 5.1: Cellular structure shown by a plot of the maximum pressure achieved at each grid zone during the simulation evolved with the Aprox13 network. Note the scales of the plots in Figures 5.1, 5.2, 5.3, 5.4 are different in order to show the cellular features from each network.

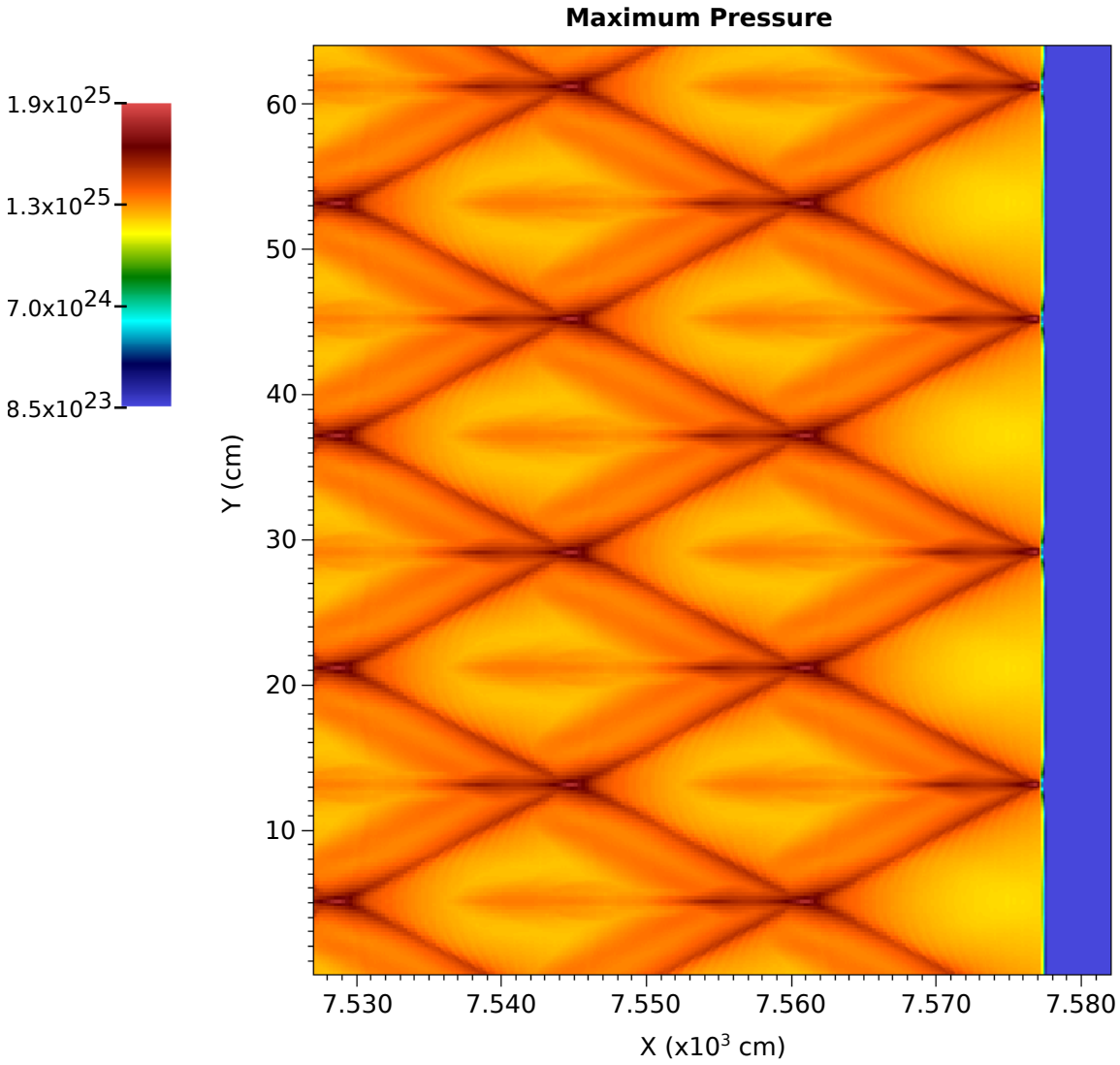


Figure 5.2: Cellular structure shown by a plot of the maximum pressure achieved at each grid zone during the simulation evolved with the X14 network. Note the scales of the plots in Figures 5.1, 5.2, 5.3, 5.4 are different in order to show the cellular features from each network.

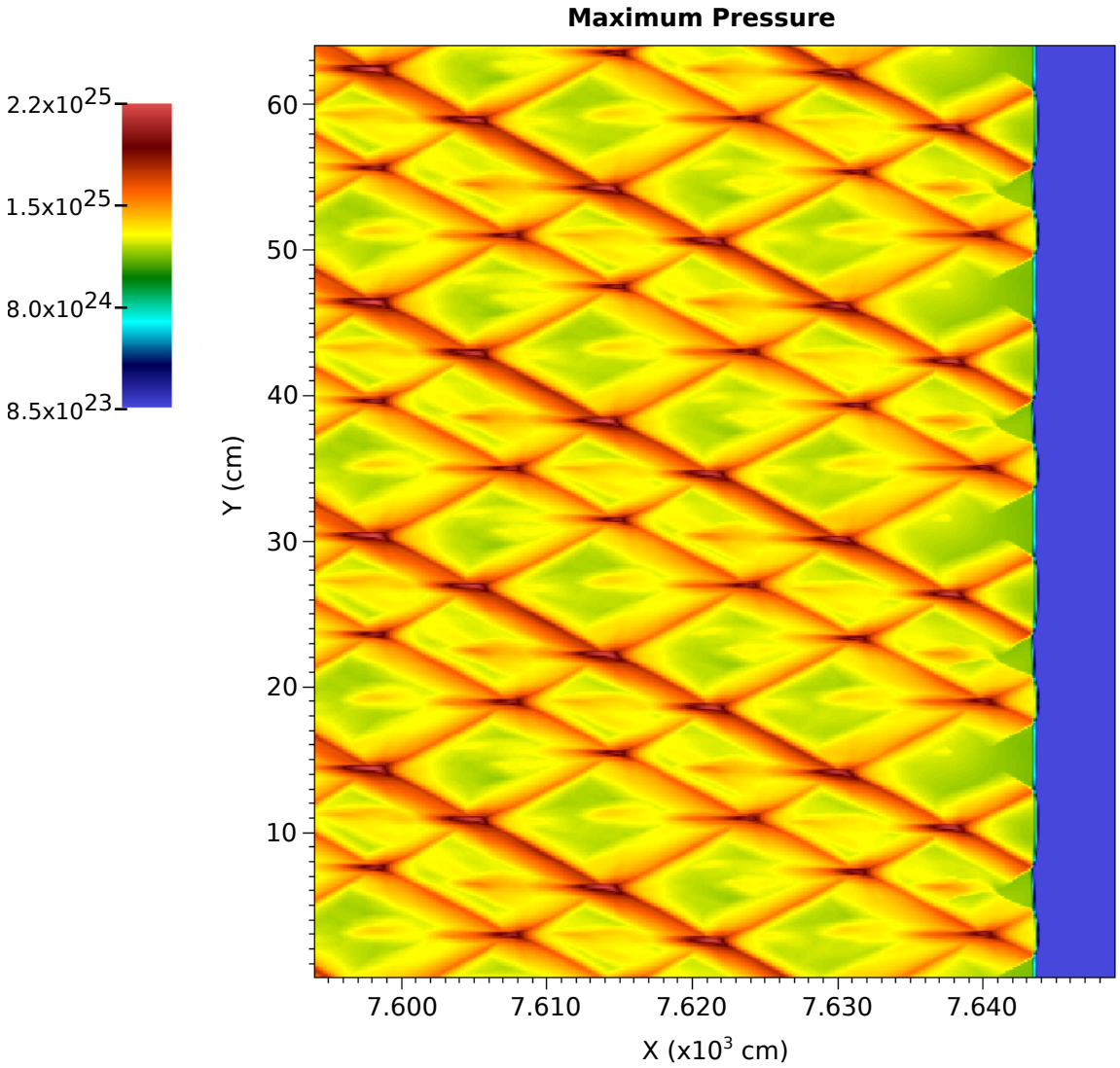


Figure 5.3: Cellular structure shown by a plot of the maximum pressure achieved at each grid zone during the simulation evolved with the X14+ap+an network. Note the scales of the plots in Figures 5.1, 5.2, 5.3, 5.4 are different in order to show the cellular features from each network.

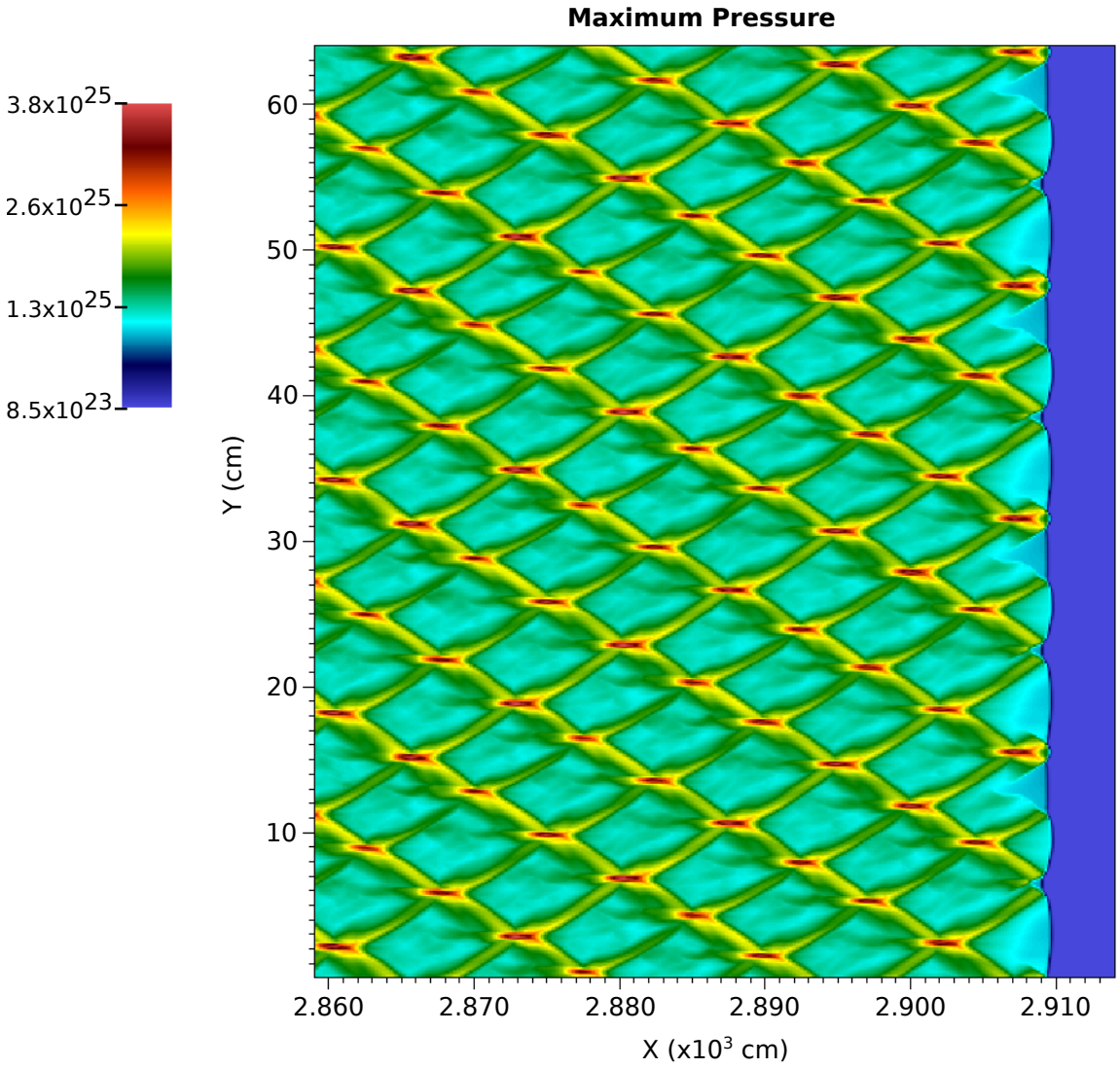


Figure 5.4: Cellular structure shown by a plot of the maximum pressure achieved at each grid zone during the simulation evolved with the X150 network. Note the scales of the plots in Figures 5.1, 5.2, 5.3, 5.4 are different in order to show the cellular features from each network.

C at a density of 1×10^7 g cm^{-3}. They also used the FLASH code with the Aprox13 network and found cells sizes of 6.0 cm by 3.8 cm with a length-to-width ratio of 1.6. The pure C composition of their fuel is most likely the reason for the smaller cell sizes that they measured relative to ours and those of Gamezo et al. (1999b) because the C+C reaction rates are dependent on the ^{12}C abundance. In addition, although the X14+ap+an and X150 detonation cells might not be fully converged at 8 levels of refinement, there appears to be a trend of decreasing length-to-width ratios with resolution and also with larger reaction networks. The smaller size of the X150 detonation cells might also be a general feature of using more realistic nuclear kinetics.

The 2D C-burning lengths were calculated analogously to their 1D counterparts at various locations along the cellular detonation front (Figures 5.5 and 5.6). The colored lines in Figure 5.5 record 1D samples of the ^{12}C mass fraction along their lengths. Figure 5.6 displays these 1D recordings, showing their differences at various positions along the front. Similar to Chapter 4, we measured the burning lengths from the back of the numerical shock (slightly curved, white region ahead of the front) to the coordinate where the ^{12}C mass fraction has been depleted by 50% or 90% of its initial value. Two hundred of these measurements were taken for each simulation and their minimum, maximum, and average values were calculated. The 2D O-burning lengths were measured differently due to extensive mixing that occurs deeper in the reaction zone. Figure 5.8 shows this mixing in the ^{16}O mass fraction resulting from the detonation evolved with the Aprox13 network at 10 levels of grid refinement. The mass fraction is only plotted in zones where its value is 0.25 (50% of its initial value) or higher in order to illustrate the ambiguity in measuring its 50% O-burning length among this mixing. Along a line extending from the numerical shock into the reaction zone, there can be pockets of fluid whose ^{16}O mass fraction is below 0.25 (white regions such as the one indicated at the tip of the arrow) although the pocket is surrounded by fluid with higher ^{16}O mass fractions. If measurements are made analogously to 1D in this case, then the extent of the 50% O-burning length would terminate when one of these pockets are encountered, leaving large amounts of fluid with ^{16}O mass fraction above 0.25 unaccounted for in the

calculation. Even when recognizing this issue, it is unclear what is the best method for making these measurements. Therefore, we used two different approaches and report both of them. In the first method, we measured from the back of the numerical shock to the left-most coordinate where the ^{16}O mass fraction was greater than or equal to 0.25 (Figure 5.9). We calculated two hundred of these measurements and recorded the minimum, maximum, and average values. In the second method, we measured from the average shock location to the coordinate behind the shock where the ^{16}O mass fraction (averaged over y along a given x-coordinate) was 0.25 (red vertical line in Figure 5.9). The average 50% O-burning lengths calculated by the two methods were not the same in all cases. In fact, the averages calculated with method 2 were generally more similar to the minimum values calculated from method 1. This illustrates the rapidity with which the fractional volume of matter with X(^{16}O) ¿ 0.25 declines in this partly mixed region. The 90% O-burning lengths were similar in all cases (method 1 min, max, avg, and method 2 avg) due to the mixing having more time to homogenize the fluid further behind the shock, and also perhaps due to derefinement in some cases.

Tables 5.2-5.5 show these burning lengths as measured for detonations evolved with each of the four reaction networks. The corresponding 1D burning lengths are also included for comparison. In all cases, as the resolution is improved, the average C-burning lengths decrease, but only the average 50% C-burning lengths are consistently larger than their 1D counterparts. The minimum and maximum values for the C-burning lengths arise from burning behind triple-points and weak incident shocks, respectively, at the front. The strong thermodynamic conditions in the triple-points over-process the ^{12}C relative to the 1D conditions while the weaker conditions of the incident shocks under-process the ^{12}C, allowing burning lengths that extend further into the reaction zone relative to 1D. This behavior can be seen in Figure 5.7, which shows the detonation cells superimposed on the ^{12}C mass fraction for the X14 results at 8 levels of grid refinement. The very regular cell structure in this simulation makes it easy to see the distinction between the burning that occurs behind the triple-points (indicated by arrows in the figure) and the weak incident

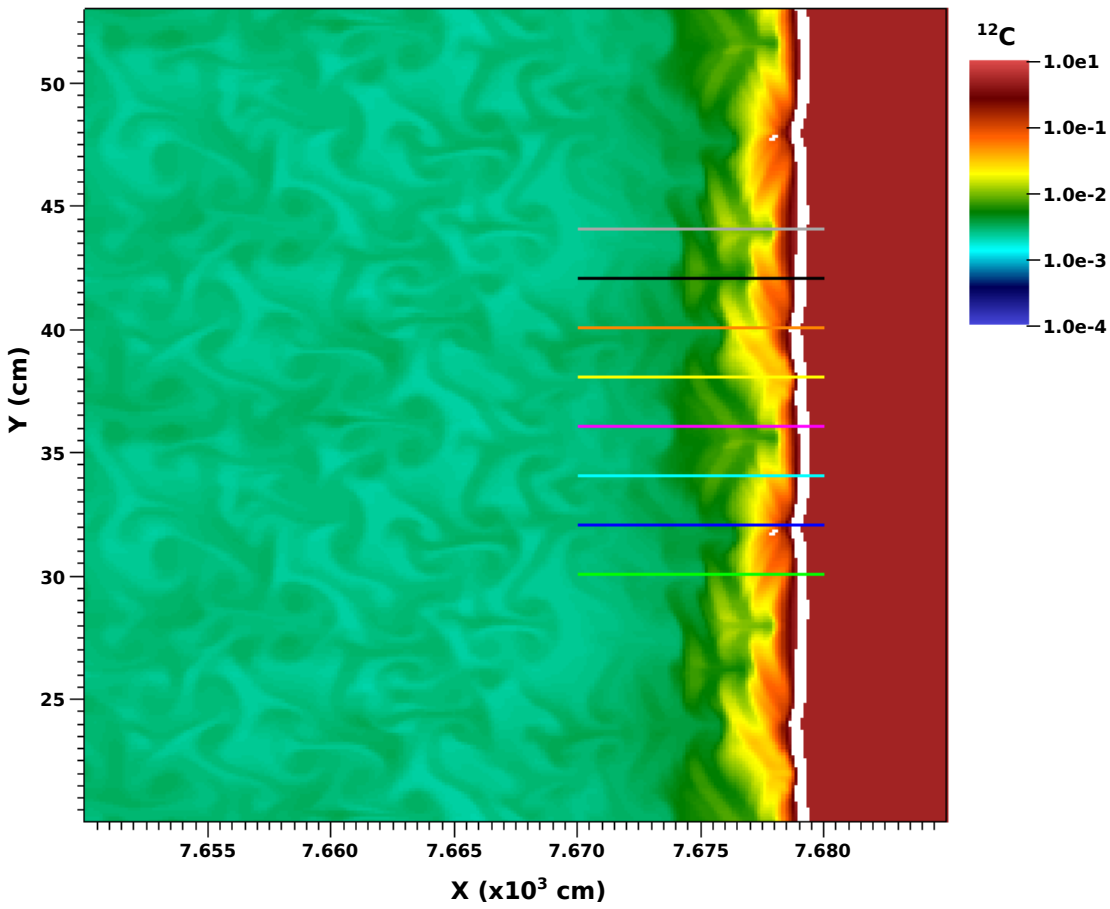


Figure 5.5: Log-plot of the ^{12}C mass fraction along with several 1D samples (see Figure 5.6) along the front. The numerical shock is shown in white.

shocks between them. The average O-burning lengths tend to increase or stay roughly the same as resolution is improved. In this case, the minimum and maximum values are not due to interaction with the features of the detonation front, but rather due to the extensive mixing that occurs in the following flow. The vorticity that drives this mixing is caused by collisions of the transverse waves behind the front. It is unclear from the literature how the burning lengths should be (have been) measured, and with various ways to define them, the method that is chosen for a particular study is best determined by its objective.

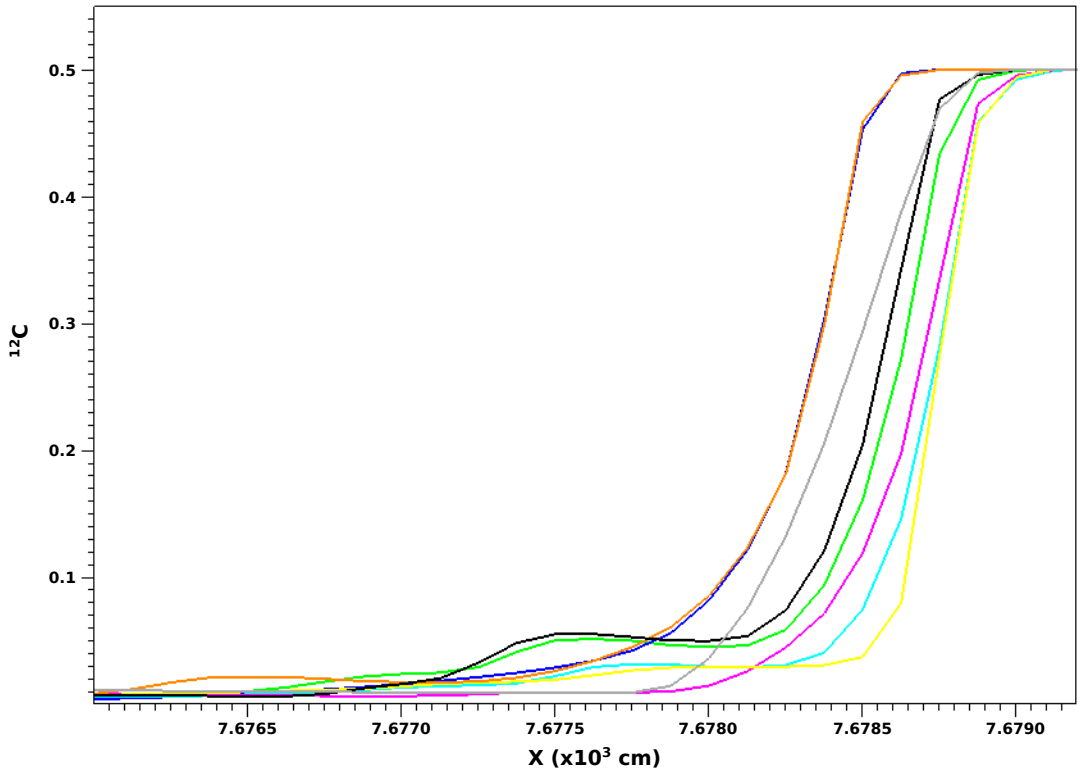


Figure 5.6: ^{12}C profiles resulting from the 1D samples taken in Figure 5.5. These profiles show the differences in the ^{12}C mass fraction at different locations along the detonation front.

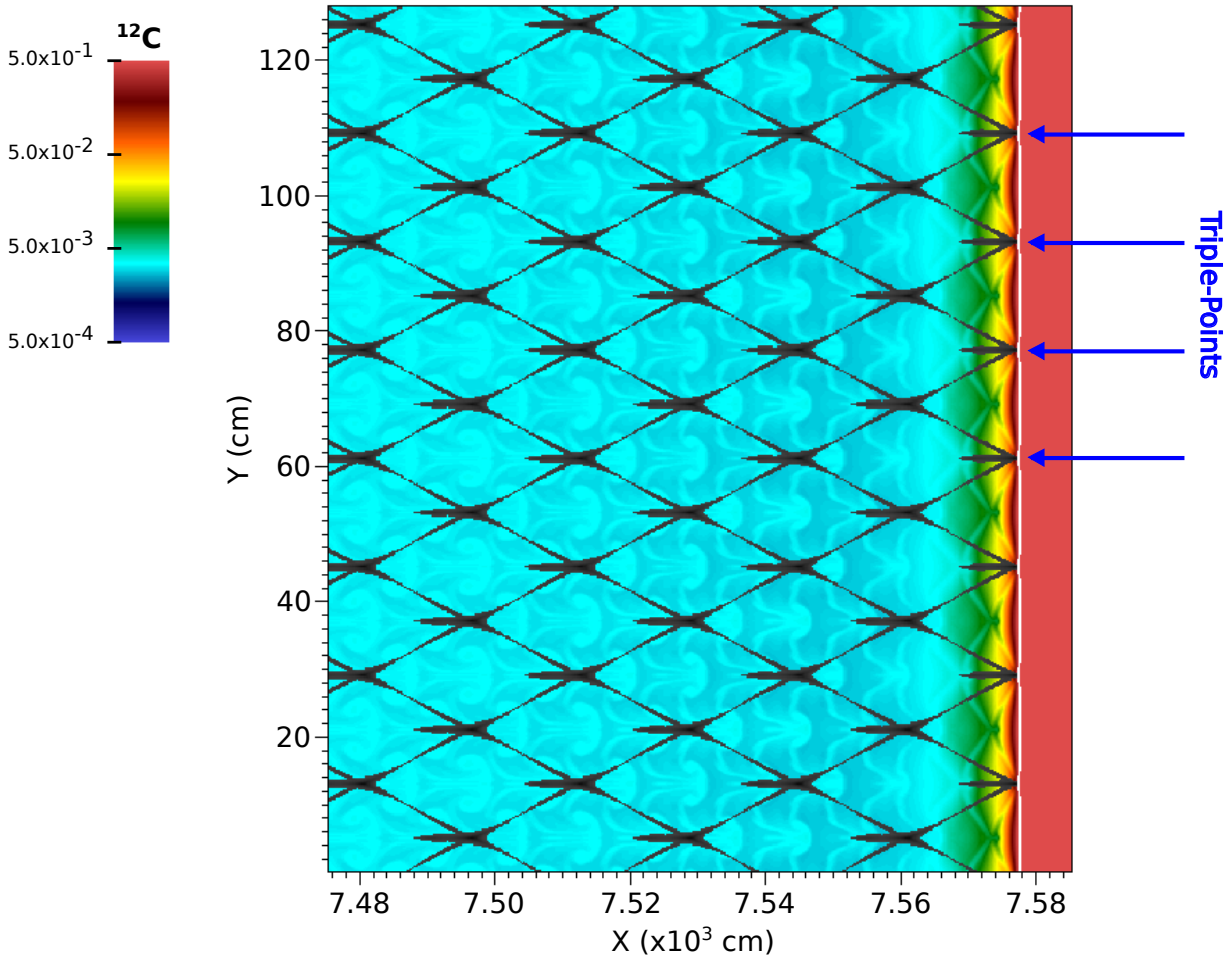


Figure 5.7: Detonation cells superimposed on ^{12}C mass fraction resulting from the detonation evolved with the X14 network at 8 levels of grid refinement. Behind the triple-points the ^{12}C is depleted on a shorter distance behind the shock (white curve) relative to its depletion behind the weak incident shocks between the triple-points.

Table 5.1: Detonation cell sizes measured for simulations evolved with each of the four reaction networks at different levels of grid refinement.

Network	Refinement Level	Length (cm)	Width (cm)	Ratio
X14	6	33.4	15.9	2.1
	8	32.2	16.0	2.0
	10	13.7	6.7	2.0
X14+ap+an	6	32.6	16.0	2.0
	8	15.7	8.0	2.0
X150	6	17.2	8.1	2.1
	8	11.9	6.7	1.8
A13	6	32.0	16.0	2.0
	8	13.0	6.8	1.9
	10	12.7	6.6	1.9

Table 5.2: Burning Lengths calculated for detonations evolved with the Aprox13 network. The C-burning lengths were calculated analogously to 1D. The O-burning lengths were calculated by two methods: Method 1 is measured from the back of the numerical shock to the left-most coordinate where the ^{16}O mass fraction still has a value greater than or equal to 0.25 or 0.05 (50% or 90% of initial value), and Method 2 is measured from the average position of the shock to the coordinate where the ^{16}O mass fraction (averaged over y for a given x-coordinate) has been depleted by 50% or 90%.

Aprox13 Burning Lengths			Refinement Level 6	8	10
50% C	Min		0.147	0.109	0.029
	Max		0.778	0.445	0.528
	Avg		0.446	0.243	0.217
	1D		0.206	0.191	0.143
90% C	Min		0.634	0.365	0.245
	Max		1.645	1.382	1.239
	Avg		1.067	0.811	0.679
	1D		0.801	0.773	0.734
50% O	Method 1	Min	78.50	77.63	79.06
		Max	85.00	94.25	95.41
		Avg	81.02	86.51	89.31
	Method 2	Avg	79.19	81.31	79.10
	1D		79.02	79.15	79.11
90% O	Method 1	Min	290.0	286.8	294.8
		Max	294.5	302.9	295.2
		Avg	293.9	292.7	295.1
	Method 2	Avg	288.7	285.8	289.1
	1D		288.5	289.5	289.5

Table 5.3: Burning Lengths calculated for detonations evolved with the X14 network. The C-burning lengths were calculated analogously to 1D. The O-burning lengths were calculated by two methods: Method 1 is measured from the back of the numerical shock to the left-most coordinate where the ^{16}O mass fraction still has a value greater than or equal to 0.25 or 0.05 (50% or 90% of initial value), and Method 2 is measured from the average position of the shock to the coordinate where the ^{16}O mass fraction (averaged over y for a given x-coordinate) has been depleted by 50% or 90%.

X14 Burning Lengths			Refinement Level 6	8	10
50% C	Min		0.161	0.166	0.095
	Max		0.992	0.622	0.552
	Avg		0.696	0.406	0.337
	1D		0.370	0.313	0.301
90% C	Min		0.800	1.078	0.823
	Max		2.305	1.898	1.790
	Avg		1.723	1.560	1.419
	1D		1.487	1.602	1.584
50% O	Method 1	Min	170.0	168.4	167.4
		Max	175.0	196.6	173.4
		Avg	172.1	181.1	170.8
	Method 2	Avg	169.2	174.2	167.5
	1D		171.5	171.6	171.6
90% O	Method 1	Min	566.5	569.1	569.3
		Max	567.0	573.1	569.5
		Avg	567.0	570.3	569.4
	Method 2	Avg	520.2	559.2	522.5
	1D		565.1	565.0	565.1

Table 5.4: Burning Lengths calculated for detonations evolved with the X14+ap+an network. The C-burning lengths were calculated analogously to 1D. The O-burning lengths were calculated by two methods: Method 1 is measured from the back of the numerical shock to the left-most coordinate where the ^{16}O mass fraction still has a value greater than or equal to 0.25 or 0.05 (50% or 90% of initial value), and Method 2 is measured from the average position of the shock to the coordinate where the ^{16}O mass fraction (averaged over y for a given x-coordinate) has been depleted by 50% or 90%.

X14+ap+an Burning Lengths			Refinement Level 6	8	10
50% C	Min		0.162	0.080	-
	Max		0.876	0.480	-
	Avg		0.598	0.265	-
	1D		0.332	0.242	0.169
90% C	Min		0.667	0.357	-
	Max		1.898	1.355	-
	Avg		1.378	0.952	-
	1D		0.969	0.959	0.878
50% O	Method 1	Min	72.50	76.75	-
		Max	84.50	89.75	-
		Avg	76.01	82.43	-
	Method 2	Avg	73.98	80.43	-
	1D		74.41	74.39	74.30
90% O	Method 1	Min	306.5	299.3	-
		Max	312.0	311.4	-
		Avg	307.5	307.5	-
	Method 2	Avg	302.0	301.4	-
	1D		301.0	302.1	302.1

Table 5.5: Burning Lengths calculated for detonations evolved with the X150 network. The C-burning lengths were calculated analogously to 1D. The O-burning lengths were calculated by two methods: Method 1 is measured from the back of the numerical shock to the left-most coordinate where the ^{16}O mass fraction still has a value greater than or equal to 0.25 or 0.05 (50% or 90% of initial value), and Method 2 is measured from the average position of the shock to the coordinate where the ^{16}O mass fraction (averaged over y for a given x-coordinate) has been depleted by 50% or 90%.

X150 Burning Lengths			Refinement Level 6	8	10
50% C	Min		0.219	0.042	-
	Max		0.666	0.835	-
	Avg		0.401	0.315	-
	1D		0.288	0.263	0.204
90% C	Min		0.820	0.183	-
	Max		1.314	1.225	-
	Avg		1.027	0.700	-
	1D		0.923	0.866	0.813
50% O	Method 1	Min	19.50	19.00	-
		Max	23.00	26.13	-
		Avg	20.90	22.05	-
	Method 2	Avg	20.23	17.20	-
	1D		21.67	21.80	21.70
90% O	Method 1	Min	63.50	60.63	-
		Max	67.00	77.88	-
		Avg	66.04	67.68	-
	Method 2	Avg	66.23	61.70	-
	1D		66.21	66.94	66.76

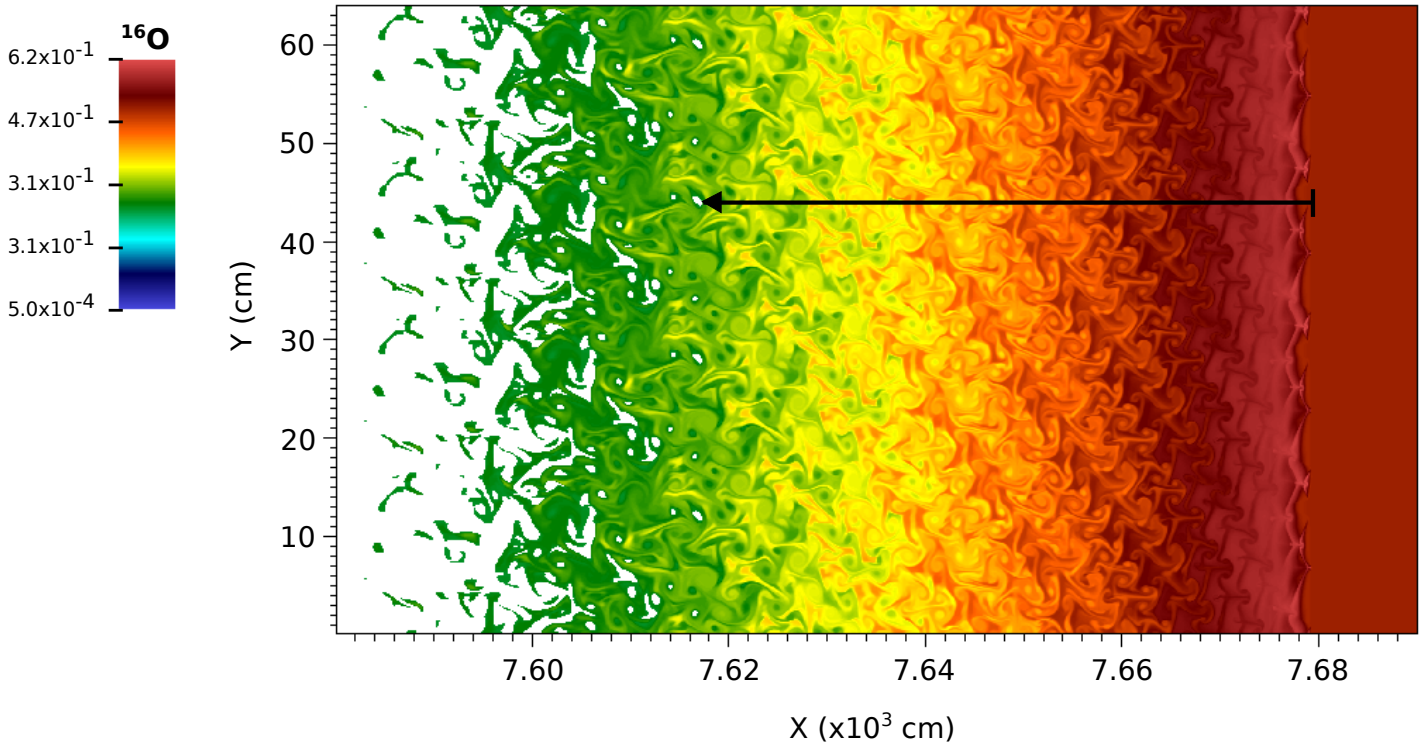


Figure 5.8: ^{16}O mass fraction (only plotted for values of 0.25 and higher) resulting from the simulation evolved with the Aprox13 network at 10 levels of grid refinement. The black arrow represents a possible 1D sample taken in order to calculate the 50% O-burning length. If burning lengths are measured analogously to 1D, then such a sample that terminates at an unrepresentative pocket of over-reacted fluid could influence results

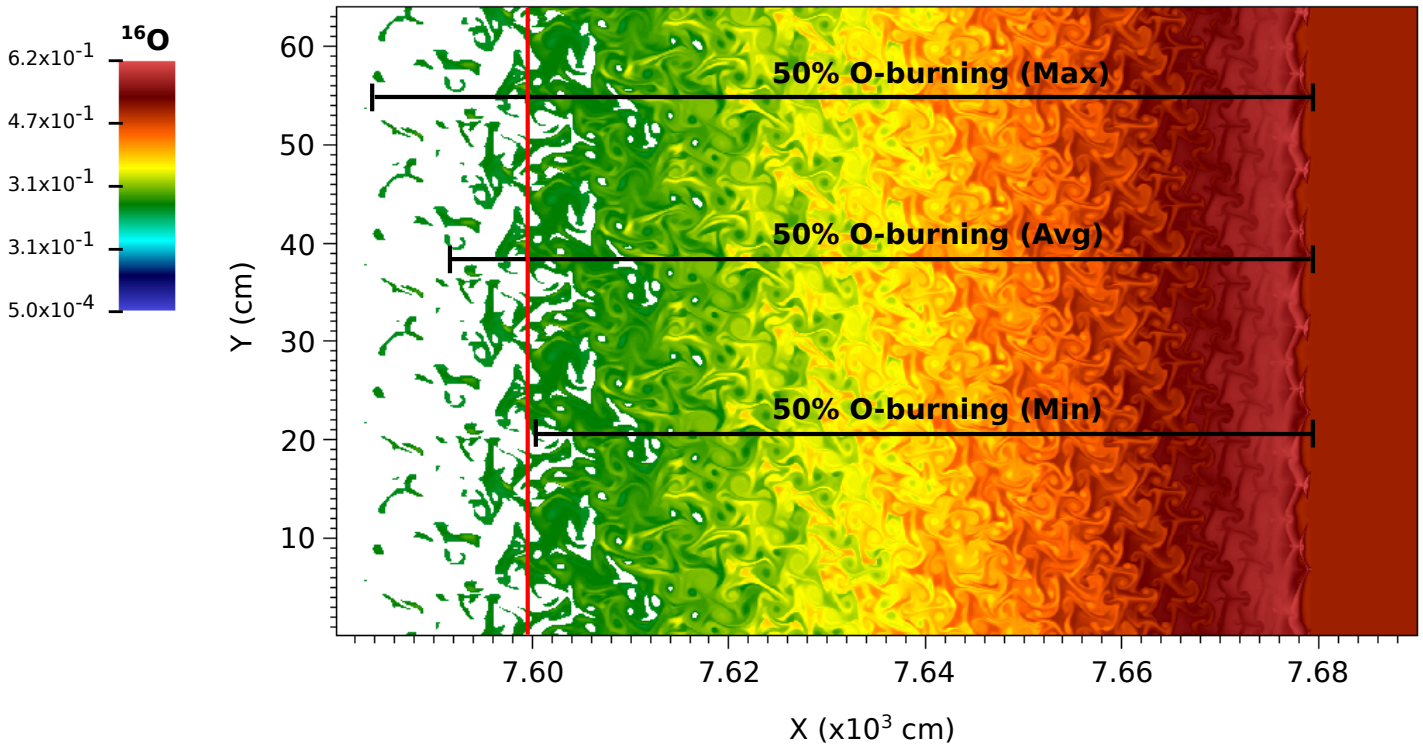


Figure 5.9: Same as Figure 5.8 but showing the two methods used to calculate O-burning lengths. In method 1 (black lines showing the minimum, maximum, and average values), we measured from the back of the numerical shock to the left-most coordinate where the ^{16}O mass fraction was still 0.25 or higher. In method 2, we measured from the average shock location to the coordinate where the y-average of ^{16}O is 0.25.

Next, we will examine the detonation velocities of the cellular burning fronts and compare them with our 1D results. These velocities were calculated by recording the time and position of the shock as it moved across the domain. Figure 5.10 shows the results of these calculations for the X14 network along with the 1D equivalent at 10 levels of grid refinement. These 2D velocities track the 1D results quite well on average, even at the coarsest resolution. This does not seem surprising however because the energy that is released in the reaction zone should be essentially the same when accounting for the extra dimension in the 2D simulation. This reasoning is supported by the data in Figure 5.11 which shows a comparison of the total energy generation rate (integrated over the grid) versus simulation time for the same 1D and 2D detonations shown in Figure 5.10. The additional energy release in the 2D simulation has been removed by dividing by the 128-cm extent of the y-dimension. So, even though the distribution of energy generation is different in 2D versus 1D due to cellular burning, the total amount of energy delivered to the region in sonic contact with the front (and therefore available to drive the detonation) is the same. For a 2D pathological detonation that is unsupported, where a sonic surface is located within the reaction zone, this reasoning would have to be modified. In this case, unreacted pockets of fuel (created by interactions of triple-points at the front) could survive beyond the sonic surface, therefore reducing the amount of energy available to drive the detonation and slightly reducing its velocity relative to 1D. In addition to the cellular structure itself, the resolution can also alter the distribution of energy release at and behind the front. But again, the same total amount of energy is added to the fluid, and because the entire reaction zone is in sonic contact with the front, the detonation velocity is not affected. This same behavior is observed for all four of the networks that we considered.

5.2 3D

In this section we show the preliminary results from a 3D detonation tube. Currently, this simulation has not evolved far enough to make meaningful measurements of the detonation cells or burning lengths ($\sim 2\times10^{-7}$ s). Figures 5.12 and 5.13 show the current state of this

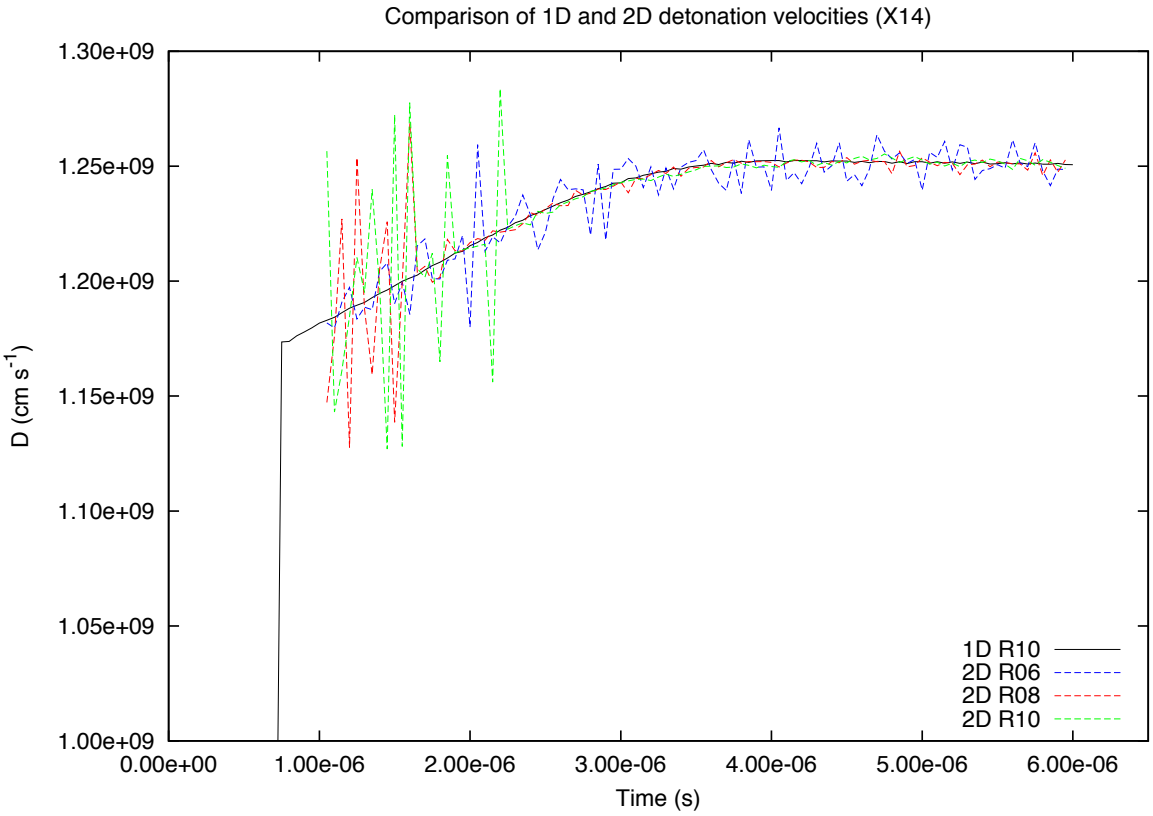


Figure 5.10: Plot of the detonation velocities versus time for the 2D results evolved with the X14 network at three levels of grid refinement. The 1D result at 10 levels of grid refinement is also shown for comparison.

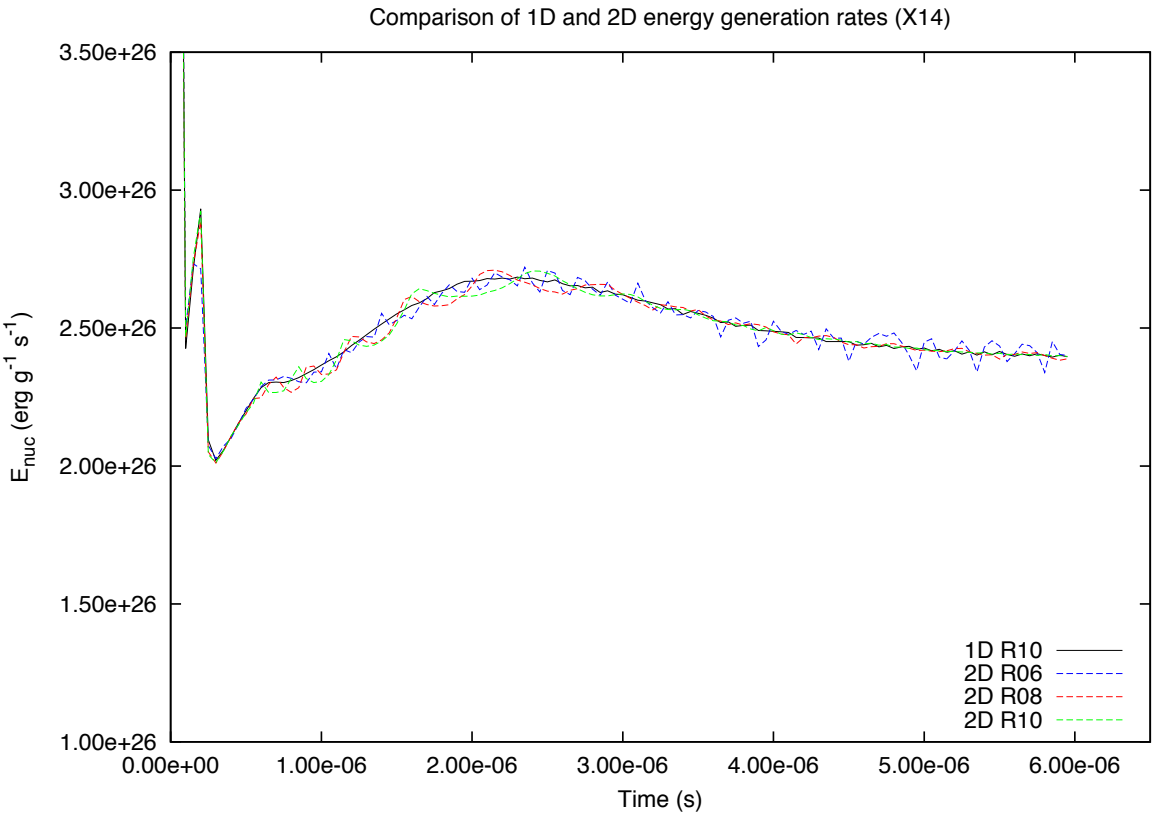


Figure 5.11: Plot of the total nuclear energy generation integrated over the grid versus time for the 2D results evolved with the X14 network at three levels of grid refinement. The 1D result at 10 levels of grid refinement is also shown for comparison. The 2D values have been divided by 128 to account for the extra 128-cm extent of fluid that was burned relative to 1D. This data shows that although the distribution of energy release is different in 1D versus 2D, and at different levels of grid refinement, the total energy that is released is roughly the same.

simulation in the ^{16}O and ^{28}Si mass fractions. From this simulation, we are interested in how the cellular features might be altered relative to our 2D results. For example, the detonation cells will not trace out "flat" diamond shapes but will instead enclose 3D diamond-shaped volumes. The size of these cells might differ from 2D due to triple-points interacting across a detonation front described by a surface rather than a line. In addition, the well-known differences between turbulent cascades in 2D and 3D can alter the mixing within the reaction zone which might cause differences in the elongated burning lengths.

5.3 Conclusions

In this chapter, we have shown that both resolution and nuclear network size can affect the cellular burning features of multi-D C/O detonations. As resolution was improved, the detonation cells measured for all networks became more irregular and appeared to converge in size. The sizes and degree of irregularity of the cells also seem to be dependent on the size of the network used to evolve the detonations. Because of this irregularity, as well as the limited resolution used for the larger networks, it is difficult to discern the nature of this relationship. The length-to-width ratios of these cells were shown to be similar as measured for all networks, but there appears to be a trend toward slightly smaller ratios as network size is increased. In addition, the triple-points (which trace the path of these detonation cells) were clearly affected by network size, with stronger triple-points observed for the larger networks. Due to multi-D effects, the definition of a burning length is unclear. However, the effective region where a particular mass fraction is diminished everywhere by a certain amount is increased relative to the 1D burning lengths. These elongated burning regions are caused by burning under various thermodynamic conditions at the front as well as burning among extensive mixing in the following flow. Regardless of the method by which the burning lengths are measured, they are all subject to the same dependence on network size as described in 1D (due to the particular reactions available to each network). Also similar to 1D, the C-burning lengths converged in size as resolution was improved, whereas

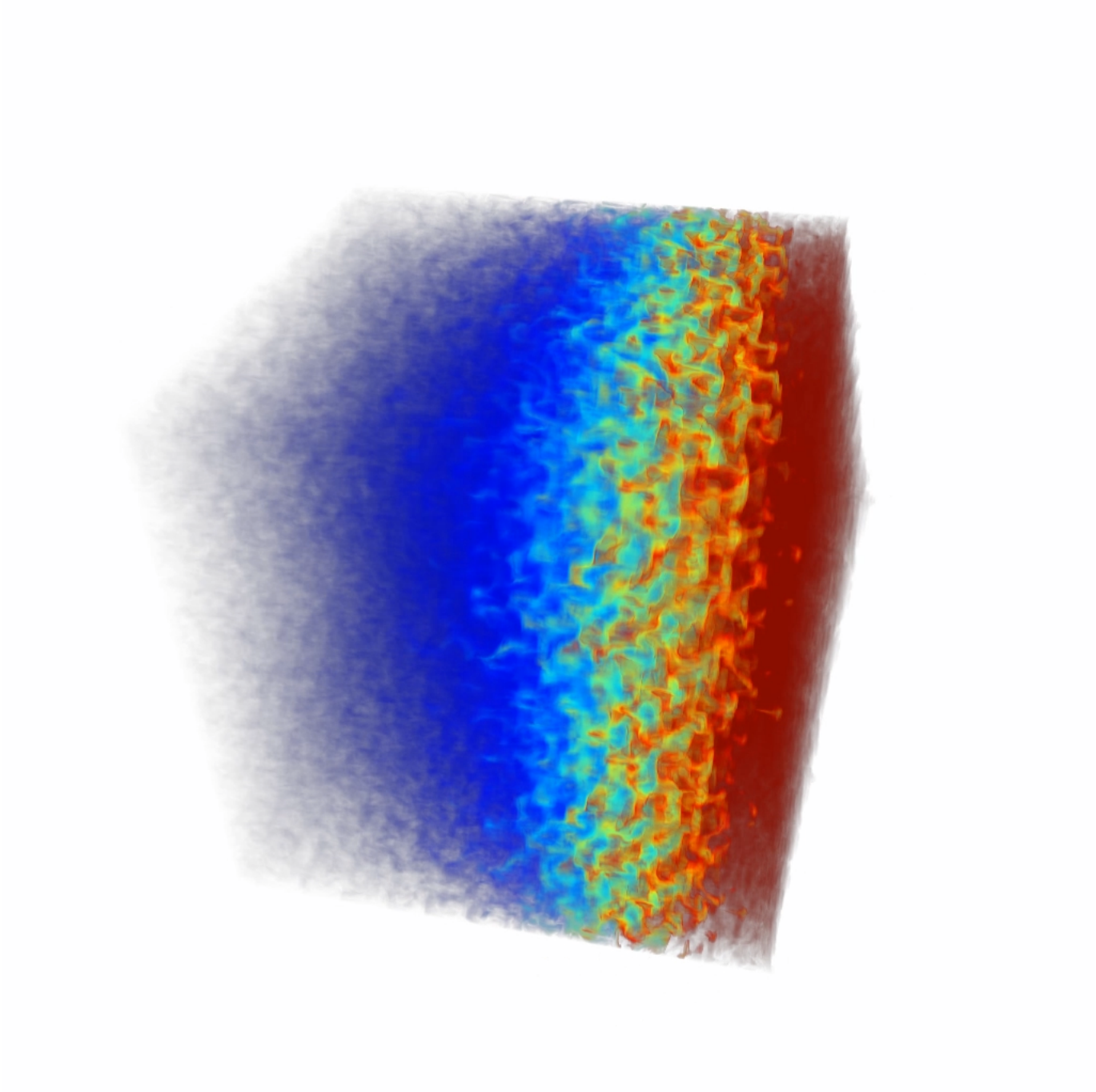


Figure 5.12: Plot of the ^{16}O mass fraction resulting from an unsupported 3D detonation evolved with the Aprox13 network at 8 levels of grid resolution ($5{\times}10^7$ g cm^{-3}).

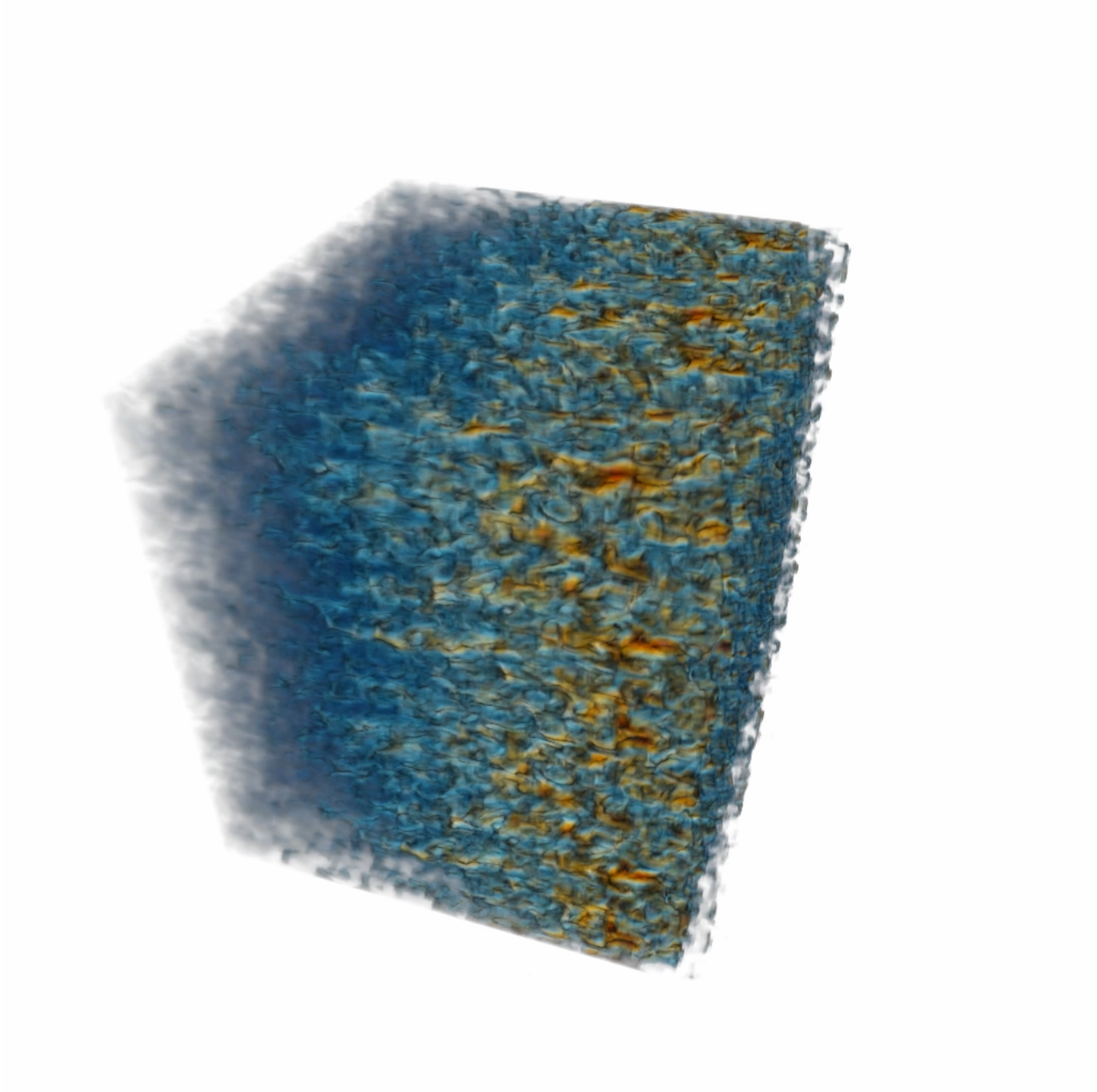


Figure 5.13: Plot of the ^{28}Si mass fraction resulting from an unsupported 3D detonation evolved with the Aprox13 network at 8 levels of grid resolution ($5{\times}10^7$ g cm^{-3}).

the O-burning lengths were resolved at all resolutions that we considered. The detonation velocities measured for a given network in 2D were essentially the same as those found in 1D. This makes sense when considering that the total energy released behind the front was the same in 1D and 2D (when accounting for the extent of the extra spatial dimension in 2D); because the detonations are of the CJ type, the same amount of energy was available to drive the detonations. These 2D detonation velocities also showed no dependence on grid resolution.

From these results, we conclude that although the effective burning region of a particular fuel is increased due to multi-D considerations, this increase is small relative to the effects that using a larger network can have on the burning lengths. This does not mean that the multi-D effects are unimportant. It is still true that when simulating full-star explosions where approximate burning models are used, those models that include the effects of cellular burning (e.g. increased burning lengths) can result in different isotopic yields (from incomplete burning in low-density environments) relative to those that do not include these effects. The changes in burning lengths due to the use of larger reaction networks simply gives a more realistic benchmark from which to measure the multi-D effects.

Chapter 6

Double-Detonations in Confined He-Belts

Given the differences we observe in detonation propagation as a function of network size, we will apply our new network technology to an astrophysical situation. SN2014J was the closest Type Ia supernova in decades at a distance of 3.5 Mpc. Located within the nearby M82 galaxy, its close proximity allowed the most detailed gamma-ray observations of a SNe Ia to date. By most standards it was a "normal" Type Ia event, both spectroscopically and photometrically. However, early-time gamma-ray observations by Diehl et al. (2014) showed the presence of *low-velocity* ^{56}Ni in the *outer regions* of the ejecta (But, the late-time gamma-ray data show no compelling evidence for prominent velocity substructure as measured by Churazov et al. (2015)). These characteristics stand out as peculiar because IGEs (including ^{56}Ni) are not normally strong features in early-time SNe Ia observations due to being confined to the inner regions of the remnant (see Chapter 1). Additionally, the matter in the outer ejecta is known to have high velocities, so the presence of low-velocity ^{56}Ni is indeed strange in these regions. In order to explain the observations, Diehl et al. (2014) considered a modified version of the double-detonation scenario (Section 1.3.3), where a detonation in an equatorial He-belt, rather than a He-shell, gives rise to the secondary C/O detonation. They proposed that, if viewed along one of the poles, this model could result in

observations of low-velocity ^{56}Ni in the outer ejecta by constraining the velocities of the ^{56}Ni (produced during the He-detonation) to directions mostly perpendicular to our line of sight (see Figure 6.1). So, although this ^{56}Ni does, in fact, have high velocities like the rest of the matter at the same radius, only a small component of its velocity is in our line of sight, and it is the line-of-sight velocities that we can infer from the spectra of such distant objects.

6.1 Simulations

We performed 2D axisymmetric simulations of this explosion scenario in order to explore its ability to produce the early-time ^{56}Ni-features observed in SN2014J. For most simulations we used a 13-species (Aprox13) nuclear reaction network, but taking advantage of our custom version of FLASH, we also revisited two of the simulations using a 150-species network (implemented with XNet; Hix and Thielemann (1999)) to see how improved nuclear kinetics might affect the results. We set up our models in two different ways. In one approach, we ignited a detonation in an equatorial belt of He surrounding a C/O WD. If successful, these He-detonations transitioned directly into C-detonations at the He-C/O interface, processing the entire object into heavier elements. The other approach we took was to assume that a detonation had already occurred in a He-belt and that the He was burned to pure ^{56}Ni before the core was detonated. For these models we started with an equatorial belt of ^{56}Ni surrounding a C/O WD and ignited a detonation at its center.

Our progenitor models were created by first generating 1D density and pressure profiles for a WD[1] with a central density of 5×10^7 g cm^{-3} (Figures 6.2 and 6.3). WDs with central densities of 2.5×10^7 and 7.5×10^7 g cm^{-3} were tried as well but these models produced too little ($\sim$0.3 M$_\odot$) or too much ($\sim$0.9 M$_\odot$) ^{56}Ni in the core, in disagreement with the $\sim$0.6 M$_\odot$ of ^{56}Ni inferred for SN2014J. We then mapped these 1D profiles into FLASH as our initial conditions and used the equation of state to calculate the temperature. All progenitors were given a homogeneous 50-50 C/O composition. The belts were created by replacing a "plug"

[1]These WD profiles were generated using publicly available software from Frank Timmes' cococubed website (http://cococubed.asu.edu)

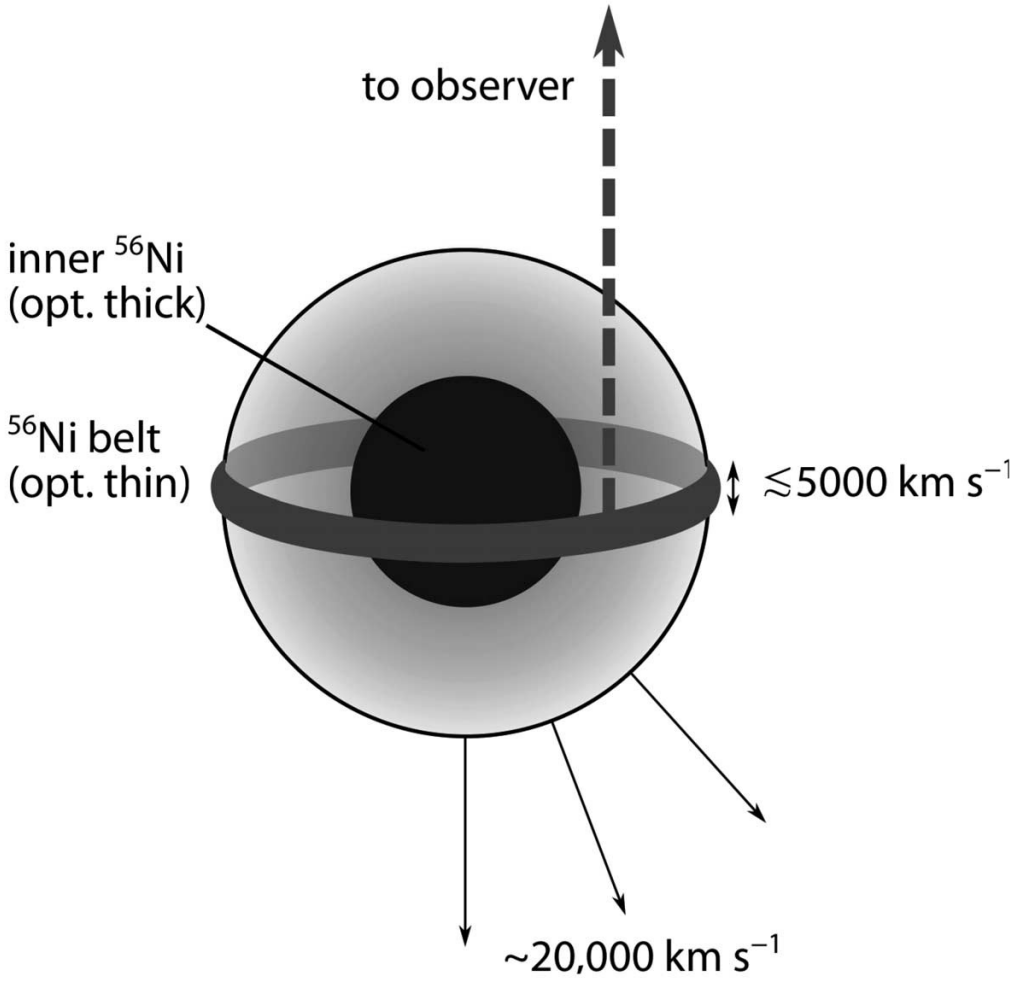


Figure 6.1: Explosion scenario proposed by Diehl et al. (2014). The ^{56}Ni produced during the He-belt detonation has large velocities like the rest of the matter in the outer ejecta, but its component in the line-of-sight of the observer is small because it is confined to an equatorial belt.

of C/O in the outer region of the WDs with either pure ^{4}He or ^{56}Ni. Due to the axisymmetry, this is equivalent to a "belt" of material (Figure 6.4). The belts were embedded within the WD in order to minimize spreading of the belt material while the initial detonations were ignited. We used both constant-density belts as well as belts whose densities followed the underlying WD profile. The constant-density belts were embedded in the outer edge of the WD to a depth where their constant densities matched with the corresponding density contour within the WD (e.g. a belt with a constant density of $2{\times}10^{6}$ g cm^{-3} would sit atop the $2{\times}10^{6}$ g cm^{-3} contour within the WD; see Figure 6.5). The width is then set to result in a desired total mass for the belt. The belts with stratified densities were given the same geometries as their constant-density counterparts but their density falls off with the WD profile. The background fluid for all simulations was given a C/O composition with a density and temperature of $1{\times}10^{-3}$ g cm^{-3} and $3{\times}10^{7}$ K, respectively.

He-Belt Models

The He-belt models consisted of eight constant-density belts and six belts with stratified densities (Table 6.1). The two models marked with X150 used the 150-species network in place of the 13-species alpha-chain. The temperature of all He-belts was set to 3×10^{7} K and the hotspots used to ignite detonations in this He were given a radius of 75 km and a temperature of $5{\times}10^{8}$ K. These hotspots were placed above the He-C/O interface at heights of 25% and 10% of the belt thickness for the constant-density and stratified-density belts, respectively. In addition, some of the He-belts were given a crescent shape in order to test a different (perhaps more realistic) geometry. The crescent shapes were constructed by creating a hypothetical circle with $3{\times}$ the radius of the WD and offsetting it in the negative x-direction until its edge is at the desired density contour of the WD (Figure 6.6). Then the crescent-shaped region of the WD with no overlap between the two circles is filled with He.

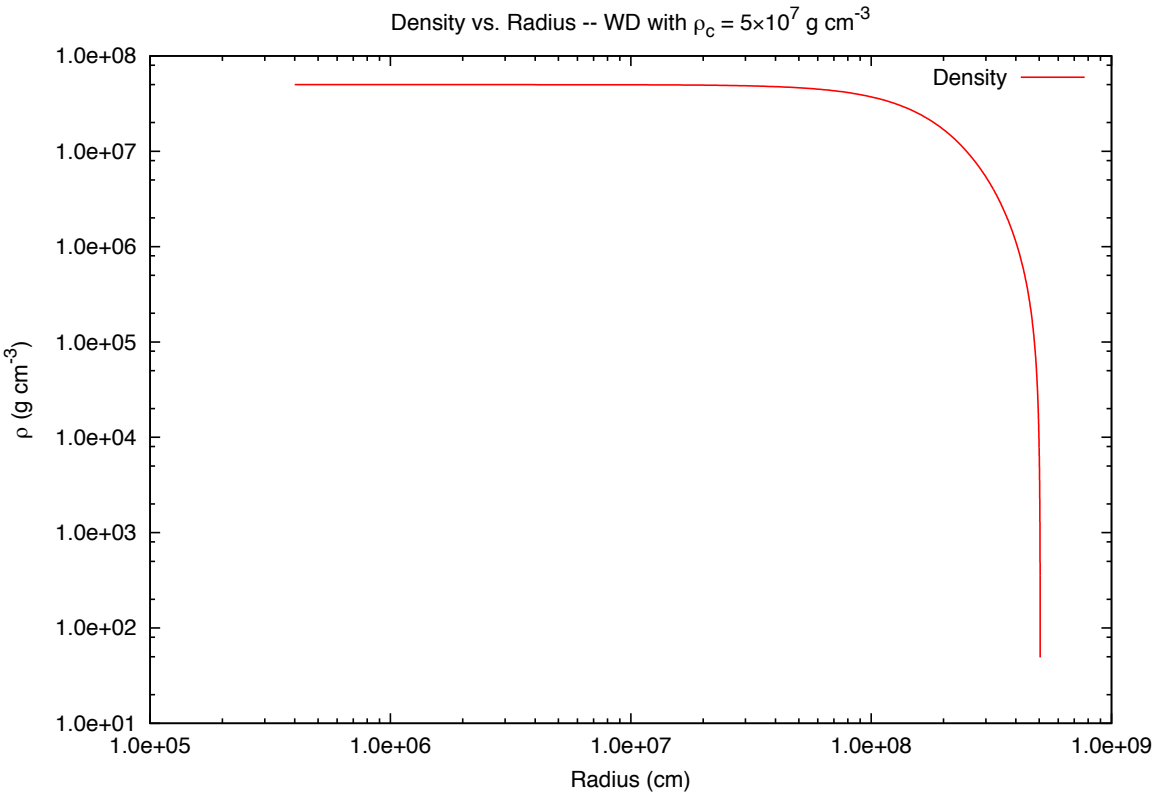


Figure 6.2: Log-Log plot of density vs radius for a WD with central density of 5×10^7 g cm^{-3}

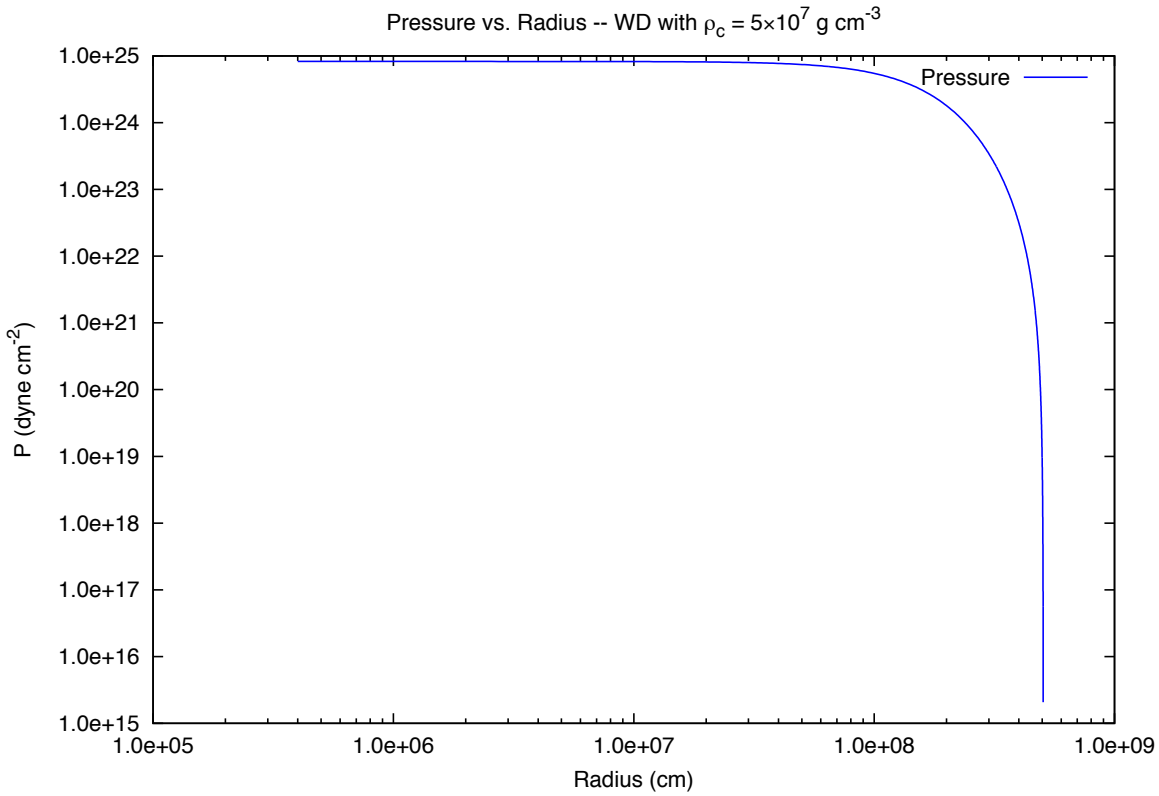


Figure 6.3: Log-Log plot of pressure vs radius for a WD with central density of 5×10^7 g cm^{-3}

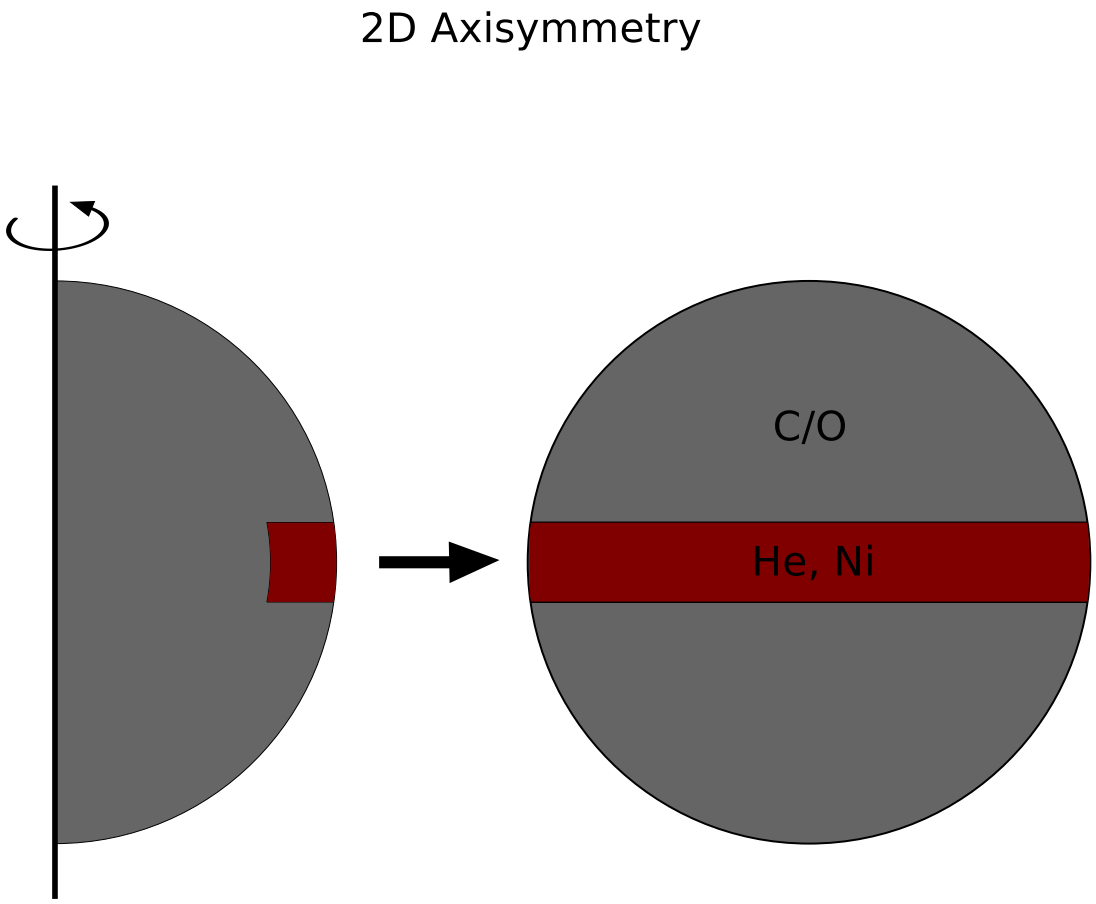


Figure 6.4: In order to represent a belt of He or Ni around the WD, it is only necessary to insert a "plug" of matter due to the 2D axisymmetry.

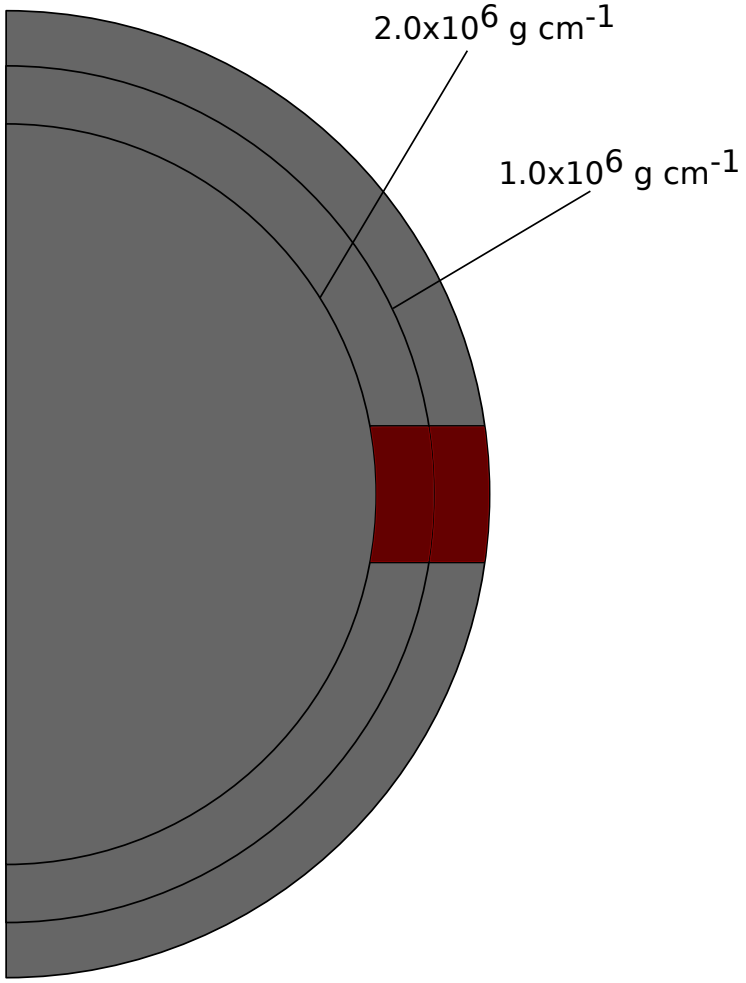


Figure 6.5: The red region represents a "belt" of He or Ni with a density of 2×10^6 g cm^{-3}. It is embedded into the WD until it reaches the density contour with the same value.

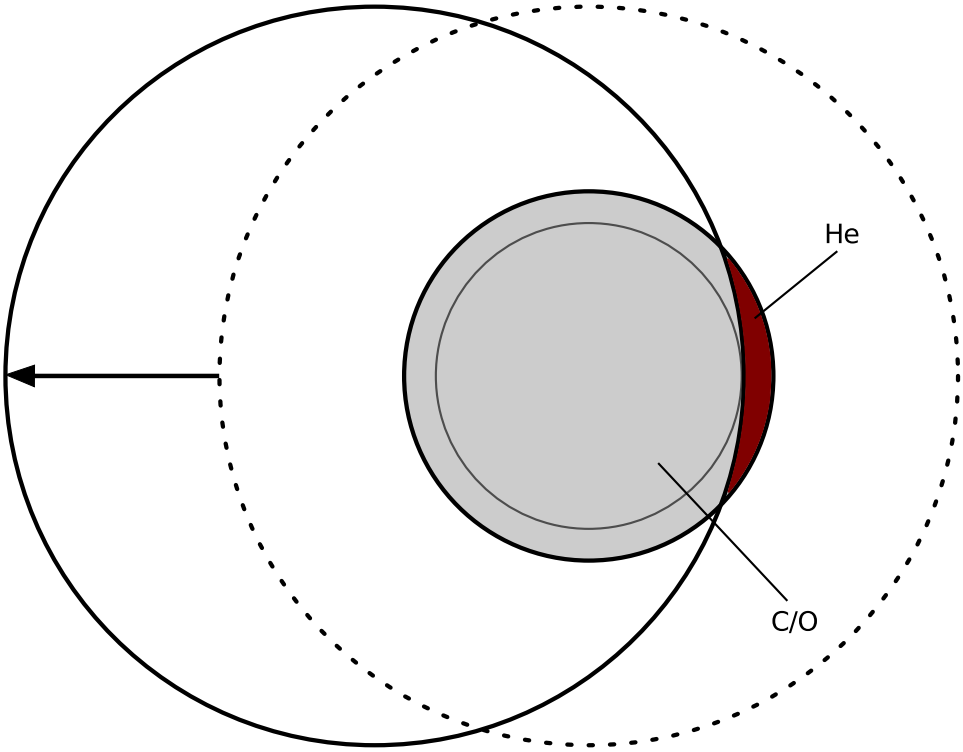


Figure 6.6: The crescent-shaped belts were created by using a hypothetical circle 3x the radius of the WD and offsetting it in the negative x-direction until its edge meets the desired density contour of the WD. The region of the WD that does not overlap with the larger circle is then filled with He.

Table 6.1: Results from He-belt simulations. Masses, densities, and kinetic energies are in units of $M_\odot$, 10^6 g cm^{-3}, and 10^{51} ergs, respectively. The FWHM defines a velocity range with units of km s^{-1}. The subscripts b and c stand for core and belt, respectively.

Belt Description	M_b	$\rho_{6,b}$	$M_{Ni,c}$	$M_{Ni,b}$	M_{Si}	M_{IME}	E_k	FWHM	Model
Crescent	0.041	Follow WD ρ (2.0)	0.534	0.017	0.237	0.412	1.131	9100	He-K
	0.034	Follow WD ρ (1.75)	0.533	0.012	0.239	0.415	1.105	8200	He-L
	0.034	Follow WD ρ (1.75) X150	0.558	0.008	0.202	0.371	1.103	7600	He-L-150
Gradient	0.030	Follow WD ρ (2.0)	0.538	0.0164	0.228	0.401	1.115	7100	He-I
	0.030	Follow WD ρ (2.5)	0.540	0.0185	0.228	0.400	1.126	7300	He-J
	0.030	Follow WD ρ (2.5) X150	0.561	0.015	0.198	0.365	1.128	7800	He-J-150
Constant	0.075	1.0	0.589	0.0342	0.207	0.366	1.135	10200	He-A
		1.5	0.543	0.0482	0.237	0.414	1.190	11800	He-B
		2.0	0.541	0.0544	0.239	0.416	1.212	12100	He-C
		2.5	0.538	0.0578	0.243	0.422	1.226	11900	He-D
	0.1	1.0	0.612	0.0478	0.196	0.345	1.161	11100	He-E
		1.5	0.551	0.0660	0.234	0.410	1.235	11600	He-F
		2.0	0.546	0.0729	0.239	0.416	1.259	12900	He-G
		2.5	0.547	0.0788	0.240	0.419	1.281	12800	He-H

Ni-Belt Models

The Ni-belt models consisted of two constant-density belts and two belts with stratified densities (Table 6.2). One of the stratified belts was given 3× the value of the underlying WD density to see how increased density (caused by burning the He to Ni) might affect the results. Both the constant-density and stratified-density Ni-belts were given a temperature of T = 1×10^8 K. The hotspots used to ignite the C-detonations were given a temperature of 3×10^9 K , a radius of 75 km, and were initiated at the center of the C/O cores.

6.2 Results

In order to compare the results of our simulations with observations of SN2014J, we looked for general agreement with the peculiar ^{56}Ni features as well as indication of a normal Type Ia SNe. Diehl et al. (2014) estimated the presence of ∼0.06 $M_\odot$ of ^{56}Ni in the outer ejecta with velocities that were $\lesssim$ 2500 km s^{-1}, so we used these two values as indicators of the ^{56}Ni features. The total mass of the ^{56}Ni produced by the He-detonations was calculated directly (Figure 6.7), and this mass was separated into line-of-sight velocity bins in order to create histograms illustrating its distribution with line-of-sight velocities. We used the full-width at half-maximum (FWHM) of these histograms as a common measure of the range in velocities for each of our models. In addition, we calculated the core-^{56}Ni masses, total IME masses, and explosion energies to ensure that these characteristics were in line with normal SNe Ia.

6.2.1 He-Belts

Our first models consisted of detonations in the crescent-shaped He-belts with stratified densities. These simulations (models He-K and He-L in Table 6.1) represented our most realstic approach. Both simulations resulted in He-detonations that successfully transitioned into edge-lit detonations of the underlying C/O WD. Table 6.1 shows that both simulations produced core-^{56}Ni masses, total IME masses, and explosion energies that correspond to normal Type Ia events (see Chapter 1). However, neither model produced enough ^{56}Ni during

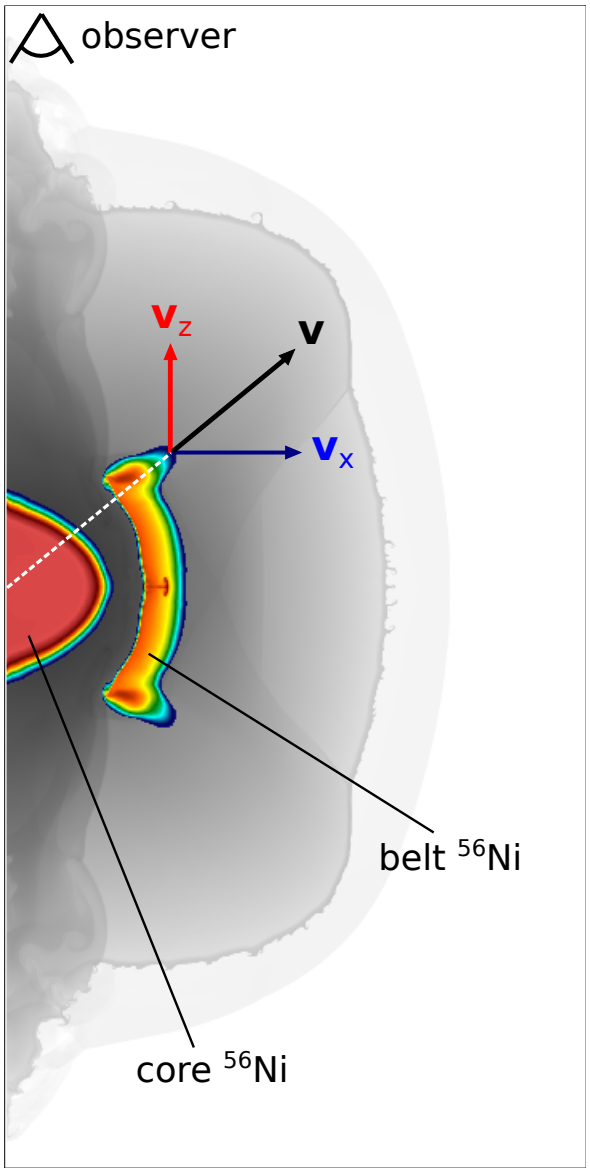


Figure 6.7: Results from a typical simulation. Density is plotted in gray-scale and ^{56}Ni is pictured in the rainbow color scheme. The total mass of ^{56}Ni synthesized in the belt is calculated and this mass is separated into line-of-sight velocity bins to create histograms of its distribution.

Table 6.2: Results from Ni-belt simulations. Masses, densities, and kinetic energies are in units of $M_\odot$, 10^6 g cm^{-3}, and 10^{51} ergs, respectively. The FWHM defines a velocity range with units of km s^{-1}. The subscripts b and c stand for core and belt, respectively.

Belt Description	M_b	$\rho_{6,b}$	$M_{Ni,c}$	M_{Si}	M_{IME}	E_k	FWHM	Model
Gradient	0.023	Follow WD ρ (2.0)	0.561	0.240	0.421	1.127	2100	Ni-C
	0.068	3x WD ρ (2.0)	0.561	0.242	0.427	1.110	700	Ni-D
Constant	0.075	2.0	0.589	0.207	0.366	1.135	1800	Ni-A
	0.1	2.5	0.543	0.237	0.414	1.190	1700	Ni-B

the He-detonations to be consistent with observations, and the belt-^{56}Ni that was produced had line-of-sight velocities that were too large. Figure 6.8 shows the results from model He-K. The belt-^{56}Ni has been noticably spread out by the explosion and the distribution of this ^{56}Ni with line-of-sight velocity is shown in Figure 6.9. The FWHM encloses a velocity range up to $\sim$9000 km s^{-1}, well above the $\sim$2500 km s^{-1} velocity range inferred by Diehl et al. (2014). From Table 6.1, it should be obvious that these models were unable to synthesize enough belt-^{56}Ni because they did not contain enough initial He in their belts. In order for them to have an adequate amount of He, we would have needed to embedded the crescent belts further into the WD or change their geometries to make them wrap further toward the poles. Both of these considerations would have led to more ^{56}Ni, however they would have also led to more of this ^{56}Ni with line-of-sight velocites that were too large, in essence, trading one ruinous result for another.

In order to reduce the line-of-sight velocities imparted to the belt-^{56}Ni, we next modeled He-belts with stratified densities that were geometrically confined near the equator (models He-I and He-J in Table 6.1). We speculate that the confinement of these belts might be realized due to rotation or magnetic fields, although our means of providing this confinement was purely geometrical. Both of these models resulted in successful edge-lit double-detonations and produced isotopic yields and energetics in agreement with normal SNe Ia (Table 6.1). Using these confined belts did slightly reduce the line-of-sight velocities of the belt-^{56}Ni, but the values still remained too high, above $\sim$7,000 km s^{-1}. In addition, like the crescent belts, we were unable to add enough He to produce the amount of ^{56}Ni observed by Diehl et al. (2014). Increasing the amount of He by embedding the belts even deeper inside the WD becomes unrealistic, and adding He by increasing the width of the belts only further stymies our attempt to constrain the line-of-sight velocities of the Ni. Figure 6.10 shows the results from model He-I, illustrating the spread of belt-^{56}Ni that leads to the large line-of-sight velocity range of this Ni shown in Figure 6.11.

In an attempt to increase the amount of ^{56}Ni produced by the He-detonations, we next used confined He-belts with constant densities. The total mass of He in the belts was either

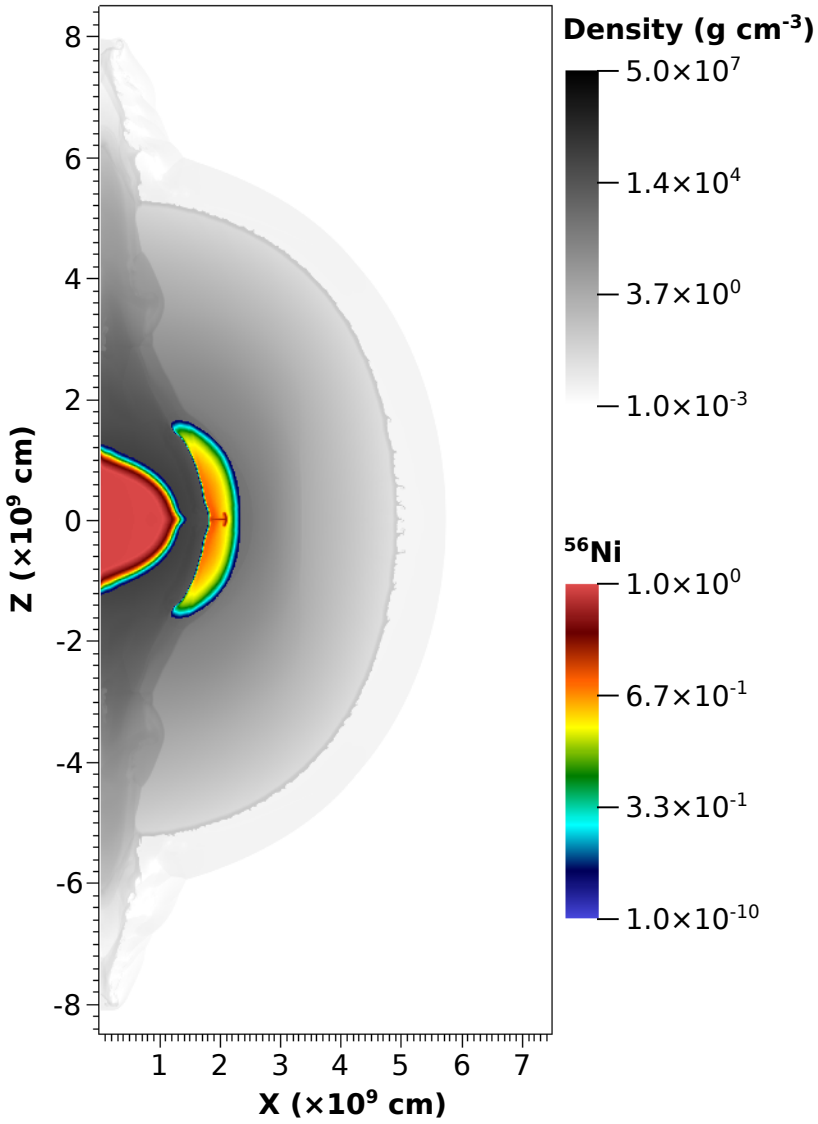


Figure 6.8: Results from model He-K. A detonation in the crescent-shaped He-belt produces a belt of ^{56}Ni with a similar shape, which reaches far from the equatorial region.

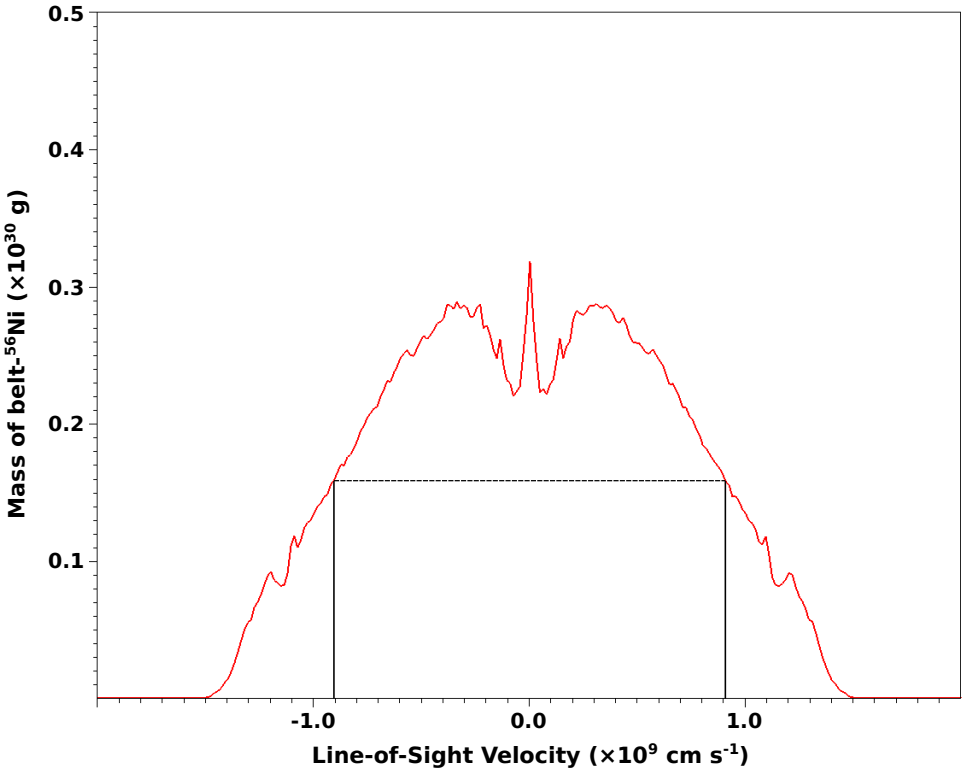


Figure 6.9: Results from model He-K. The FWHM shows that most of the belt-^{56}Ni has line-of-sight velocities below $\sim$9000 km s^{-1}.

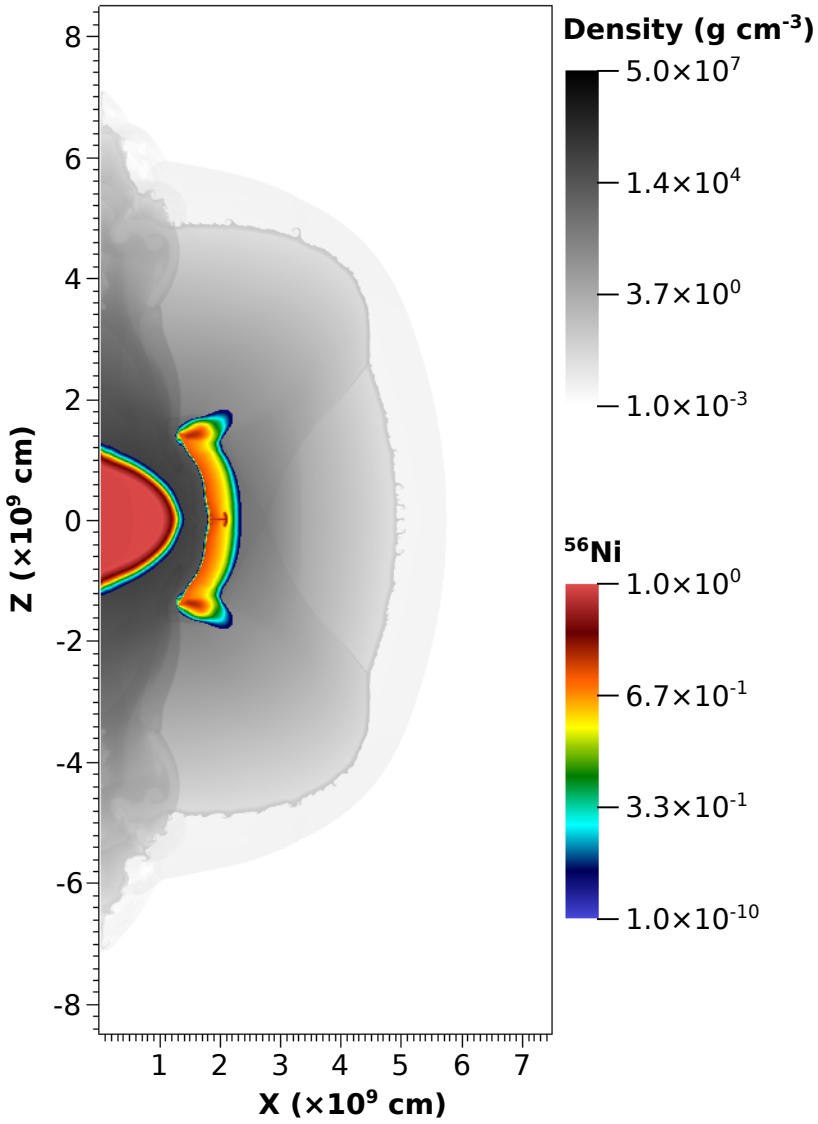


Figure 6.10: Results from model He-I. Even with a geometrically confined belt, the He-detonation spreads the resulting ^{56}Ni far from the equator.

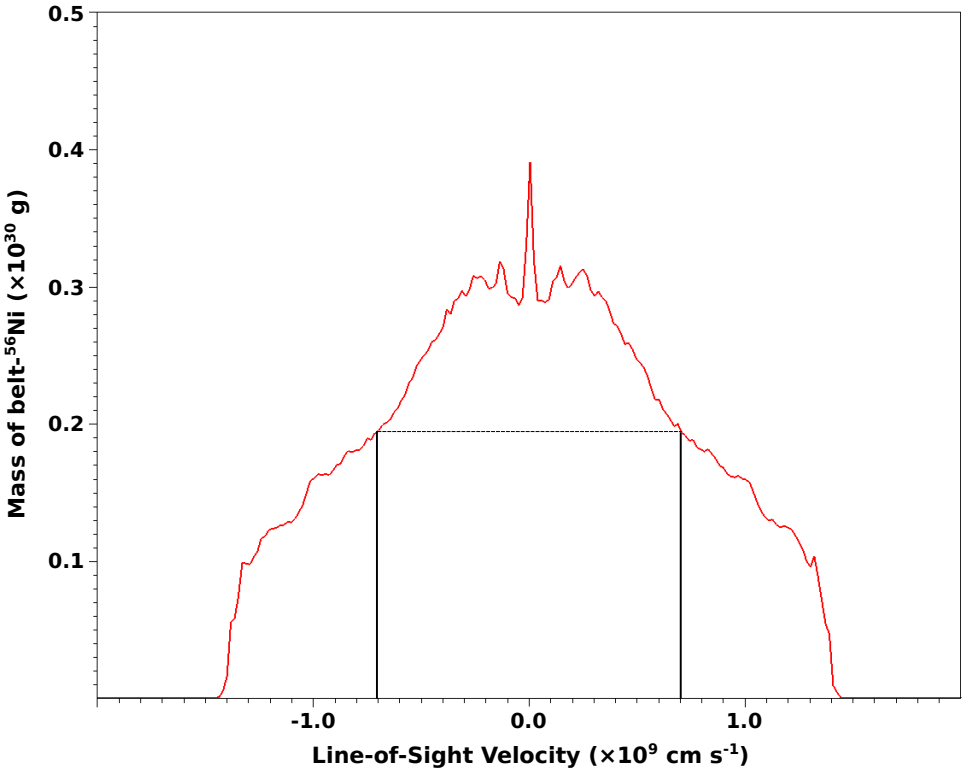


Figure 6.11: Results from model He-I. The FWHM shows that most of the belt ^{56}Ni has line-of-sight velocities below $\sim$7000 km s^{-1}.

0.075 $M_\odot$ or 0.1 $M_\odot$, and the constant densities were 1.0, 1.5, 2.0, or 2.5×10^6 g cm^{-3} (Table 6.1). Like the previous models, these simulations resulted in successful double-detonations and characteristics that agree with normal Type Ia events. By increasing the amount of He in the belts, many of these He-detonations were able to synthesize between 0.05-0.08 $M_\odot$ of ^{56}Ni, in agreement with Diehl et al. (2014). However, the line-of-sight velocities of the ^{56}Ni were much too large in all cases. Figure 6.12 shows the results from model He-C, where the belt-^{56}Ni has been spread far from the equator, giving it large line-of-sight velocities in excess of 12,000 km s^{-1} as seen in Figure 6.13. So it seems that any attempt to produce a sufficient amount of belt-^{56}Ni results in further discrepancies with the observed line-of-sight velocities.

Improved Nuclear Kinetics

Using a larger nuclear reaction network can alter the production of IGEs (and potentially the amount and distribution of ^{56}Ni) relative to reduced networks and more accurately captures the nuclear energy released in the process. So we re-ran two of our simulations using a 150-species network (marked with X150 in Table 6.1) in place of the 13-species network that was used for all other runs in order to see how this might affect our results. It is important to note that the 13 alpha-chain species (shown in red in Figure 6.14) are only connected through (α,γ)-links and heavy-ion reactions between C and O. Whereas, the large network (sum of all red and blue squares in Figure 6.14) follows 150 species and includes all of the reactions that link them. This means that there are many more reaction pathways available as the C/O fuel is processed into heavier elements when using the large network, and this can impact the final abundances as we will see.

Figure 6.18 shows a time sequence comparing models He-K and He-K-X150. Both simulations were given a confined He-belt with stratified density that started at 2.5×10^6 g cm^{-3} and fell off with the WD density. The only difference between these models is that He-K used the 13-species network while He-K-X150 used the 150-species network. In addition to the density and ^{56}Ni mass fractions shown in the previous figures, the mass

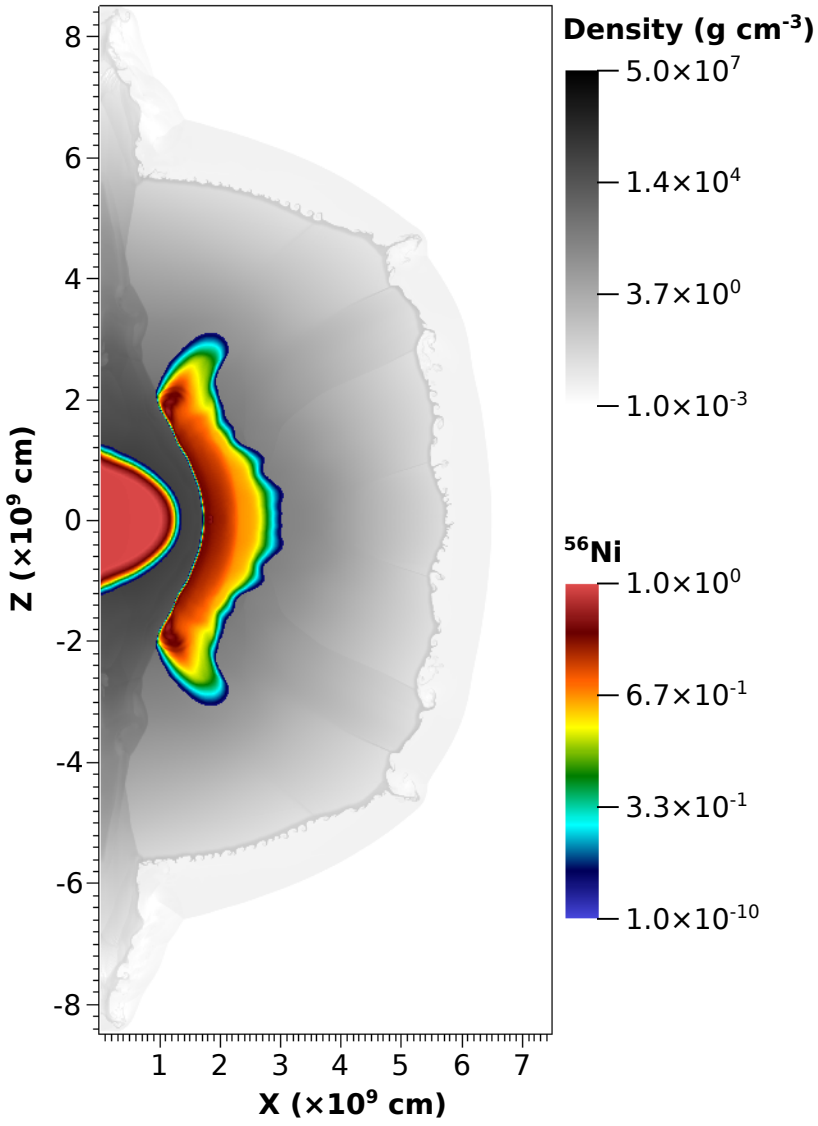


Figure 6.12: Results from model He-C. Detonations in this geometrically confined, constant-density He-belt produces more ^{56}Ni than its stratified-density counterpart, but the ^{56}Ni is spread even further from the equator.

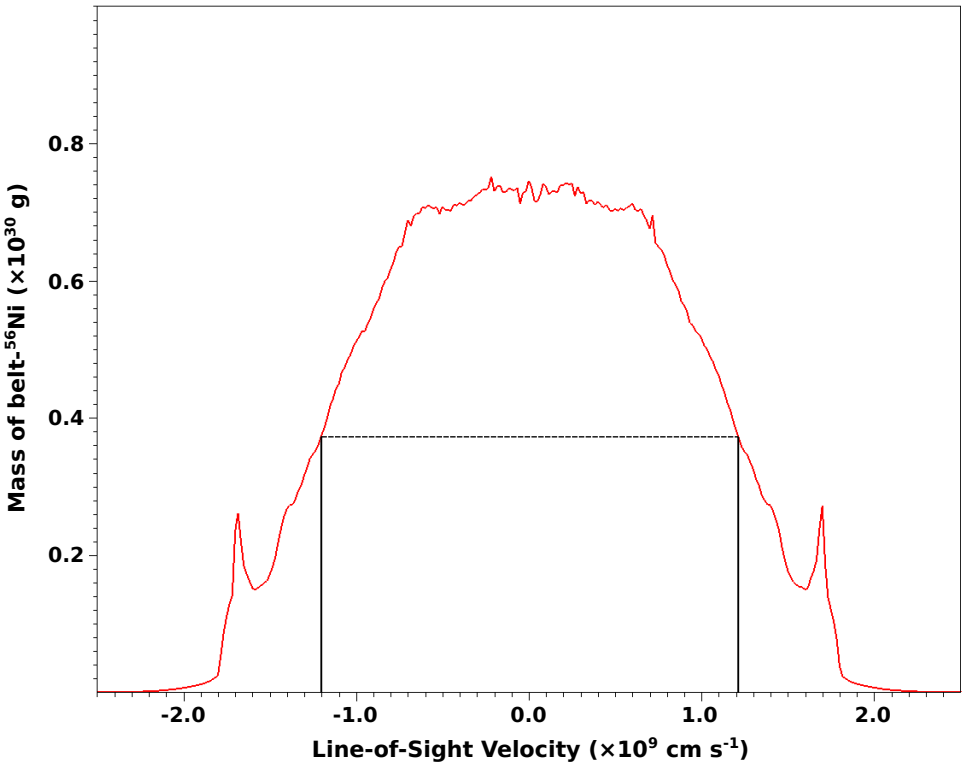


Figure 6.13: Results from model He-C. The FWHM shows that most of the belt ^{56}Ni has line-of-sight velocities below ∼12000 km s^{-1}.

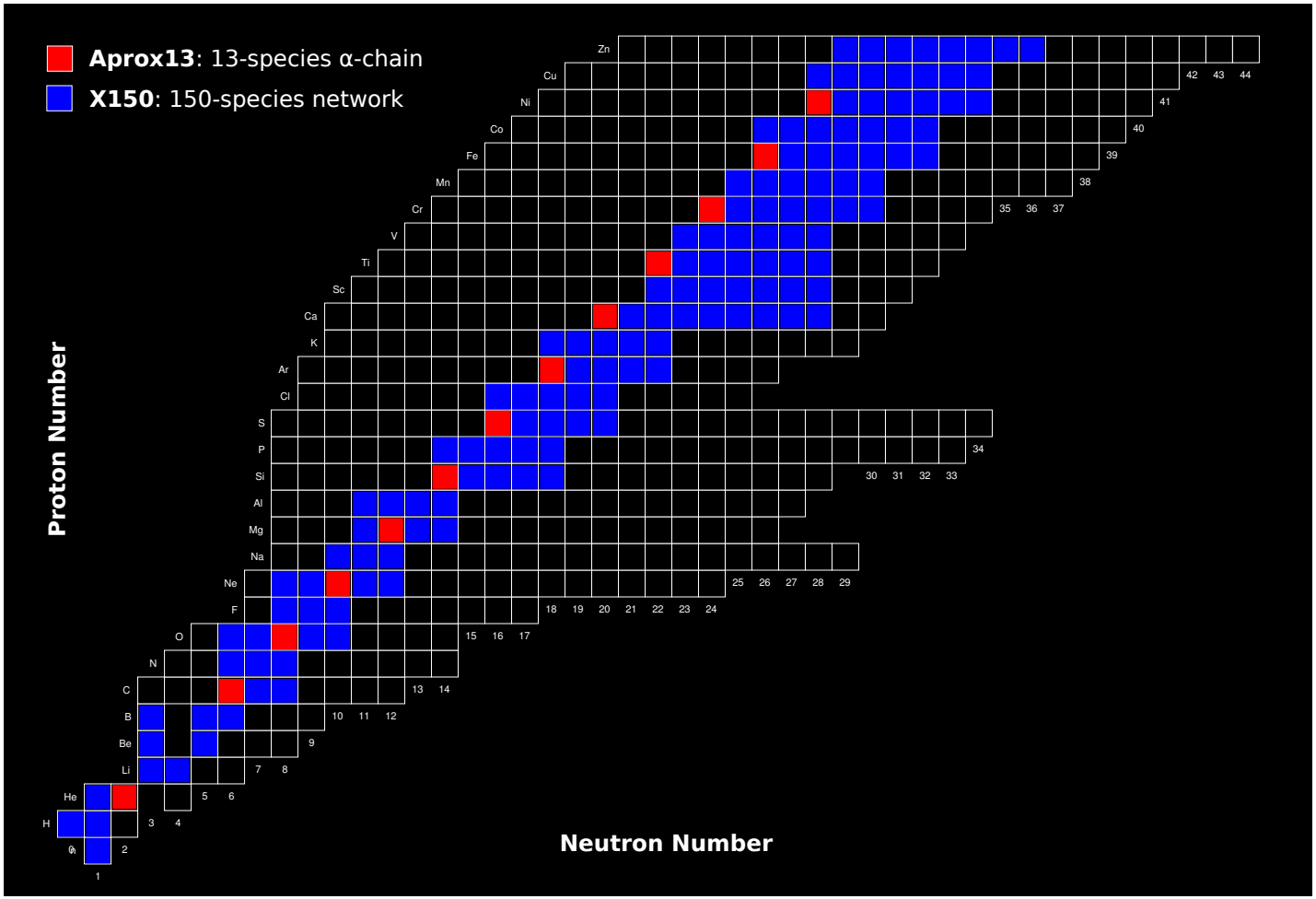


Figure 6.14: Plot of proton number versus neutron number showing the isotopes involved in the 13-species network (red) and the 150-species network (sum of red and blue).

fraction of ^{44}Ti has been included. As the simulations evolve, it is noticable that the 150-species network produces ^{56}Ni more slowly in the core. This happens because the reactions in the reduced network can only follow one path toward the Fe-peak, whereas burning in the large network can deviate from the alpha-pathway into more neutron-rich isotopes on its way to ^{56}Ni. Figure 6.15 shows that, due to the high density in the center of the WD, both simulations eventually burn to completion there, resulting in large amounts of ^{56}Ni. On the other hand, the He-detonations occur in the lower-density outer regions of the WD, where the reactions are truncated by expansion before the burning completes. Therefore, because the large network burns to ^{56}Ni more slowly than the reduced network, when expansion quenches the burning in the outer regions there is less belt-^{56}Ni produced in model He-L-X150 (also shown in Figure 6.15). A comparison of the histograms (Figures 6.16 and 6.17) also shows the lower mass of belt-^{56}Ni produced by the 150-species network relative to the reduced network, and furthermore it demonstrates that the large network does not help to constrain the line-of-sight velocities when compared to the reduced network. In fact, due to the reduction in belt-^{56}Ni, the FWHM range is slightly larger for the 150-species results than for the 13-species. One other notable difference between the simulations is that there is less ^{44}Ti produced by the large network compared to the alpha-network (Figures 6.18 and 6.15). This reduction in the amount of both ^{44}Ti and ^{56}Ni is important because these are radioactive isotopes that are observable to γ-ray telescopes.

6.2.2 Ni-Belts

From the results of the He-belt simulations, it is clear that in order for this modified explosion mechanism to produce results consistent with the observations of SN2014J, there must be some mechanism to equatorially constrain the ashes produced during the He-detonations. So, as a final approach, we made the assumption that there **is** some mechanism to provide the constraint, and we modeled this case by igniting detonations in the centers of C/O WDs surrounded by equatorial belts of pure ^{56}Ni. For these simulations, we found that the line-of-sight velocities of the belt-^{56}Ni were reasonably constrained for all of our models (both

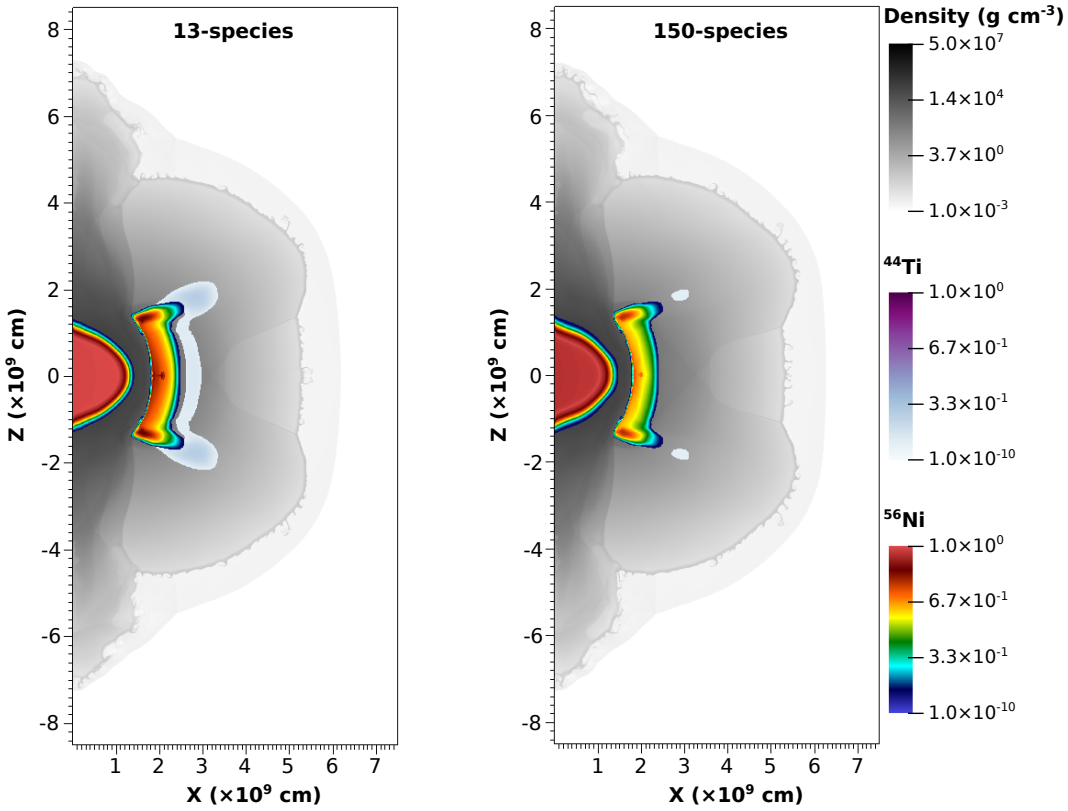


Figure 6.15: Comparison of the final results from models He-K and He-K-X150.

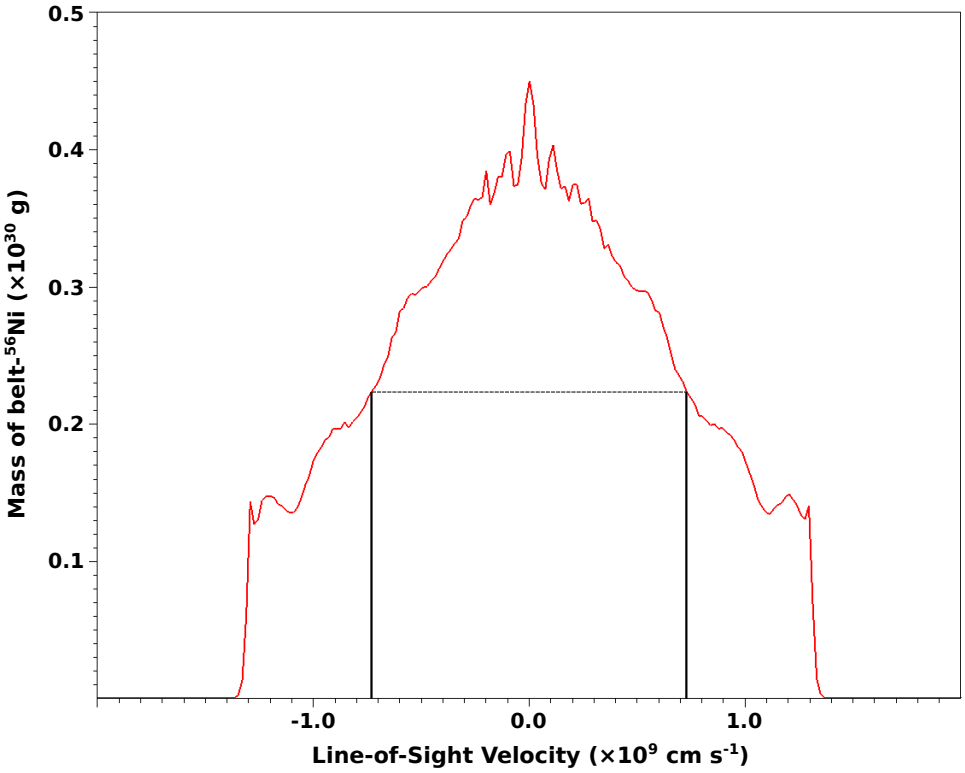


Figure 6.16: Results from model He-K. The FWHM shows that most of the belt ^{56}Ni has line-of-sight velocities below $\sim$7300 km s^{-1}.

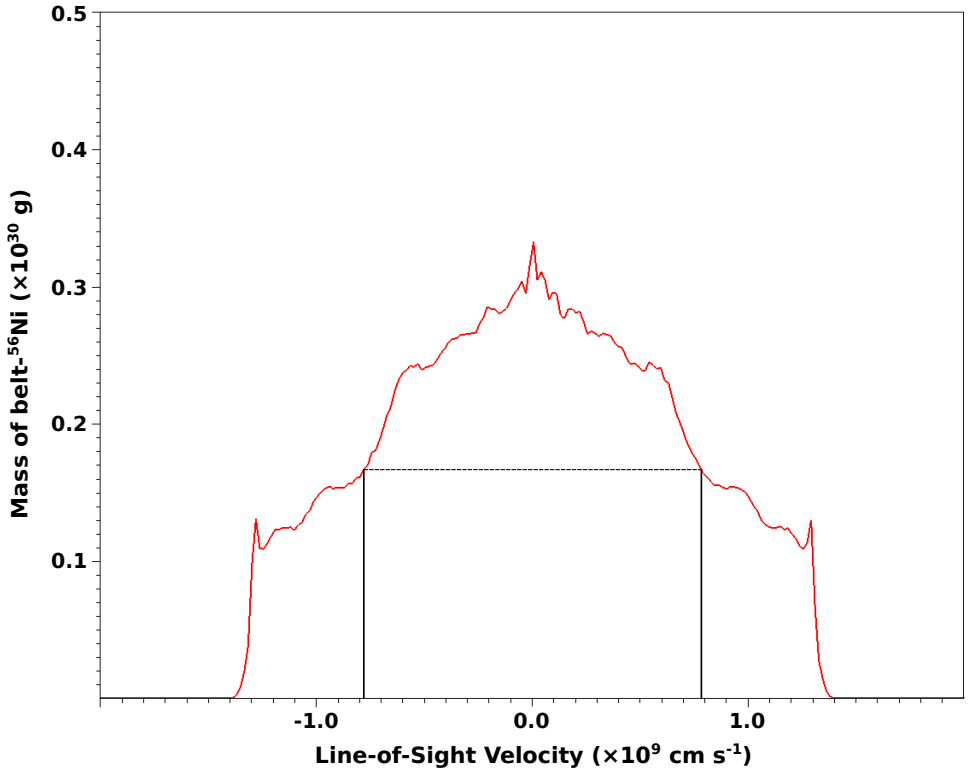


Figure 6.17: Results from model He-K-X150. The FWHM shows that most of the belt ^{56}Ni has line-of-sight velocities below $\sim$7800 km s^{-1}.

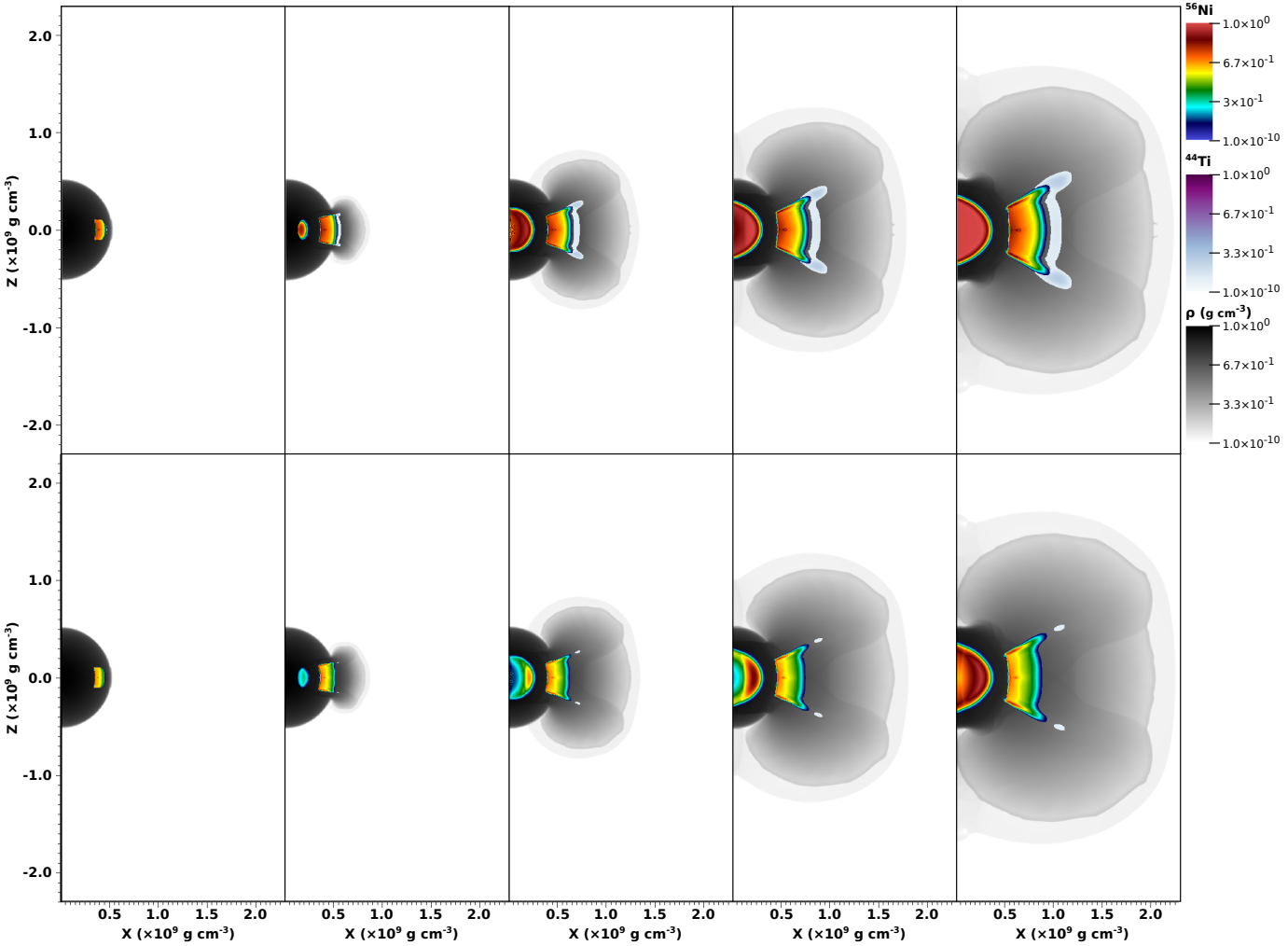


Figure 6.18: A comparison of models He-K and He-K-X150, showing the first 0.5s of the evolution.

constant- and stratified-density belts) and that the amount of ^{56}Ni also agreed with the observations. Figure 6.19 shows the results from model Ni-A (Table 6.2), which was given a confined belt of ^{56}Ni with a constant density of $2{\times}10^6$ g cm^{-3}. The mass of the belt-^{56}Ni did not change during the explosion, and so remains 0.075 M$_\odot$ for this model, but it has been spread out by the explosion. However, the majority of this ^{56}Ni mass is still concentrated within the equatorial plane, so its line-of-sight velocities are constrained to small values (below $\sim$1800 km s^{-1}) as can be seen in the histogram in Figure 6.20.

Figure 6.21 shows the results of model Ni-C, which was given a confined ^{56}Ni-belt that followed the WD profile from $2{\times}10^6$ g cm^{-3}. The confinement of this ^{56}Ni after the explosion is clear and Figure 6.22 shows how this confinement translates to a small range in line-of-sight velocities. Despite the good agreement with the line-of-sight velocities of the belt-^{56}Ni, there is not enough of it in the initial stratified belt. But, the ^{56}Ni resulting from a previous He-detonation should have higher density that the initial He. Thus, by increasing the density of our stratified ^{56}Ni-belt, we can increase its initial (and final) mass. Model Ni-D was given such a confined belt whose density was 3x the underlying WD density profile. Figure 6.23 shows the resulting ^{56}Ni mass fraction of this model and Figure 6.24 shows that the range in line-of-sight velocities for this model are sufficiently constrained. All of the models are also shown to be consistent with normal Type Ia events: core-^{56}Ni masses between 0.5-0.6 M$_\odot$, IMEs around 0.4 M$_\odot$, and explosion energies of $\sim$1.1$\times10^{51}$ ergs (Table 6.2). Thus, we categorize these Ni-belt models as being plausible progenitor models for SN2014J.

6.3 Summary

With these exploratory models, we have shown that the modified double-detonation scenario proposed by Diehl et al. (2014) might be capable of producing the early-time ^{56}Ni features observed in SN2014J. However, this is only true under the assumption that the ashes of the He-belt detonation can be equatorially confined by some mechanism. We have contrived a geometry of the pre-explosion WD consistent with the observations of Diehl et al. (2014),

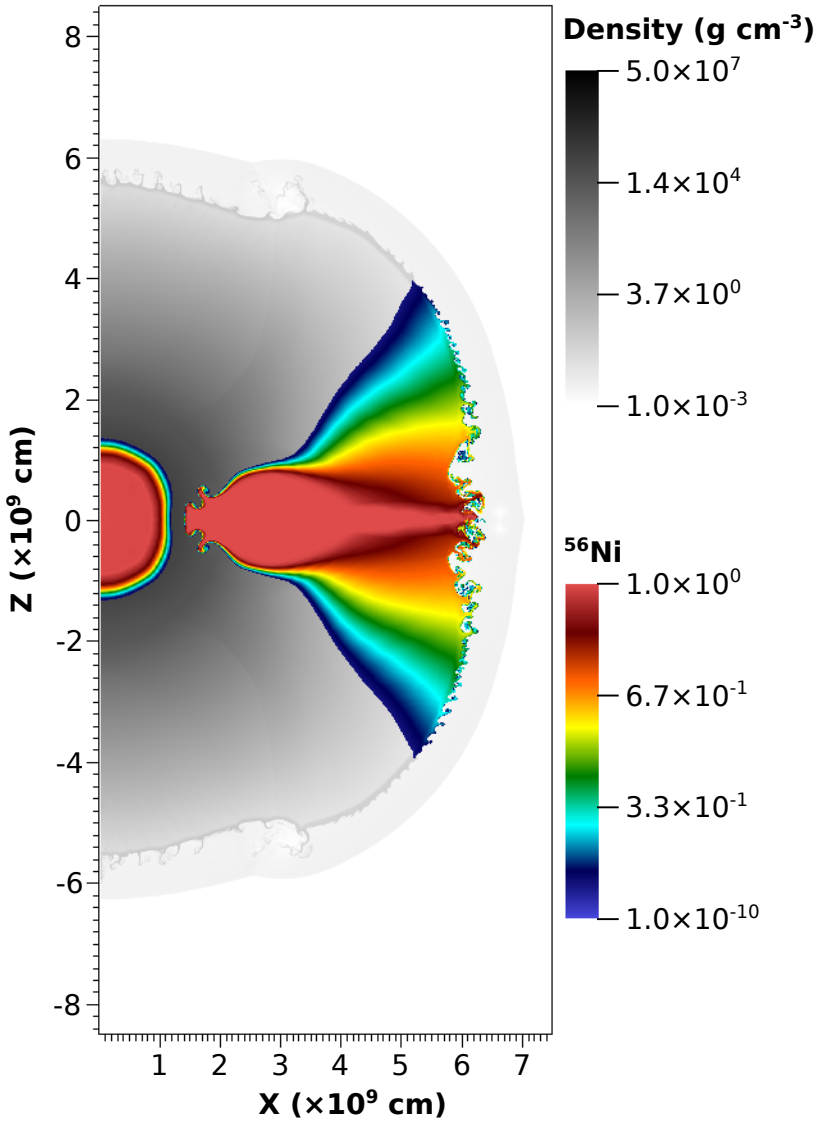


Figure 6.19: Results of model Ni-A. The belt of ^{56}Ni has been spread out by the explosion but the majority of its mass is still close to the equator.

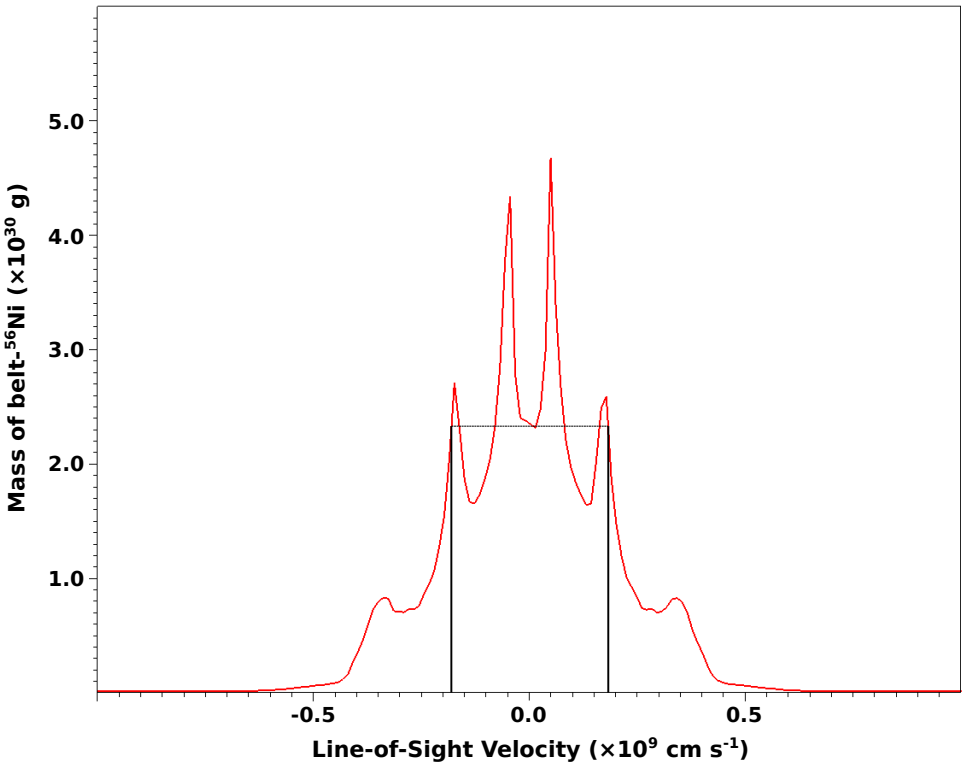


Figure 6.20: Results from model Ni-A. The FWHM shows that most of the belt-^{56}Ni has line-of-sight velocities below $\sim$1800 km s^{-1}

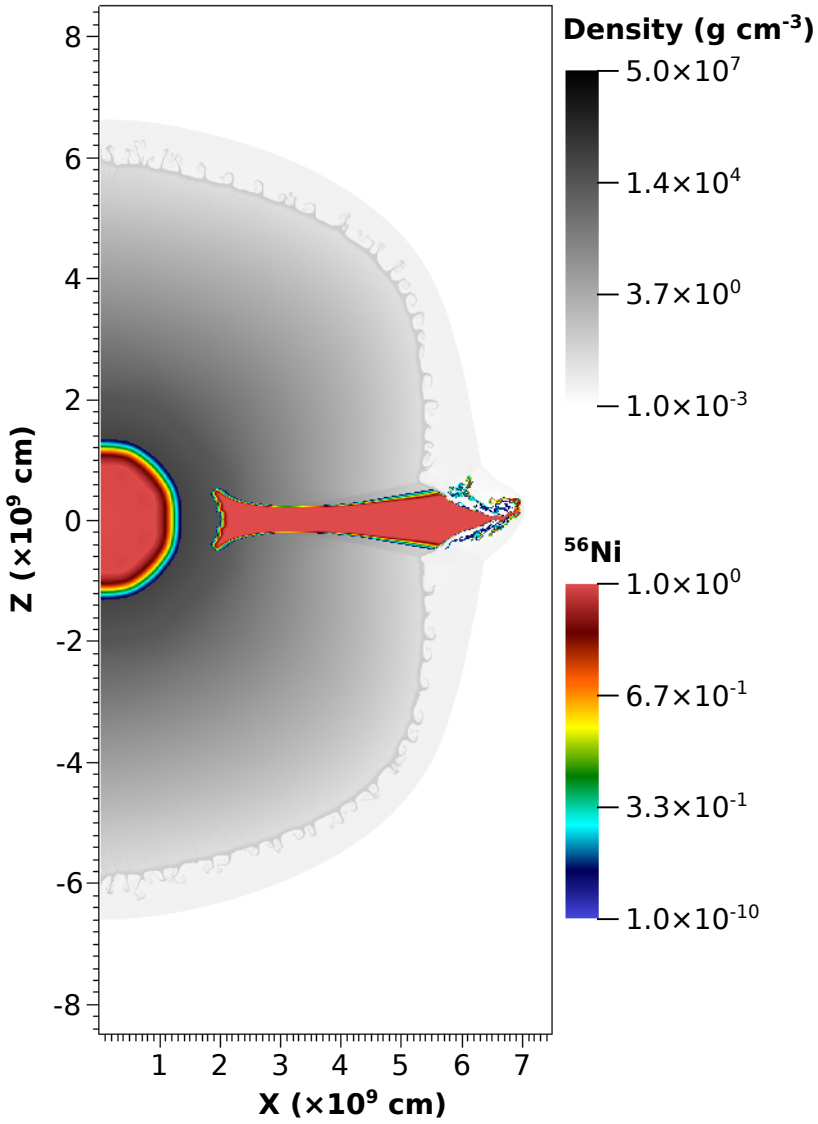


Figure 6.21: Results from model Ni-C. The belt-^{56}Ni has not been spread out much by the explosion and so remains near the equator.

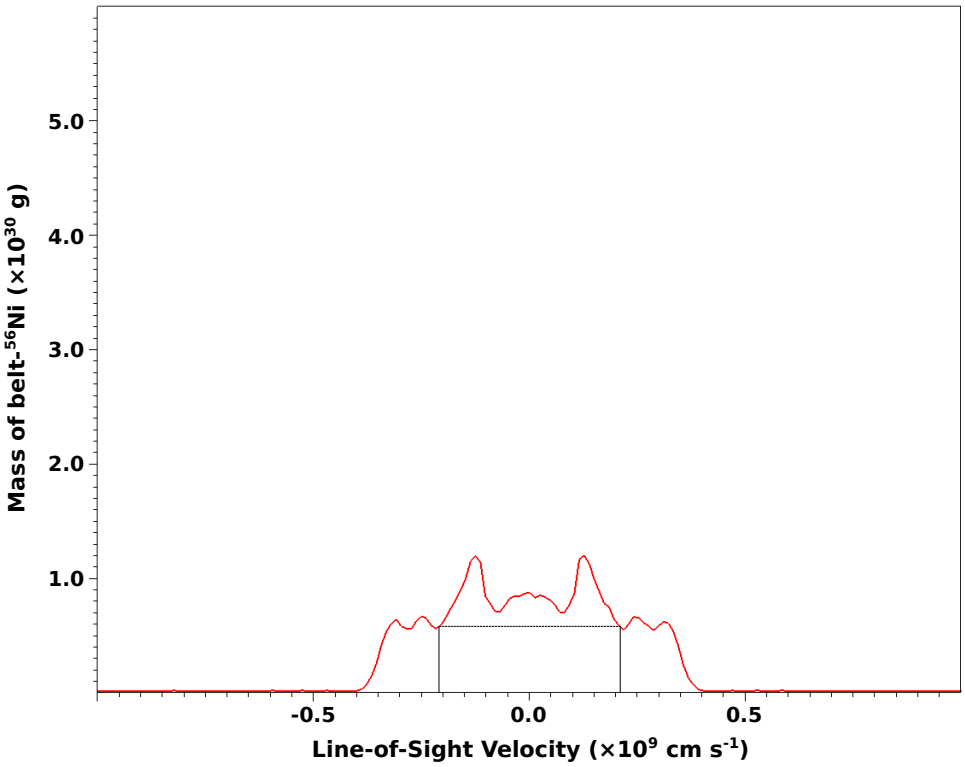


Figure 6.22: Results from model Ni-C. The FWHM shows that most of the belt-^{56}Ni has line-of-sight velocities below $\sim$2100 km s^{-1}

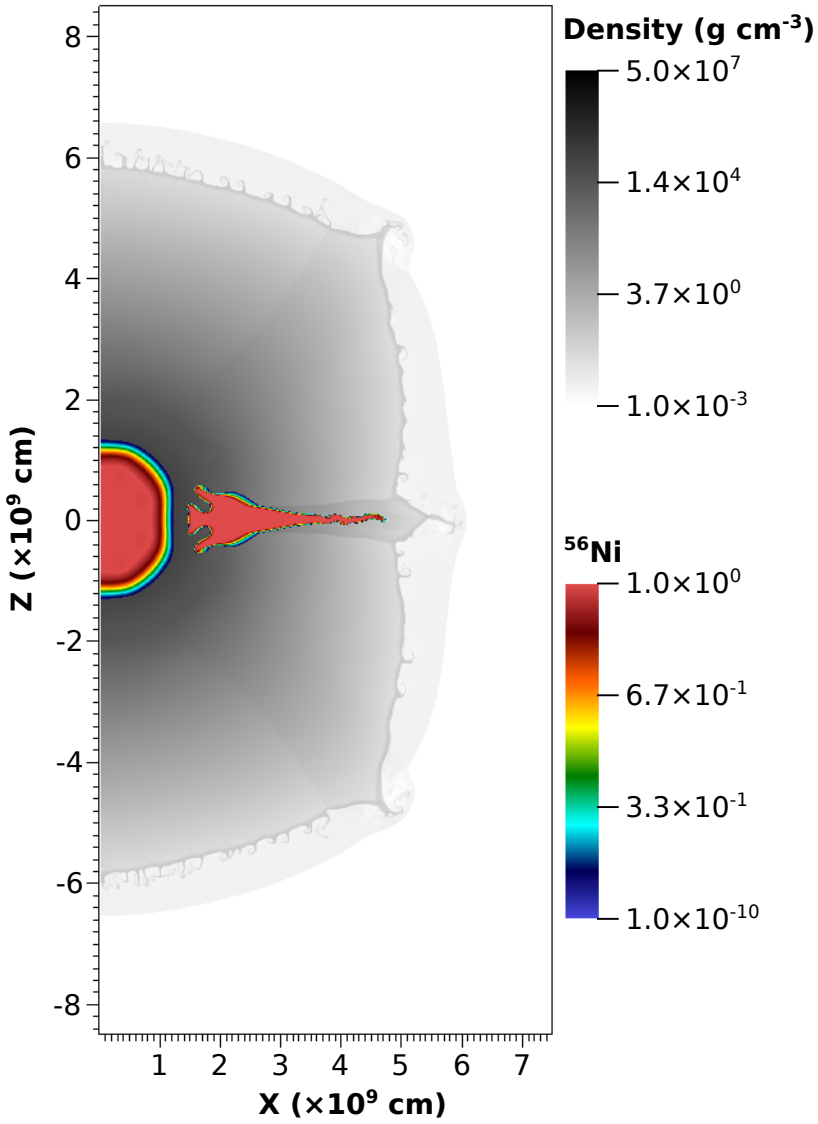


Figure 6.23: Results from model Ni-D. The belt-^{56}Ni has not been spread out much by the explosion and so remains near the equator. By increasing the density by 3× relative to model Ni-C, the belt-^{56}Ni resides deeper inside the remnant.

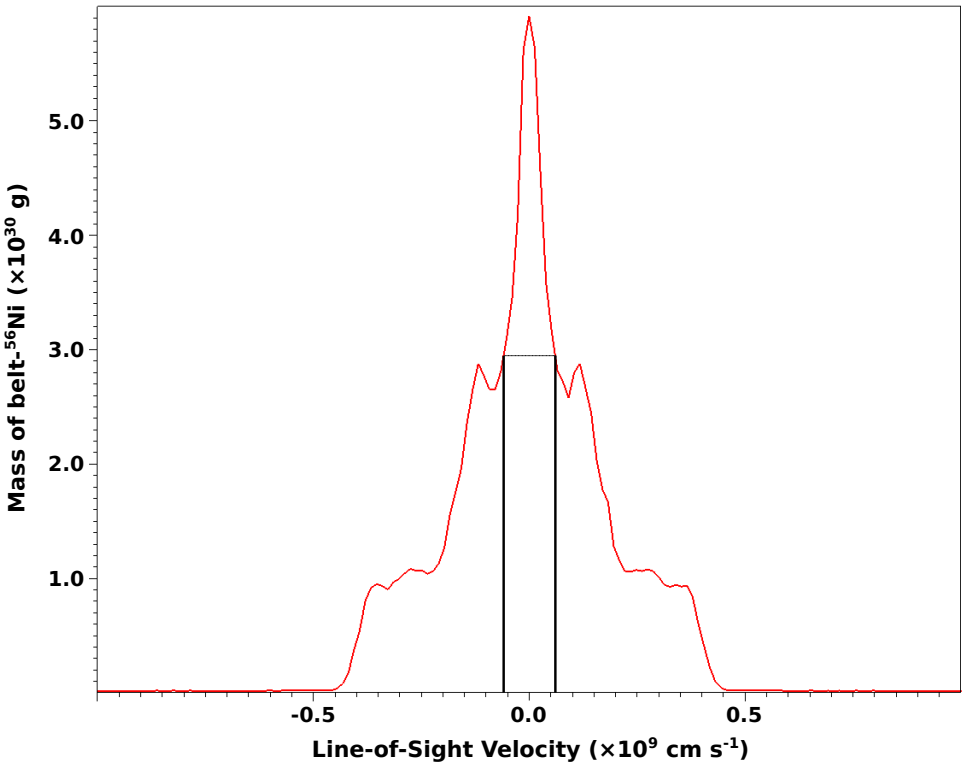


Figure 6.24: Results from model Ni-D. The FWHM shows that most of the belt-^{56}Ni has line-of-sight velocities below $\sim$700 km s^{-1}

however it is uncertain how it could be constructed by nature. This confinement might be realized due to rotation or possibly the presence of magnetic fields. These effects are important to this explosion scenario and will be explored in future work.

Although the use of improved nuclear kinetics did not appreciably affect the dynamics of the ejecta, it did result in the production of less ^{56}Ni and ^{44}Ti relative to the Aprox13 network. These radioactive isotopes are observable to astronomers, and this is important even outside the scope of this particular modified explosion mechanism that we have been considering. Specifically, in the traditional double-detonation scenario, the presence of IGEs in the outer ejecta (produced by detonations in He-shells) has been problematic because it is in conflict with observations. However, recent simulations have shown that He-detonations that lead to successful double-detonations can be sustained in very thin He-shells, reducing the amount of IGEs that are produced (Fink et al., 2010). But one of the remaining obstacles for this explosion mechanism is the over-production of Ti (Kromer et al., 2010). The reduction of ^{56}Ni that we found in our simulations is probably not as important in these thin He-shell models because the burning is truncated before producing ^{56}Ni. However, the reduction in ^{44}Ti can give better agreement with observations and so might prove to be useful in advocating for the traditional double-detonation scenario as a probable progenitor candidate for Type Ia supernovae.

Chapter 7

Conclusions

In this work, we have simulated C/O detonations in low-density environments to understand how using improved nuclear kinetics in place of commonly-used reduced networks (e.g. α-chains) can influence the outcome of SNe Ia models. In addition to 1D detonations, we also simulated 2D and 3D (preliminary) detonations to account for the multi-D effects of cellular structure and to explore a large-scale explosion model. We also carried out many of our simulations over a range of grid resolutions to investigate the effects of unresolved burning.

We found that nuclear network size has the largest influence on our detonation models. The burning length (time) scales over which a fuel source is depleted can be significantly decreased when using a large nuclear reaction network relative to a reduced network. This can affect the outcome of full-star explosion models by altering the incomplete burning products; for a given density, incomplete burning with a large network would be "more complete" than with a reduced network. On the other hand, the size of these burning lengths can be increased by cellular structure in multi-D models, although this effect is smaller compared to the influence of network size. This increase in burning lengths would cause the incomplete burning to be "less complete" than predicted by a 1D model at a given density. Therefore, it is the combination of these two effects that would result in the most accurate burning lengths. Additionally, burning lengths that are smaller than the size of the grid zones can be artificially increased due to burning in an entire (coarse) zone. Although we only found

the C-burning lengths to be unresolved (at our lowest resolution) in our simulations, the O- and Si-burning lengths can also be unresolved in large-scale models. This can result in a larger volume of fuel being burned in a given time than would be burned in a more resolved simulation. The detonation velocities measured from our simulations were found to be essentially unaffected by resolution and dimensionality, but there was a small dependence on network size.

In addition to these small-scale simulations, we investigated the effects of using our higher-fidelity nuclear kinetics in the context of a particular astrophysical situation. Specifically, we explored the plausibility of a modified version of the double-detonation scenario, where the initial detonation occurs in a He-belt rather than a He-shell. One of our results from this investigation showed that using a large reaction network in place of a reduced network decreased the amount of ^{56}Ni and ^{44}Ti that was produced by the He-detonation at low-densities. The reduction of these isotopes occurred because the large network has more reaction pathways than the reduced network, so as the large network processes the fuel toward the Fe-peak, the path of the burning (in the proton-neutron plane) can deviate away from (into more neutron-rich isotopes) the only path available to the α-network; the burning proceeds more slowly toward ^{56}Ni using the large network. Therefore, when the nuclear reactions cease due to expansion at a given time, the burning evolved with the large network has not proceeded as far as that evolved with the reduced network, so there the amount of these two isotopes is smaller. This is a different effect of using the large network than the one resulting in decreased burning lengths, although the cause is the same. In the latter case (decreased burning lengths), the additional reaction pathways act to diminish a fuel source (e.g. C, O, Si) more quickly, whereas in the former case (slowed evolution toward the Fe-peak), the additional reaction pathways can slow the rate at which a product nucleus is populated. As we explained in the conclusions of Chapter 6, this can change the isotopic yields resulting from full-star explosion models and perhaps give better agreement with observations.

These results emphasize the need to include high-fidelity nuclear kinetics in full-star SNe Ia simulations if the results are to be of a predictive value. This can be accomplished by evolving a large nuclear reaction network *in situ* or by incorporating the effects of a large network in an approximate burning scheme. If the former method is chosen, we have shown that care must be taken to avoid the unintentional suppression of large-scale cellular features (and its effects) when prescribing a particular treatment of burning within numerically-widened shocks.

Bibliography

Arnett, W. D. (1969). A possible model of supernovae: Detonation of12c. *Astrophysics and Space Science*, 5(2):180–212. 8

Benz, W., Thielemann, F.-K., and Hills, J. G. (1989). Three-dimensional hydrodynamical simulations of stellar collisions. II - white dwarfs. *ApJL*, 342:986. 11

Boisseau, J. R., Wheeler, J. C., Oran, E. S., and Khokhlov, A. M. (1996). The multidimensional structure of detonations in type ia supernovae. *The Astrophysical Journal*, 471(2):L99–L102. 18, 20, 30, 39

Branch, D., Fisher, A., and Nugent, P. (1993). On the relative frequencies of spectroscopically normal and peculiar type IA supernovae. *The Astronomical Journal*, 106:2383. 4

Bravo, E. and García-Senz, D. (2006). Beyond the bubble catastrophe of type ia supernovae: Pulsating reverse detonation models. *ApJL*, 642(2):L157–L160. 9

Chapman, D. (1899). *Philos. Mag.*, 47:90. 14

Churazov, E., Sunyaev, R., Isern, J., Bikmaev, I., Bravo, E., Chugai, N., Grebenev, S., Knödlseder, P. J. J., , Lebrun, F., and Kuulkers, E. (2015). Gamma-rays from type ia supernova sn2014j. *arXiv eprint*. 108

Churazov, E., Sunyaev, R., Isern, J., Knödlseder, J., Jean, P., Lebrun, F., Chugai, N., Grebenev, S., Bravo, E., Sazonov, S., and Renaud, M. (2014). Cobalt-56 γ-ray emission lines from the type ia supernova 2014j. *Nature*, 512(7515):406–408. 4

Collela, P. and Woodward, P. (1984). *JCoPh*, 54:174. 156

Denisov, Y. and Troshin, Y. (1959). *Phys. Chem. Sec.*, 125:110. 18

Diehl, R., Siegert, T., Hillebrandt, W., Grebenev, S. A., Greiner, J., Krause, M., Kromer, M., Maeda, K., Ropke, F., and Taubenberger, S. (2014). Early 56ni decay gamma rays from SN2014j suggest an unusual explosion. *Science*, 345(6201):1162–1165. xviii, 108, 110, 118, 121, 126, 135

Domínguez, I. and Khokhlov, A. (2011). INCOMPLETE CARBON-OXYGEN DETONATION IN TYPE ia SUPERNOVAE. *ApJ*, 730(2):87. 29

Döring, W. (1943). *Ann. Phys.*, 1:435. 14

Fickett, W. and Davis, C. (1979). *Detonation: Theory and Experiment*. xiii, 16, 18, 33, 60

Filippenko, A. V. (1997). OPTICAL SPECTRA OF SUPERNOVAE. *Annual Review of Astronomy and Astrophysics*, 35(1):309–355. 3, 4

Filippenko, A. V., Richmond, M. W., Branch, D., Gaskell, M., Herbst, W., Ford, C. H., Treffers, R. R., Matheson, T., Ho, L. C., Dey, A., Sargent, W. L. W., Small, T. A., and van Breugel, W. J. M. (1992a). The subluminous, spectroscopically peculiar type IA supernova 1991bg in the elliptical galaxy NGC 4374. *The Astronomical Journal*, 104:1543. 7

Filippenko, A. V., Richmond, M. W., Matheson, T., Shields, J. C., Burbidge, E. M., Cohen, R. D., Dickinson, M., Malkan, M. A., Nelson, B., Pietz, J., Schlegel, D., Schmeer, P., Spinrad, H., Steidel, C. C., Tran, H. D., and Wren, W. (1992b). The peculiar type IA SN 1991t - detonation of a white dwarf? *ApJL*, 384:L15. 7

Fink, M., Röpke, F. K., Hillebrandt, W., Seitenzahl, I. R., Sim, S. A., and Kromer, M. (2010). Double-detonation sub-chandrasekhar supernovae: can minimum helium shell masses detonate the core? *Astronomy and Astrophysics*, 514:A53. 12, 39, 142

Fryxell, B., Müller, E., and Arnett, W. (1989). *Garching: Max-Planck-Institut fur Astrophysik*, 449. 22, 24, 27, 36

Fryxell, B., Olson, K., Ricker, P., Timmes, F. X., Zingale, M., Lamb, D. Q., MacNeice, P., Rosner, R., Truran, J. W., and Tufo, H. (2000). FLASH: An adaptive mesh hydrodynamics code for modeling astrophysical thermonuclear flashes. *ASTROPHYS J SUPPL S*, 131(1):273–334. 156

Gamezo, V., Desbordes, D., and Oran, E. (1999a). *CoFl*, 116:154. 18, 29

Gamezo, V. N., Khokhlov, A. M., and Oran, E. S. (2005). Three-dimensional delayed-detonation model of type ia supernovae. *ApJ*, 623(1):337–346. 9

Gamezo, V. N., Wheeler, J. C., Khokhlov, A. M., and Oran, E. S. (1999b). Multilevel structure of cellular detonations in type ia supernovae. *ApJ*, 512(2):827–842. 20, 29, 30, 39, 49, 72, 84, 89

Hamuy, M., Maza, J., Phillips, M. M., Suntzeff, N. B., Wischnjewsky, M., Smith, R. C., Antezana, R., Wells, L. A., Gonzalez, L. E., Gigoux, P., Navarrete, M., Barrientos, F., Lamontagne, R., della Valle, M., Elias, J. E., Phillips, A. C., Odewahn, S. C., Baldwin, J. A., Walker, A. R., Williams, T., Sturch, C. R., Baganoff, F. K., Chaboyer, B. C., Schommer, R. A., Tirado, H., Hernandez, M., Ugarte, P., Guhathakurta, P., Howell, S. B., Szkody, P., Schmidtke, P. C., and Roth, J. (1993). The 1990 calan/tololo supernova search. *The Astronomical Journal*, 106:2392. xi, 4, 5

Hillebrandt, W., Kromer, M., Röpke, F. K., and Ruiter, A. J. (2013). Towards an understanding of type ia supernovae from a synthesis of theory and observations. *Front. Phys.*, 8(2):116–143. 4

Hillebrandt, W. and Niemeyer, J. C. (2000). Type ia supernova explosion models. *Annual Review of Astronomy and Astrophysics*, 38(1):191–230. 9

Hillebrandt, W. and Röpke, F. (2005). Chasing the flames: The challenge of modeling type ia supernovae in 3d. *Bulletin of the American Astronomical Society*, 37:467. 9

Hix, W. and Thielemann, F. (1999). Computational methods for nucleosynthesis and nuclear energy release. *J. Comput. Appl. Math.*, 109(1-2):321–351. 41, 109, 161

Howell, D. A., Sullivan, M., Nugent, P. E., Ellis, R. S., Conley, A. J., Borgne, D. L., Carlberg, R. G., Guy, J., Balam, D., Basa, S., Fouchez, D., Hook, I. M., Hsiao, E. Y., Neill, J. D., Pain, R., Perrett, K. M., and Pritchet, C. J. (2006). The type ia supernova SNLS-03d3bb from a super-chandrasekhar-mass white dwarf star. *Nature*, 443(7109):308–311. 40

Iben, I. J. and Tutukov, A. V. (1984). Supernovae of type i as end products of the evolution of binaries with components of moderate initial mass (m not greater than about 9 solar masses). *ApJS*, 54:335. 10

Jouguet, J. (1905). *J. Math. Pure Appl.*, 1:347. 14

Kasen, D., Röpke, F. K., and Woosley, S. E. (2009). The diversity of type ia supernovae from broken symmetries. *Nature*, 460(7257):869–872. 10

Katz, B. and Dong, S. (2012). The rate of wd-wd head-on collisions may be as high as the sne ia rate. *arXiv eprints*. 11

Khokhlov, A. (1989). The structure of detonation waves in supernovae. *MNRAS*, 239:785. 18

Khokhlov, A. (1991). Delayed detonation model for type ia supernovae. *Astronomy and Astrophysics*, 245:114–128. 9

Khokhlov, A. M. (1993). Stability of detonations in supernovae. *ApJL*, 419:200. 60, 61

Kromer, M., Sim, S. A., Fink, M., Röpke, F. K., Seitenzahl, I. R., and Hillebrandt, W. (2010). DOUBLE-DETONATION SUB-CHANDRASEKHAR SUPERNOVAE: SYNTHETIC OBSERVABLES FOR MINIMUM HELIUM SHELL MASS MODELS. *ApJ*, 719(2):1067–1082. 12, 142

Kushnir, D., Katz, B., Dong, S., Livne, E., and Fernández, R. (2013). HEAD-ON COLLISIONS OF WHITE DWARFS IN TRIPLE SYSTEMS COULD EXPLAIN TYPE ia SUPERNOVAE. *ApJ*, 778(2):L37. 11

LeVeque, R., Mihalas, D., Dorfi, E., and Müller, E. (1998). Computational methods for astrophysical flow. 27

Li, W., Leaman, J., Chornock, R., Filippenko, A. V., Poznanski, D., Ganeshalingam, M., Wang, X., Modjaz, M., Jha, S., Foley, R. J., and Smith, N. (2011). Nearby supernova

rates from the lick observatory supernova search - II. the observed luminosity functions and fractions of supernovae in a complete sample. *Monthly Notices of the Royal Astronomical Society*, 412(3):1441–1472. 4

Lorén-Aguilar, P., Isern, J., and García-Berro, E. (2010). Smoothed particle hydrodynamics simulations of white dwarf collisions and close encounters. *Monthly Notices of the Royal Astronomical Society*, 406(4):2749–2763. 11

Oran, E. and Boris, J. (2000). *Numerical Simulation of Reactive Flow (2nd Ed.)*. Cambridge University Press. 22

Oran, E., Weber, J. J., Stefaniw, E., Lefebvre, M., and Anderson, J. J. (1998). *CoFl*, 113:147. 18

Pakmor, R., Hachinger, S., Röpke, F. K., and Hillebrandt, W. (2011). Violent mergers of nearly equal-mass white dwarf as progenitors of subluminous type ia supernovae. *Astronomy & Astrophysics*, 528:A117. 11

Pakmor, R., Kromer, M., Röpke, F. K., Sim, S. A., Ruiter, A. J., and Hillebrandt, W. (2010). Sub-luminous type ia supernovae from the mergers of equal-mass white dwarfs with mass $\sim$0.9m$\odot$. *Nature*, 463(7277):61–64. 11

Pakmor, R., Kromer, M., Taubenberger, S., Sim, S. A., Röpke, F. K., and Hillebrandt, W. (2012). NORMAL TYPE ia SUPERNOVAE FROM VIOLENT MERGERS OF WHITE DWARF BINARIES. *ApJ*, 747(1):L10. 11, 39

Papatheodore, T. L. and Messer, O. E. B. (2014). ON NUMERICAL CONSIDERATIONS FOR MODELING REACTIVE ASTROPHYSICAL SHOCKS. *ApJ*, 782(1):12. 21

Parrent, J. T., Thomas, R. C., Fesen, R. A., Marion, G. H., Challis, P., Garnavich, P. M., Milisavljevic, D., Vinkò, J., and Wheeler, J. C. (2011). A STUDY OF CARBON FEATURES IN TYPE ia SUPERNOVA SPECTRA. *ApJ*, 732(1):30. 4, 40

Phillips, M. M. (1993). The absolute magnitudes of type IA supernovae. *ApJL*, 413:L105. 4, 7

Plewa, T., Calder, A. C., and Lamb, D. Q. (2004). Type ia supernova explosion: Gravitationally confined detonation. *ApJL*, 612(1):L37–L40. 9

Raskin, C., Scannapieco, E., Rhoads, J., and Valle, M. D. (2009). PROMPT ia SUPERNOVAE ARE SIGNIFICANTLY DELAYED. *ApJ*, 707(1):74–78. 11

Raskin, C., Scannapieco, E., Rockefeller, G., Fryer, C., Diehl, S., and Timmes, F. X. (2010). 56 ni PRODUCTION IN DOUBLE-DEGENERATE WHITE DWARF COLLISIONS. *ApJ*, 724(1):111–125. 11

Rosswog, S., Kasen, D., Guillochon, J., and Ramirez-Ruiz, E. (2009). COLLISIONS OF WHITE DWARFS AS a NEW PROGENITOR CHANNEL FOR TYPE ia SUPERNOVAE. *ApJ*, 705(2):L128–L132. 11

Ruiter, A. J., Sim, S. A., Pakmor, R., Kromer, M., Seitenzahl, I. R., Belczynski, K., Fink, M., Herzog, M., Hillebrandt, W., Ropke, F. K., and Taubenberger, S. (2012). On the brightness distribution of type ia supernovae from violent white dwarf mergers. *Monthly Notices of the Royal Astronomical Society*, 429(2):1425–1436. 11

Ruiz-Lapuente, P. (2014). New approaches to SNe ia progenitors. *New Astronomy Reviews*, 62-63:15–31. 10

Saio, H. and Nomoto, K. (1985). Evolution of a merging pair of c + o white dwarfs to form a single neutron star. *Astronomy & Astrophysics*, 150(1):L21. 11

Seitenzahl, I. R., Meakin, C. A., Townsley, D. M., Lamb, D. Q., and Truran, J. W. (2009). SPONTANEOUS INITIATION OF DETONATIONS IN WHITE DWARF ENVIRONMENTS: DETERMINATION OF CRITICAL SIZES. *ApJ*, 696(1):515–527. 81

Sharpe, G. J. (1999). The structure of steady detonation waves in type ia supernovae: pathological detonations in c–o cores. *Monthly Notices of the Royal Astronomical Society*, 310(4):1039–1052. 23, 29, 72

Silverman, J. M. and Filippenko, A. V. (2012). Berkeley supernova ia program - IV. carbon detection in early-time optical spectra of type ia supernovae. *Monthly Notices of the Royal Astronomical Society*, 425(3):1917–1933. 4, 40

Sim, S. A., Röpke, F. K., Hillebrandt, W., Kromer, M., Pakmor, R., Fink, M., Ruiter, A. J., and Seitenzahl, I. R. (2010). DETONATIONS IN SUB-CHANDRASEKHAR-MASS c+o WHITE DWARFS. *ApJ*, 714(1):L52–L57. 12, 39

Stehle, M., Mazzali, P. A., Benetti, S., and Hillebrandt, W. (2005). Abundance stratification in type ia supernovae - i. the case of SN 2002bo. *Monthly Notices of the Royal Astronomical Society*, 360(4):1231–1243. 9

Thompson, T. A. (2011). ACCELERATING COMPACT OBJECT MERGERS IN TRIPLE SYSTEMS WITH THE KOZAI RESONANCE: A MECHANISM FOR "PROMPT" TYPE ia SUPERNOVAE, GAMMA-RAY BURSTS, AND OTHER EXOTICA. *ApJ*, 741(2):82. 11

Timmes, F. X., Hoffman, R. D., and Woosley, S. E. (2000a). An inexpensive nuclear energy generation network for stellar hydrodynamics. *ASTROPHYS J SUPPL S*, 129(1):377–398. xiii, 33

Timmes, F. X., Zingale, M., Olson, K., Fryxell, B., Ricker, P., Calder, A. C., Dursi, L. J., Tufo, H., MacNeice, P., Truran, J. W., and Rosner, R. (2000b). On the cellular structure of carbon detonations. *ApJ*, 543(2):938–954. 20, 24, 36, 39, 84, 156

van Kerkwijk, M. H., Chang, P., and Justham, S. (2010). SUB-CHANDRASEKHAR WHITE DWARF MERGERS AS THE PROGENITORS OF TYPE ia SUPERNOVAE. *ApJ*, 722(2):L157–L161. 39

Voitsekhovskii, B., Mitrofanov, V., and Topchian, M. (1963). *Novosibirsk: IZD-VO Sibirsk, Otdel. Akad. Nauk SSST*. 18

von Neumann, J. (1942). *OSRD Reports*, 1:549. 14

Webbink, R. F. (1984). Double white dwarfs as progenitors of r coronae borealis stars and type i supernovae. *ApJL*, 277:355. 10

Wheeler, J. C. and Hansen, C. J. (1971). Thermonuclear detonations in collapsing white dwarf stars. *Ap&SS*, 11:373. 8

Whelan, J. and Icko, J. I. (1973). Binaries and supernovae of type i. *ApJL*, 186:1007. 8

Woosley, S. E. and Weaver, T. A. (1986). The physics of supernova explosions. *Annual Review of Astronomy and Astrophysics*, 24(1):205–253. 8

Woosley, S. E., Wunsch, S., and Kuhlen, M. (2004). Carbon ignition in type ia supernovae: An analytic model. *ApJ*, 607(2):921–930. 8

Zel'dovich, Y. (1940). *Eksp. Teor. Fiz.*, 10:524. 14

Zheng, W., Silverman, J. M., Filippenko, A. V., Kasen, D., Nugent, P. E., Graham, M., Wang, X., Valenti, S., Ciabattari, F., Kelly, P. L., Fox, O. D., Shivvers, I., Clubb, K. I., Cenko, S. B., Balam, D., Howell, D. A., Hsiao, E., Li, W., Marion, G. H., Sand, D., Vinko, J., Wheeler, J. C., and Zhang, J. (2013). THE VERY YOUNG TYPE ia SUPERNOVA 2013dy: DISCOVERY, AND STRONG CARBON ABSORPTION IN EARLY-TIME SPECTRA. *ApJ*, 778(1):L15. 4, 40

Appendix

Appendix A - The FLASH code

The simulations performed in this research were all carried out within FLASH (version 4; Fryxell et al., 2000), a parallel simulation code that is capable of handling reactive, compressible flow problems in astrophysical environments. The widely-used directionally-split piecewise-parabolic method (Collela and Woodward, 1984) was chosen to evolve the Euler equations on an adaptive mesh, and these equations were closed using an equation of state relevant for electron-degenerate environments. In the public version of FLASH there are three nuclear reaction networks available to evolve the burning in a simulation; a 7-, 13-, and 19-species network. Of these, we often utilize the 13-species "Aprox13" α-chain. This network has been shown to capture energy generation rates for carbon and oxygen comparable to larger networks without their computational burden (Timmes et al., 2000b). The reactions include (α, γ) and $(\alpha, p)(p, \gamma)$ links as well as their reverse sequences among the 13 isotopes ^{4}He, ^{12}C, ^{16}O, ^{20}Ne, ^{24}Mg, ^{28}Si, ^{32}S, ^{36}Ar, ^{40}Ca, ^{44}Ti, ^{48}Cr, ^{52}Fe, and ^{56}Ni.

Below we have included the Config files as well as the problem setup files for all of our simulations:

Detonation Tubes - 1D, 2D, 3D

```
REQUIRES Driver
REQUIRES physics/Hydro
REQUIRES physics/Eos/EosMain/Helmholtz
REQUIRES physics/sourceTerms/Burn/BurnMain/nuclearBurn/XNet14_new
REQUIRES Simulation/SimulationComposition
REQUIRES Multispecies
REQUESTS IO REQUESTS IO/IOMain/hdf5/parallel/PM

D    xhe4 mass fraction of he4
D    xc12 mass fraction of c12
```

```
D    xo16 mass fraction of o16
D    rhoAmbient density of the cold upstream material
D    tempAmbient temperature of the cold upstream material
D    velxAmbient x-velocity of the cold upstream material
D    rhoPerturb density of the post shock material
D    tempPerturb temperature of the post shock material
D    velxPerturb x-velocity of the post shock material
D    radiusPerturb distance below which perturbation is applied
D    x/y/zCenterPerturb origin of the of the perturbation
D    usePseudo1d .true.  for a 1d initial configuration, with the
D    & copied along the y and z directions
D    & .false.  for a spherical configuration
D    noiseAmplitude white noise amplitude added to perturbation
D    noiseDistance distances above and below r_init get noise

PARAMETER xhe4 REAL 0.0 [0.0 to 1.0]
PARAMETER xc12 REAL 1.0 [0.0 to 1.0]
PARAMETER xo16 REAL 0.0 [0.0 to 1.0]

PARAMETER rhoAmbient REAL 1.0e7 [0 to ]
PARAMETER tempAmbient REAL 2.0e8 [0 to ]
PARAMETER velxAmbient REAL 0.0

PARAMETER rhoPerturb REAL 4.236e7
PARAMETER tempPerturb REAL 4.423e9
PARAMETER velxPerturb REAL 2.876E+08

PARAMETER radiusPerturb REAL 25.6
PARAMETER xCenterPerturb REAL 0.0
```

```
PARAMETER yCenterPerturb REAL 0.0
PARAMETER zCenterPerturb REAL 0.0

PARAMETER usePseudo1d BOOLEAN FALSE

PARAMETER noiseAmplitude REAL 1.0e-2
PARAMETER noiseDistance REAL 5.0

PARAMETER f REAL 0.2

VARIABLE eold
VARIABLE mprs
VARIABLE inshock
VARIABLE checkEos
VARIABLE NBTS
VARIABLE TSSZ
```

He-Belt Detonations

```
REQUIRES Driver
REQUIRES Grid
REQUIRES physics/Hydro
REQUIRES physics/Gravity/GravityMain/Poisson
REQUIRES physics/Eos/EosMain/Helmholtz
REQUIRES physics/sourceTerms/Burn/BurnMain/nuclearBurn/XNet14_new
REQUIRES Simulation/SimulationComposition
REQUIRES Multispecies
REQUESTS IO
```

```
# ambient medium outside star
#
# dens_fluff = density of the fluff
# temp_fluff = temperature of the fluff
# xc12_fluff = c12 mass fraction of the fluff
# xo16_fluff = o16 mass fraction of the fluff

PARAMETER dens_fluff REAL 1.0e-3
PARAMETER temp_fluff REAL 3.0e7
PARAMETER xc12_fluff REAL 0.5e0
PARAMETER xne22_fluff REAL 0.0e0

#
# ignition
#

PARAMETER ignite BOOLEAN FALSE
PARAMETER x_match REAL 0.e0
PARAMETER y_match REAL 0.e0
PARAMETER z_match REAL 0.e0
PARAMETER r_match REAL 0.e0
PARAMETER t_ignite REAL 4.e9

PARAMETER useBelt BOOLEAN FALSE
PARAMETER inBelt REAL 0.e0
PARAMETER outBelt REAL 0.e0
PARAMETER topBelt REAL 0.e0
PARAMETER bottomBelt REAL 0.e0
```

```
PARAMETER densMult REAL 1.e0
```

Appendix B – XNet

XNet Hix and Thielemann (1999) is a thermonuclear reaction network that is capable of including an arbitrary number of species with all of their interconnecting reactions (REACLIB). The system of ODEs that describe a particular network are solved with the LAPACK DGESV routine and the Backward Euler scheme evolves the system in time. Because the public version of FLASH only includes three small network, we created a custom version of FLASH that includes three new networks that are evolved with XNet; a 14-, 42-, and 150-species network. In order to do so, we needed to add an initialization routine that reads in and distributes the nuclear data from the master MPI rank to all other ranks. We also needed to alter a few FLASH routines because FLASH requires knowledge of the network size during the setup of a problem. By creating a set of Python scripts that take XNet data (e.g. number of species, proton and neutron numbers, binding energies of each species) files as input, we automated this process to make adding new networks to FLASH a trivial task. However, evolving a large nuclear reaction network in each zone of a hydrodynamics code every time step can be computationally quite burdensome. The cost of solving large networks increases as the number of species squared and can end up dominating the runtime of simulations. In order to ameliorate part of this burden, we added OpenMP threading to the initialization routines and to the burning routine that FLASH uses to loop over the local blocks and all of their zones. The XNet code was already "thread safe" so we only needed to alter several FLASH files and interface routines. With this threaded version of FLASH/XNet, we were able to decrease the runtime by about 5× with 8 OpenMP threads per MPI rank. This custom version of FLASH afforded us the unique ability to study hydrodynamical models of Type Ia supernovae evolved with large *in situ* nuclear reaction networks.

Vita

Thomas Papatheodore was born on June 14, 1979 to parents Deborah and James Papatheodore in Flint, Michigan. He was a student in the Swartz Creek school system until he graduated from Swartz Creek High School in 1997. In the fall of 2002, he enrolled in courses at the University of Michigan, Flint, and graduated with a Bachelor's degree in physics in May of 2008. In the fall of 2009, Thomas began his graduate studies at the University of Tennessee in Knoxville, where he received a Master of Science degree in physics in May of 2012. He then continued his graduate work as a PhD candidate at the University of Tennessee, where he studied computational astrophysics. On July 10, 2015, Thomas successfully defended his dissertation and received his PhD in August.